

Dieser Forschungsbericht wurde als Dissertation von der Mathematisch-Naturwissenschaftlichen Fakultät der Universität Bonn angenommen und ist auf dem Publikationsserver der ULB Bonn elektronisch publiziert: <https://nbn-resolving.org/urn:nbn:de:hbz:5-63793>

- 1. Gutachter: Prof. Dr. Dieter Meschede
- 2. Gutachter: Prof. Dr. Yoav Sagi
- 3. Gutachter: Prof. Dr. Johann Kroha
- 4. Gutachter: Prof. Dr. Carl-Friedrich Bödigheimer

Tag der Promotion: 31.08.2021
Erscheinungsjahr: 2021

A mis papás, mi esposa Fabiana y mi hija María Inés

Abstract

The development of quantum technologies requires a deep knowledge of quantum systems and a high level of control of quantum states. In this thesis I report on my contribution to three areas that are important to quantum technologies: (i) Imaging of quantum states (ii) Fast transport of matter wave packets (iii) Estimation of the speed limit of quantum evolution. The platform here used consists of single neutral ^{133}Cs atoms trapped in a state dependent optical lattice potential. The control over the internal state of the atoms and the potential landscape is used as a tool to study the atomic wave packet dynamics.

In the first part of the thesis I present the experimental setup as well as various experimental techniques that are required for the measurements presented in the following chapters. Two new implementations have been done in order to realize the desired measurements. One of them is a technique to measure the motional ground state population fraction, with an accuracy that is robust over a wide range of temperatures of the thermal ensemble. The second one is a pair of Raman beams to couple two hyperfine states with Rabi frequencies of around 6.5 MHz. Much faster than the observed wave packet dynamics.

In chapter 3, I present a new technique to obtain time-resolved single-pixel images of quantum wave packets using Ramsey interferometry. The technique shares a clear analogy to classical optical imaging and can be potentially extended to obtain multi-pixel images that contain the same information as the full wave function. Even though the measurements presented in this thesis are restricted to single-pixel images, important information is extracted from them, including the Hamiltonian moments, the energy spectrum of the Hamiltonian and the population probabilities in the basis of motional eigenstates.

In the last part of the thesis, the quantum speed limit of two different processes are studied. In chapter 4, the Mandelstam-Tamm and the Margolus-Levitin bounds are verified for atomic wave packets in a static optical lattice potential. The bounds impose a limit to the maximum rate of change of a quantum state. Two different regimes are covered: one where the Mandelstam-Tamm bound is more restrictive and one where the Margolus-Levitin bound is more restrictive. Moreover, it has been observed that the atomic wave packets evolve at a rate very close to the limit imposed by the Mandelstam-Tamm bound. In chapter 5, the speed limit of a different quantum process is studied, namely, fast atom transport without motional excitations over distances much longer than the width of the atomic wave packet. The transport trajectories are obtained with optimal quantum control, making possible to realize transport operations down to the shortest fundamental duration - the quantum speed limit. The Mandelstam-Tamm bound is found to predict an absurdly small estimate of the minimum transport duration, but a meaningful bound consistent with the measured speed limit is obtained based on geometric arguments.

Parts of this thesis have been published in a peer-reviewed journal:

- [1] M. R. Lam, N. Peter, T. Groh, W. Alt, C. Robens, D. Meschede, A. Negretti, S. Montangero, T. Calarco, and A. Alberti, *Demonstration of Quantum Brachistochrones between Distant States of an Atom*, (2021), Phys. Rev. X 11, 011035. DOI: <https://doi.org/10.1103/PhysRevX.11.011035>

Parts of this thesis have been uploaded to arXiv and are in the process to be published in a peer-reviewed journal:

- [2] G. Ness, M. R. Lam, W. Alt, D. Meschede, Y. Sagi and A. Alberti, *Observing quantum-speed-limits crossover with matter wave interferometry*. (2021). arXiv: 2104.05638 [quant-ph]

My contribution to the articles: I contributed to the preparation and maintenance of the experimental setup and the realization of all the measurements presented in the articles. Subsequently, I took part in the data analysis and the manuscript writing together with the other authors.

Contents

1	Introduction	1
2	Experimental apparatus and measurement techniques	3
2.1	Internal degrees of freedom	3
2.1.1	Atom trapping and cooling	3
2.1.2	Optical dipole trap	5
2.1.3	Spin state preparation	8
2.1.4	Microwave driving and σ -Qubit	8
2.1.5	Raman driving and π -Qubit	8
2.1.6	Lattice depth and position control	10
2.2	External degrees of freedom	12
2.2.1	Motional ground state preparation	12
2.2.2	Robust measurement of motional ground state population	14
2.2.3	Measurement of potential depth and transverse temperature	16
2.2.4	Raman Ramsey interferometry	18
2.2.5	Potential crosstalk compensation	20
3	Hello atom, how do you look like?	23
3.1	Introduction	23
3.2	Single pixel image of a quantum wave packet	24
3.3	Model-agnostic spectral decomposition	26
3.4	Hamiltonian moments from recorded image traces	29
3.5	Phase of single-pixel images	31
3.6	Outlook	34
4	How fast am I allowed to drive Mr. Heisenberg?	37
4.1	Introduction	37
4.2	Observing quantum-speed-limits crossover with matter-wave interferometry	40
4.2.1	Introduction	40
4.2.2	Fast matter wave interferometry	41
4.2.3	Testing quantum speed limits	41
4.2.4	Quantum-speed-limit crossover	42
4.2.5	Deviation from the speed limit	43
4.2.6	Concluding remarks	44
4.2.7	Appendix	45
4.3	Summary	49

5	Quantum drag racing	51
5.1	Introduction	51
5.2	Demonstration of quantum brachistochrones between distant states of an atom	54
5.2.1	Introduction	54
5.2.2	Quantum Brachistochrones between distant states	55
5.2.3	Fast atom transport in optical conveyor belts	55
5.2.4	Optimal transport solutions	56
5.2.5	Revealing the quantum speed limit	56
5.2.6	Coherent splitting and recombination of matter waves	58
5.2.7	Interpretation and physical insight	58
5.2.8	Conclusions and Outlook	59
5.2.9	Appendix	60
5.3	Summary	71
6	Summary and Outlook	73
	Bibliography	75
A	Change of energy reference of Hamiltonian moments	83
B	Overlap between coherent states	85
C	Bound of the phase of single-pixel images	87

Introduction

Faster cars, faster planes, faster internet. The world is every day more impatient. Time is gold nowadays. But I cannot think of any field where time is as “expensive” as in quantum technologies, where the required processes have to be done in time scales that go beyond our every-day notion of time. Every tiny fraction of a second counts, so we keep pushing the gas pedal as long as we can. We are in a constant race against nature and keep speeding things up, beating every technical limitation that gets on our way. But how far can we keep racing? Or in other words, is it always going to be a matter of human creativity and ingenuity to push the limit still one more step? It turns out it isn’t; also in the quantum realm there is a speed limit, a fundamental bound impossible to overcome by technical improvements.

The impact of technology on society has hugely increased over the last decades, and quantum technologies promise to do the same in the times to come. We hear that quantum computers will be much faster than classical computers [3, 4], that quantum cryptography will make information transfer more secure than ever [5] and that quantum sensors can improve the sensitivity to measure magnetic fields, electric fields, acceleration, rotation, gravitational fields, etc. [6]. But all these technologies share the characteristic that they rely on quantum processes, meaning that they are very sensitive to external disturbances. This is why the time needed to realize the required operations has important implications in many of those quantum technologies, including quantum information processing [7–10], quantum communication [11–13], quantum metrology [14–16], energy storage [17], bond-selective chemistry [18, 19], among others. In fact, the fundamental limit on the duration of the desired processes can potentially become a limiting factor in the performance of future technologies. This is why substantial effort has gone into understanding the speed limit of different processes, such as quantum gates [20], information transport [21, 22], information production [23], nonequilibrium thermodynamics [24], as well as fundamental limits that govern the evolution rate of generic quantum systems [25–33]. And surely, the implications of such limits on concrete applications like computational speed [34–37].

One of the earliest studies on the speed limit of quantum evolution was done by Leonid Mandelstam and Igor Tamm (MT), and dates back to the 40’s [27]. They reported an inequality that sets a lower bound to the duration of quantum processes. The value predicted by the bound only depends on the energy spread of the wave function, and can be interpreted as an alternative version of the famous Heisenberg’s time-energy uncertainty relation [38]. The result was later generalized to time-dependent Hamiltonians by Anandan and Aharonov [30]. A similar result by Norman Margolus and Lev B. Levitin (ML) predicts a bound that depends on the mean energy of the wave function instead of the energy spread [28]. The unified bound, defined as the maximum between the MT and ML bounds, is considered to be the quantum speed limit, which has been proved to be saturated only by systems that can be effectively reduced to two-level systems [39].

The MT and ML bounds have only been experimentally verified for effective two-level systems in the past [40]. The bounds are expected to be satisfied by any quantum system, however, it is known that for more complex systems the bounds may provide absurdly small values that fall short of reflecting the true limit [29]. Therefore, one may naturally think that the bounds are only useful for simple two-level systems and turn useless as soon as more levels are added. In chapter 4 we will see that such a quick reasoning is not true. I present our results on the experimental verification of the unified bound for the dynamical evolution of single neutral atoms in an optical lattice, which constitutes a multi-level system. We have found that the evolving wave packet not only satisfies the bound but also evolves at a speed that approaches the limit even when multiple energy levels are populated. Moreover, the bound was verified in two different regimes: one in which the MT bound imposes a stronger limit and one in which the ML bound imposes a stronger limit.

As already mentioned, the MT and ML bounds fall short of predicting the true speed limit of some quantum processes. Particularly, this happens in processes that connect spatially distant states for which a Rabi-type coupling is impossible. A process of this type is studied in chapter 5 where our results on single atom transport in optical lattices over distances of around 20 times the size of the wave packet are presented. The atoms are initially prepared in the motional ground state and transported in such a way that they are still in the ground state after the transport process. The transport trajectories are obtained by optimal quantum control which optimizes the transport's fidelity, given by the ground state population fraction after transport. Transport operations with a fidelity equivalent to one are obtained for any transport duration above a certain threshold, identified as the quantum speed limit. The observed value of the quantum speed limit is well above the one predicted by the MT bound but is consistent with a bound that we obtained with geometric arguments following a proposal by Bukov et al., [29].

Another subject of great importance for quantum technologies is the knowledge of the wave function corresponding to the quantum states that are being manipulated. The wave function contains all the information of the quantum state and this is why various techniques to image it have been explored in different platforms [41–45]. In chapter 3 of this thesis, our results on time-resolved single-pixel imaging of atomic wave packets in optical lattices are presented. The images are obtained with a novel technique that makes use of Ramsey interferometry to image a time-evolving wave function by comparing it to a static wave function. The measurements here presented are limited to a single pixel, but the technique can be naturally extended to obtain a multi-pixel image that would contain the same information as the wave function. Moreover, there are multiple features of the wave function and the trapping potential that are extracted from the single-pixel images. The Hamiltonian moments of the system are extracted from the behavior of the single-pixel images at the limit of short times, while the energy spectrum of the trapping potential is extracted from the time dependence of the images over times of a few trapping periods. The Hamiltonian moments characterize the evolution of the wave packet, and the first two of them provide an upper bound to the rate of change of the wave packet evolution according to the MT and ML bounds discussed in chapter 4. In fact, the recorded single-pixel image traces presented in chapter 3 have been used to verify the MT and ML bounds in chapter 4.

Experimental apparatus and measurement techniques

The measurements discussed in this thesis require high level of control over atomic quantum states in order to achieve the desired state preparation and subsequent manipulation. In our experiment we use a one-dimensional optical lattice (Fig. 2.1A) as our canvas to trap, manipulate and study the dynamics of neutral ^{133}Cs atoms in a potential well. Specifically, we make use of the control over the internal degrees of freedom (atomic hyperfine levels, see Fig. 2.2) to study the dynamics of the external degrees of freedom (motional states in the trapping potential, see Fig. 2.1B). In this chapter I present basic concepts of atom trapping and cooling as well as the experimental apparatus and techniques used to realize the measurements presented in the following chapters. The concepts and techniques concerning the internal degrees of freedom are introduced in Sec. 2.1, and the concepts involving the external degrees of freedom are discussed in Sec. 2.2.

2.1 Internal degrees of freedom

2.1.1 Atom trapping and cooling

Every experimental sequence realized in our experiment starts by trapping the cesium atoms from a low pressure thermal background gas using a magneto-optical trap (MOT). The MOT has three orthogonal pairs of counter-propagating circularly-polarized laser beams tuned to a frequency close to the atomic cycling transition $|F = 4\rangle \rightarrow |F' = 5\rangle$ (see Fig. 2.1C), red detuned by a few times the natural linewidth of the transition $\Gamma_{D2} = 2\pi \cdot 5.22 \text{ MHz}$ [46]. Due to the Doppler shift, the MOT beams produce radiation pressure on the atoms only in the direction opposite to their velocity [47]. Additionally, the MOT has a pair of coils in anti-Helmholtz configuration (called MOT coils) that form a quadrupole magnetic field gradient. The center of the quadrupole field is located at the position where the MOT beams intersect each other. The exact position of the center of the quadrupole field is controlled by three additional pairs of coils (called compensation coils) in Helmholtz configuration. When the magnetic field gradient is turned on, the radiation pressure becomes position dependent due to the Zeeman splitting [48]. Specifically, the radiation pressure increases as the atoms move away from the center of the quadrupole field. This way, the atoms are trapped from the background gas in a region around the center of the quadrupole field and cooled down to temperatures around the Doppler limit $T_D = \hbar\Gamma_{D2}/(2k_B) \approx 125 \mu\text{K}$ [49]. More details on the MOT used in our experiment can be found in [50] and for more details on the physical effects in a MOT see [47, 51].

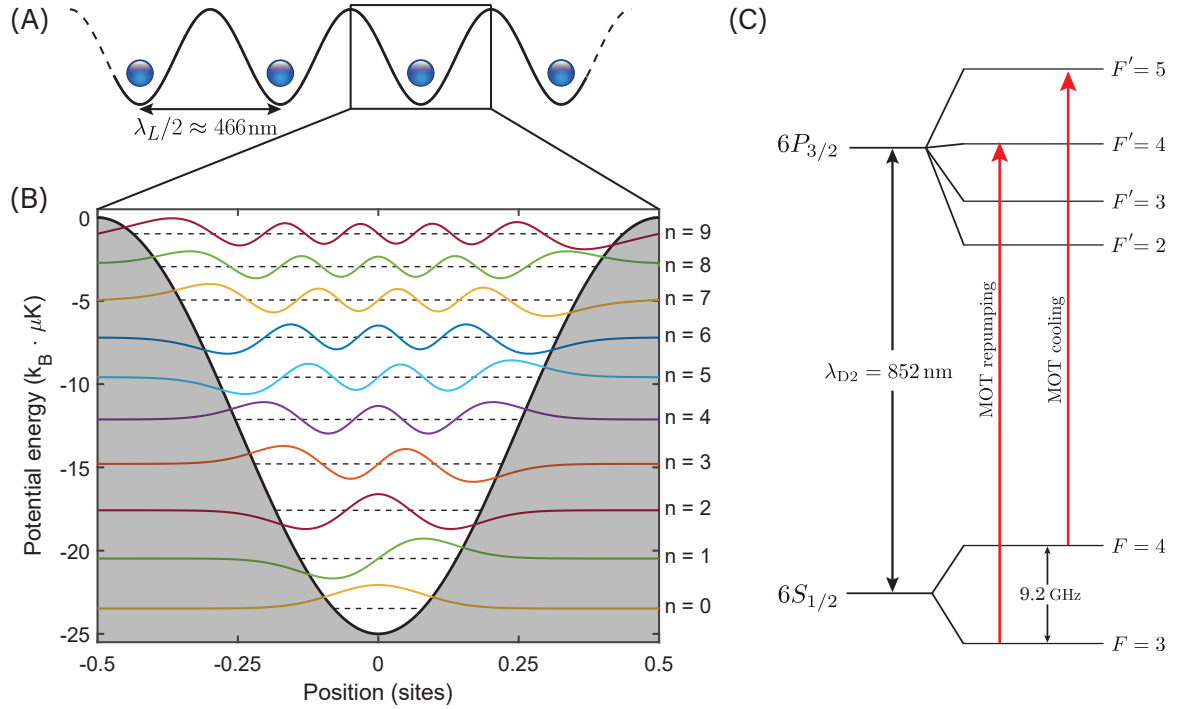


Figure 2.1: **Cesium atoms in optical lattices.** (A) Illustration of our optical lattice formed by two counter-propagating laser beams with a wavelength of $\lambda \approx 866\text{nm}$. The blue spheres represent ^{133}Cs atoms trapped by the optical lattice potential as explained in Sec. 2.1.2. (B) The trapped atoms not only have internal (spin) degrees of freedom but also external degrees of freedom given by the motional levels determined by the trapping potential. Here, the wave function amplitude of the first 10 bounded eigenstates are illustrated (colorful solid lines). Each wave function is vertically shifted by its corresponding energy (horizontal dashed lines) for illustration purposes. (C) ^{133}Cs D2 line level scheme. The two red arrows indicate the transitions induced by the MOT cooling ($F = 4 \rightarrow F' = 5$) and repumping ($F = 3 \rightarrow F' = 4$) beams.

After the atoms are trapped and cooled by the MOT, they are transferred to the lattice potential (described in Sec. 2.1.2) which is formed by two counter-propagating beams that form a one-dimensional lattice that intersects the MOT's center. The atoms are therefore transferred to the lattice by simply turning the magnetic field gradient off¹. Once the atoms are in the lattice, the temperature is further reduced by sub-Doppler cooling. Such technique cools down the atoms beyond the Doppler limit by means of polarization gradient cooling [52] (also known as Sisyphus effect), reaching temperatures on the order of $10\ \mu\text{K}$ for a trap depth of² $80\ \mu\text{K}$. After the sub-Doppler cooling, the MOT beams are turned off and the atoms are only trapped by the lattice potential. The storage time (half-life) of the atoms in the lattice is around 6 s , limited by phase noise of the lattice beams [53], which is translated into position fluctuations of the lattice, see Sec. 2.1.6. The storage time is orders of magnitude longer than the duration of any physical process studied in this thesis.

¹ Before turning the magnetic field off, the current of the MOT coils is shortly increased in order to increase the field's gradient, therefore compressing the MOT cloud. Simultaneously, the current of the compensation coils is linearly swept in order to drag the MOT cloud along the lattice. This increases the transfer efficiency into the lattice.

² The exact temperature depends on the depth of the potential, for more details see Sec. 2.2.3

2.1.2 Optical dipole trap

In this section I explain the concept of spin dependent dipole trap potential, meaning that the potential experienced by the atoms depends on their internal spin state. The optical potential originates from the energy shift of the internal atomic energy levels produced by the interaction between the atom and the light field. The energy shift of the i 'th energy level, with unperturbed energy ε_i , is given by [49]

$$\Delta E_i = \sum_{j \neq i} \frac{|\langle j | \hat{\mathcal{H}}_1 | i \rangle|^2}{\varepsilon_i - \varepsilon_j}, \quad (2.1)$$

where $\hat{\mathcal{H}}_1 = -\hat{\mu} \cdot \mathbf{E}$ is the interaction component of the system's Hamiltonian $\hat{\mathcal{H}} = \hat{\mathcal{H}}_0 + \hat{\mathcal{H}}_1$ with $\hat{\mu} = -e\mathbf{r}$ being the electric dipole operator. For illustration purposes, let us first consider a two-level system. According to Eq.(2.1), the energy shift on the ground state of a two level system is

$$\Delta E = \frac{3\pi c^2 \Gamma}{2\omega_0^3 \Delta} I, \quad (2.2)$$

where ω_0 is the atomic transition frequency, c is the speed of light, I is the intensity of the lattice beams, Δ is the detuning between the atomic transition and the laser beam and Γ is the decay rate of the atomic transition. From Eq.(2.2), it is clear that the energy shift of the ground state is attractive for a red-detuned light field and repulsive for a blue-detuned light field.

In our experiment we work with ^{133}Cs whose fine structure level scheme is shown in Fig. 2.2A. The fine-structure splitting arises from the interaction between the orbital angular momentum and the electron's spin. Particularly, the ground state $6^2S_{1/2}$ is split in two levels here denoted $|\uparrow_{\text{fine}}\rangle$ and $|\downarrow_{\text{fine}}\rangle$ corresponding to $m_J = 1/2$ and $-1/2$ respectively. According to Eq.(2.2), given a light field with a frequency in between the D1 and D2 lines, the σ^+ -polarized component of the light field produces a potential on $|\downarrow_{\text{fine}}\rangle$ containing an attractive contribution and a repulsive contribution, while the σ^- -polarized component has the same effect on $|\uparrow_{\text{fine}}\rangle$. A properly chosen lattice wavelength produces a complete cancellation between the attractive and repulsive forces in such a way that the potential on $|\uparrow_{\text{fine}}\rangle$ only depends on the intensity of the σ^+ -polarized lattice component while the potential on $|\downarrow_{\text{fine}}\rangle$ only depends on the intensity of the σ^- -polarized lattice component. A computation including higher energy levels [54] yields a value of $\lambda = 865.9$ nm known as the magic wavelength.

The fine splitting of the ground state on the two spin states $|\uparrow_{\text{fine}}\rangle$ and $|\downarrow_{\text{fine}}\rangle$ doesn't take into account the interaction with the nuclear spin. Such interaction produces the well known hyperfine splitting shown in Fig. 2.2B. For the measurements presented in this thesis we have used three out of the 16 hyperfine levels of the ground state: $|4, 4\rangle := |F = 4, m_F = 4\rangle$, $|4, 3\rangle := |F = 4, m_F = 3\rangle$ and $|3, 3\rangle := |F = 3, m_F = 3\rangle$. They can be written in terms of the fine splitting states $|\uparrow_{\text{fine}}\rangle$ and $|\downarrow_{\text{fine}}\rangle$:

$$|4, 4\rangle = |I = \frac{7}{2}, m_I = \frac{7}{2}\rangle \otimes |\uparrow_{\text{fine}}\rangle, \quad (2.3)$$

$$|3, 3\rangle = -\sqrt{\frac{1}{8}} |I = \frac{7}{2}, m_I = \frac{7}{2}\rangle \otimes |\uparrow_{\text{fine}}\rangle + \sqrt{\frac{7}{8}} |I = \frac{7}{2}, m_I = \frac{7}{2}\rangle \otimes |\downarrow_{\text{fine}}\rangle, \quad (2.4)$$

$$|4, 3\rangle = -\sqrt{\frac{7}{8}} |I = \frac{7}{2}, m_I = \frac{7}{2}\rangle \otimes |\uparrow_{\text{fine}}\rangle + \sqrt{\frac{1}{8}} |I = \frac{7}{2}, m_I = \frac{7}{2}\rangle \otimes |\downarrow_{\text{fine}}\rangle. \quad (2.5)$$

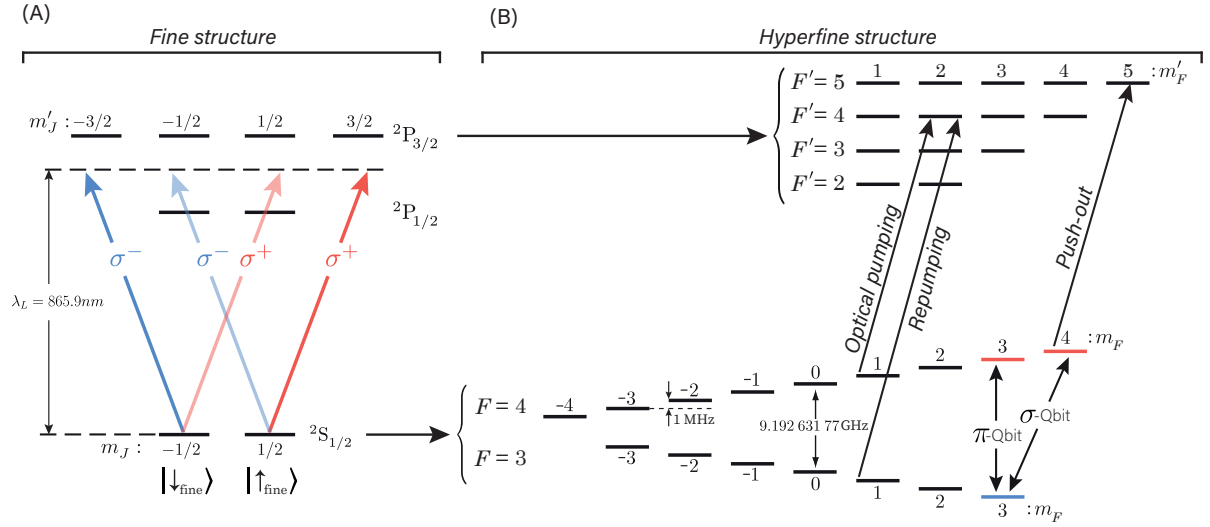


Figure 2.2: ^{133}Cs fine and hyperfine level schemes [46]. **(A)** Fine structure level scheme. The lattice wavelength $\lambda = 865.9 \text{ nm}$ corresponds to the so called magic wavelength (horizontal dashed line). It is red detuned from the D2 transition $^2S_{1/2} \rightarrow ^2P_{3/2}$ and blue detuned from the D1 transition $^2S_{1/2} \rightarrow ^2P_{1/2}$. The $|\uparrow_{\text{fine}}\rangle$ state experiences an attractive potential from the σ^+ -polarized component, which only has a contribution from the D2 line, and no potential from the σ^- -polarized component since the D1 and D2 line contributions cancel each other. For the $|\downarrow_{\text{fine}}\rangle$ state the opposite happens. **(B)** Hyperfine structure level scheme. The $^2S_{1/2}$ orbital splits in 16 hyperfine levels. The optical pumping ($F = 4 \rightarrow F' = 4$) and repumping ($F = 3 \rightarrow F' = 4$) beams are used to prepare the atoms in the $|4, 4\rangle$ state. The push-out beam ($F = 4 \rightarrow F' = 5$) is used to remove atoms in $F = 4$ by radiation pressure without removing atoms in $F = 3$. The pair of states $|3, 3\rangle \leftrightarrow |4, 4\rangle$ is called the σ -Qubit, while the pair $|3, 3\rangle \leftrightarrow |4, 3\rangle$ is called π -Qubit.

Therefore, the potential of each of the three states in a one-dimensional lattice is given by³

$$U_{|4,4\rangle}(\vec{r}) = \alpha I_{\sigma^+}(\vec{r}), \quad (2.6)$$

$$U_{|3,3\rangle}(\vec{r}) = \frac{1}{8}\alpha I_{\sigma^+}(\vec{r}) + \frac{7}{8}\alpha I_{\sigma^-}(\vec{r}), \quad (2.7)$$

$$U_{|4,3\rangle}(\vec{r}) = \frac{7}{8}\alpha I_{\sigma^+}(\vec{r}) + \frac{1}{8}\alpha I_{\sigma^-}(\vec{r}), \quad (2.8)$$

where α is a constant that depends on cesium polarizability, and $I_{\sigma^\pm}(\vec{r})$ is the intensity of the σ^\pm -polarized component of the light field at the position \vec{r} . In our case, we trap the atoms in a one-dimensional lattice formed by two counter-propagating linearly-polarized laser beams with Gaussian profiles and equal powers. Since the linear polarization can be decomposed into left and right-circular polarization components with equal amplitudes, we effectively have two superimposed lattices, one σ^+ -polarized and one σ^- -polarized. The intensity profile of the two lattice components is

$$I_{\sigma^\pm}(x, r) = \frac{4P}{\pi w^2(x)} e^{-2r^2/w^2(x)} \cos^2[k(x - x_\pm)], \quad (2.9)$$

³ The contribution of I_{σ^+} and I_{σ^-} to the potential depends on the lattice wavelength. The expressions here given correspond to the magic wavelength. A different wavelength can be chosen such that $U_{|3,3\rangle}$ only depends on I_{σ^-} while $U_{|4,3\rangle}$ only depends on I_{σ^+} . Such configuration is optimal for certain measurements here presented. However, a change of lattice wavelength requires a major re-optimization of the setup, which given the time constraint we have decided not to do.

where x and r are the longitudinal and transverse positions, $k = 2\pi/\lambda$ with λ being the lattice wavelength, $w(x)$ is the Gaussian waist at x , P is the power of each of the two counter-propagating beams and x_{\pm} is the position of the σ^{\pm} -polarized lattice.

Using Eq.(2.9), the three potential landscapes in Eqs.(2.6-2.8) can be written as a sinusoidal potential with a depth and offset that depend on the relative position between the two σ -polarized lattices (see Fig. 2.3).

$$U_{|4,4\rangle}(x) = -U(0) \cos^2 [k(x - x_+)], \quad (2.10)$$

$$U_{|3,3\rangle}(x) = -U(x_+ - x_-) \cos^2 [k(x - x_{\text{pos}}(x_-, x_+))] - U_{\text{offs}}(x_+ - x_-), \quad (2.11)$$

$$U_{|4,3\rangle}(x) = -U(x_+ - x_-) \cos^2 [k(x - x_{\text{pos}}(x_+, x_-))] - U_{\text{offs}}(x_+ - x_-), \quad (2.12)$$

with

$$U(x) = \frac{\alpha I_0}{8} \sqrt{50 + 14 \cos(2kx)} \quad (2.13)$$

$$U_{\text{offs}} = \frac{\alpha I_0}{2} - \frac{U(x)}{2} \quad (2.14)$$

$$x_{\text{pos}}(x_1, x_2) = \frac{\lambda}{4\pi} \arctan \left(\frac{7 \sin(2kx_1) + \sin(2kx_2)}{7 \cos(2kx_1) + \cos(2kx_2)} \right), \quad (2.15)$$

where we restricted ourselves to the positions along the lattice axis ($r = 0$), we assume that x is much smaller than the Rayleigh length⁴ ($w(x) \approx w(0)$), and $I_0 = 4P/(\pi w^2(0))$ represents the peak intensity of each σ -polarization component.

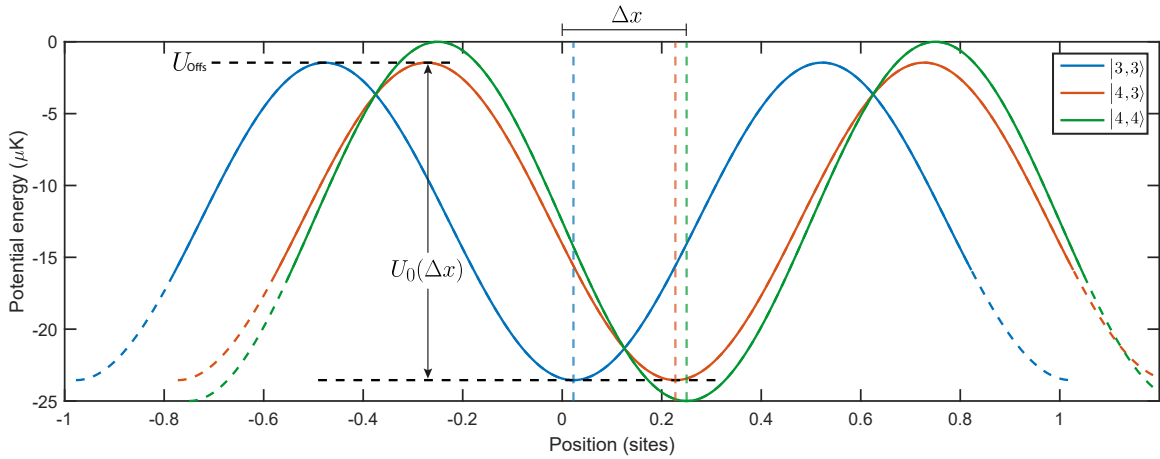


Figure 2.3: **Spin dependent optical lattice potential.** The three states $|3, 3\rangle$, $|4, 3\rangle$ and $|4, 4\rangle$ experience different potential landscapes when there is a relative displacement $\Delta x = x_+ - x_-$ between the two σ -polarized lattice components, Eqs.(2.10-2.12). The three curves here shown correspond to $x_+ = 0.25\lambda/2$ and $x_- = 0$. The position of $U_{|4,4\rangle}$ only depends on x_+ , its amplitude is independent of both x_- and x_+ , and it has zero vertical offset. On the other hand, $U_{|3,3\rangle}$ and $U_{|4,3\rangle}$ both acquire a vertical offset Eq.(2.14), their depth U is reduced Eq.(2.13) and their effective positions depend on both x_- and x_+ , Eqs.(2.11, 2.12 and 2.15).

⁴ In our experiment, the atoms are loaded within a range of less than 200 lattice sites, which is one order of magnitude smaller than the Rayleigh length $z_R = \pi\omega_0^2/\lambda$

2.1.3 Spin state preparation

As already mentioned in Sec. 2.1.2, for the measurements presented in this thesis only the three hyperfine levels $|3, 3\rangle$, $|4, 3\rangle$ and $|4, 4\rangle$ are used. However, after the atoms are trapped by the MOT and transferred into the lattice, they are homogeneously distributed along the 16 different hyperfine levels of $6^2S_{1/2}$, Fig. 2.2. This is why every measurement sequence starts with a spin state preparation that transfers all atoms into the outermost hyperfine state $|4, 4\rangle$. This is done by optical pumping, a well known technique developed in the 50's by the Nobel prize winner Alfred Kastler [55].

To prepare the atoms in the target state $|4, 4\rangle$, a σ^+ -polarized optical pumping beam, frequency-locked to the $|F = 3\rangle \rightarrow |F' = 4\rangle$ transition, shines the atoms in the direction of the quantization axis defined by a nearly homogeneous magnetic field of 3 G parallel to the lattice⁵. The magnetic quantum number of the atom increases by one unit for every absorbed photon $m_F \rightarrow m_F + 1$, until it reaches the target state $m_F = 4$. The atoms decaying to the $F = 3$ are pumped back by a repumper beam locked to the $|F = 3\rangle \rightarrow |F' = 4\rangle$ transition, see Fig. 2.2B. Importantly, $|4, 4\rangle$ is a dark state because there are no resonant transitions induced by the σ^+ -polarized optical pumping and repumper beams. This reduces the probability of heating the atoms that have already reached the target state. Once the atoms reach $|4, 4\rangle$ and the pumping beams are turned off, the hyperfine sublevel lifetime is limited by off-resonant scattering with lattice photons [56, 57], to around 100 ms (half-life) [58]. This doesn't pose a problem for the measurements presented in this thesis since it is at least three orders of magnitude longer than the physical processes here studied.

2.1.4 Microwave driving and σ -Qubit

The atoms initially prepared in $|4, 4\rangle$ can be transferred to $|3, 3\rangle$ by a microwave driving field that couples the two states with a Rabi frequency⁶ $\Omega_{\text{MW}} = \langle 3, 3 | \hat{\mu} \vec{B} | 4, 4 \rangle / \hbar$ [59, 60]. In order to address a specific transition between hyperfine levels, the quantization axis field of 3 G lifts the degeneracy by 1.05 MHz between consecutive levels [46], allowing us to exclusively couple the two hyperfine states $|4, 4\rangle$ and $|3, 3\rangle$, Fig 2.2B. This way we avoid populating any of the other hyperfine states during the microwave driving. This means that we effectively have a two level system that we call σ -Qubit, because the transition requires an angular momentum change of $m_F \rightarrow m_F \pm 1$.

The microwave driving field is generated by a horn placed close to the glass cell with which Rabi frequencies of up to 50 kHz are reached. A detailed description of the microwave generation setup can be found in [50]. Given a certain Rabi frequency, any desired superposition of the two σ -Qubit states is obtained by controlling the length of the microwave pulses.

2.1.5 Raman driving and π -Qubit

As mentioned in Sec. 2.1.4, with microwave driving we reach Rabi frequencies up to 50 kHz. However, for the measurements presented in Chapter 4, frequencies of up to the MHz regime were needed. To reach the required Rabi frequencies we couple the two hyperfine states $|4, 3\rangle$ and $|3, 3\rangle$ with a pair of Raman beams. The Raman coupling allows us to reach much higher transition frequencies even though it is a two-photon process as opposed to the microwave transition that is a one-photon process. This is due to the fact that the microwave field couples the two states by a magnetic dipole transition while the Raman driving field couples the two states by electric dipole transitions [61]. Additionally, the Raman transitions used here are driven by optical driving fields and can therefore be focused to achieve high

⁵ The magnetic field that defines the quantization axis is generated by a pair of coils in Helmholtz configuration [50]

⁶ Electric dipole transitions are forbidden due to selection rules.

intensities. Analogously to the σ -Qubit, the two states $|4, 3\rangle$ and $|3, 3\rangle$ effectively form a two level system that we call π -Qubit, because the transition preserves the atom's angular momentum (see Fig 2.2B).

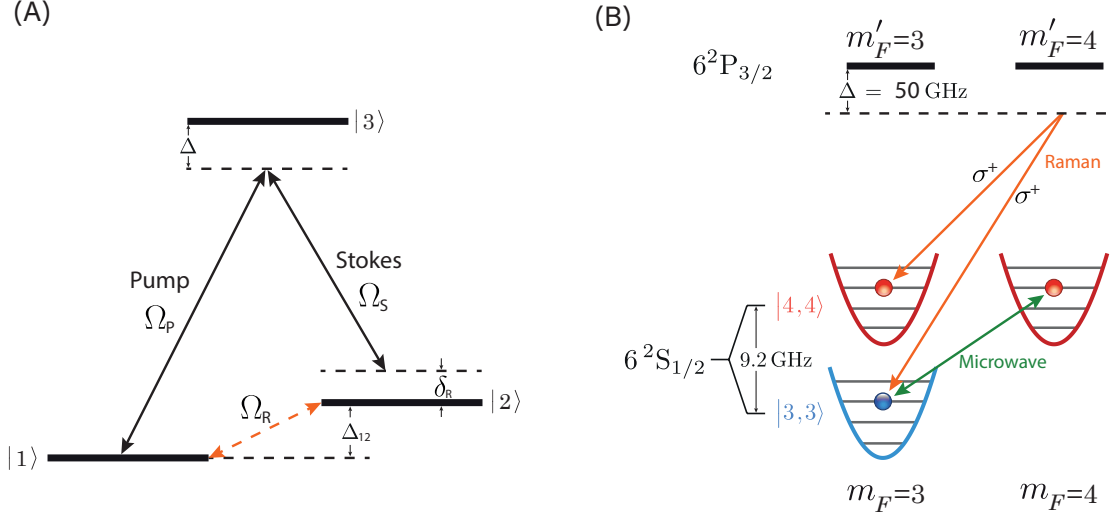


Figure 2.4: **Raman and microwave transitions.** (A) A Raman transition between two states $|1\rangle$ and $|2\rangle$ is a two-photon process induced by two beams whose relative frequency difference $\Delta_{12} + \delta_R$ is close to the energy difference between $|1\rangle$ and $|2\rangle$ up to a possible detuning δ_R . Both beams have a detuning Δ from a third excited level $|3\rangle$. The atom is excited from its initial state $|1\rangle$ by the pump beam and decays to $|2\rangle$ emitting a photon stimulated by the Stokes beam. The process effectively couples $|1\rangle$ and $|2\rangle$ with a Rabi frequency Ω_R . (B) In our system, the Raman transitions are used to transfer the atoms between the $|3, 3\rangle$ and $|4, 3\rangle$ states (π -Qubit) with a pair of σ^+ -polarized beams. on the other hand, microwave transitions are used to transfer atoms between the $|3, 3\rangle$ and $|4, 4\rangle$ states (σ -Qubit) with a single-photon process induced by a resonant microwave driving field.

A Raman transition between two states $|1\rangle$ and $|2\rangle$ consists of a two photon process induced by a pair of off-resonant beams, detuned by a frequency Δ from a third excited level $|3\rangle$, and whose relative frequency difference is near the transition frequency Δ_{12} between $|1\rangle$ and $|2\rangle$ (see Fig.2.4A). The atom initially prepared in $|1\rangle$ is excited by a photon from the pump beam and then decays to $|2\rangle$ emitting a photon stimulated by the Stokes beam. In the case of Raman transitions between hyperfine levels of ^{133}Cs ground state, the Rabi frequency of the transition is [62]

$$\Omega_R = \sqrt{X(m_F)} \frac{\Omega_S \Omega_P}{2\Delta} \quad (2.16)$$

where Ω_P and Ω_S are the single-photon Rabi frequencies of the resonant optical transitions induced by the pump and Stokes beams respectively, m_F is the magnetic quantum number of the lower level ($F = 3$), and $X(m_F)$ is a factor that depends on the polarization of the two beams

$$X(m_F) = \begin{cases} \frac{1}{288}(4 + m_F)(5 + m_F) & : (\pi, \sigma^-), (\sigma^+, \pi) \\ \frac{1}{288}(4 - m_F)(5 - m_F) & : (\pi, \sigma^+), (\sigma^-, \pi) \\ \frac{1}{9} \left[1 - \left(\frac{m_F}{4} \right)^2 \right] & : (\sigma^+, \sigma^+), (\sigma^-, \sigma^-) \\ 0 & : (\pi, \pi), (\sigma^\pm, \sigma^\mp) \end{cases} \quad (2.17)$$

where the two terms in parenthesis denote the polarization of the pump and Stokes beams respectively.

For the measurements presented in chapter 4, we need to couple the two π -Qubit states instead of the σ -Qubit states that we couple by microwave driving. This is because the potential landscapes experienced by the two π -Qubit states are equal between them up to a longitudinal displacement, while the σ -Qubit states experience potential landscapes with different depth and vertical offset (see Fig. 2.3). Having equal potentials for the two spin states is essential for the interferometric measurements presented in chapter 4, where the eigenstates of the two potentials need to coincide (up to a spatial displacement). From Eq. (2.17) we know that the highest coupling (given that in our case $m_F = 3$) is obtained with the (π, σ^-) or (σ^+, π) configurations resulting in $X(m_F) = 0.1944$. However, those configurations do not couple the π -Qubit states. The only two configurations that produce a non-zero coupling between the π -Qubit states are (σ^+, σ^+) and (σ^-, σ^-) which result in $X(m_F) = 0.0486$. The two configurations work equally well for our purpose; we have simply chosen the (σ^+, σ^+) configuration (see Fig. 2.4B) because it was easier to implement in the setup. The Raman beams are overlapped with the σ^+ polarized lattice beam and they thus go through the same optics before reaching the atoms. The beams have a Gaussian profile with a waist of around $17 \mu\text{m}$. Such a small waist means we have a high intensity at the position of the atoms, which translates in high Rabi frequencies. With a detuning of around $\Delta = 50 \text{ GHz}$ we reach Rabi frequencies up to $\Omega_R = 6.5 \text{ MHz}$.

2.1.6 Lattice depth and position control

As we have already seen in Sec. 2.1.2, the position and depth of the potential experienced by the different hyperfine states $|4, 4\rangle$, $|4, 3\rangle$ and $|3, 3\rangle$ depends on the position and intensity of the two σ -polarized lattice components according to Eqs. (2.10-2.12). In this section I explain how the intensity and position of the two lattice components are actively controlled using acousto-optic modulators (AOM) in closed feedback loops. A more detailed explanation can be found in [53, 58].

One of the two counter-propagating lattice beams, called non-synthesized arm, has a fixed linear polarization and only its intensity is actively controlled with the help of an AOM in a closed feedback loop as shown in Fig. 2.5A. A fraction of the beam's power is reflected by a pickup plate into a photodiode. The photodiode's signal is compared to a reference voltage produced by an arbitrary waveform generator. The voltage difference between the photodiode and the reference is used as an error signal and sent to a lock box⁷, whose output is mixed with an 80 MHz RF signal generated by a DDS⁸. The mixed RF signal is finally used to drive the AOM which controls the beam's intensity, therefore closing the feedback loop.

The opposite counter-propagating lattice beam, called synthesized arm, is controlled with two AOMs. Each AOM controls the phase and intensity of each σ -polarized component. Initially, the beams corresponding to the σ^+ and σ^- components are horizontally and vertically polarized respectively. A quarter wave plate⁹ transforms the horizontally polarized beam into a left-circularly polarized beam and the vertically polarized beam into a right-circularly polarized beam.¹⁰ Two independent loops, like the one used for the non-synthesized arm, are used to actively control the intensity of each component. A wollastone prism is used to split the horizontal and vertical polarization components in order to control the two components independently (see intensity control box in Fig. 2.5B).

The phases of the two synthesized-arm components are actively controlled by two independent optical phase-locked loops (see phase control box in Fig. 2.5B). To achieve this, a fraction of their power is

⁷ A proportional-double-integral-derivative (PI2D) lock box D2-125 from Vescent Photonics

⁸ Direct digital synthesizer AD9954 from Analog Devices

⁹ Since wave plates are never perfect, we actually use two (imperfect) quarter wave plates to produce the desired polarization

¹⁰ The quantization axis points in the same direction as the non-synthesized arm. The right-circularly polarized beam of the synthesized arm therefore corresponds to the σ^- component while the left-circularly polarized corresponds to the σ^+ component

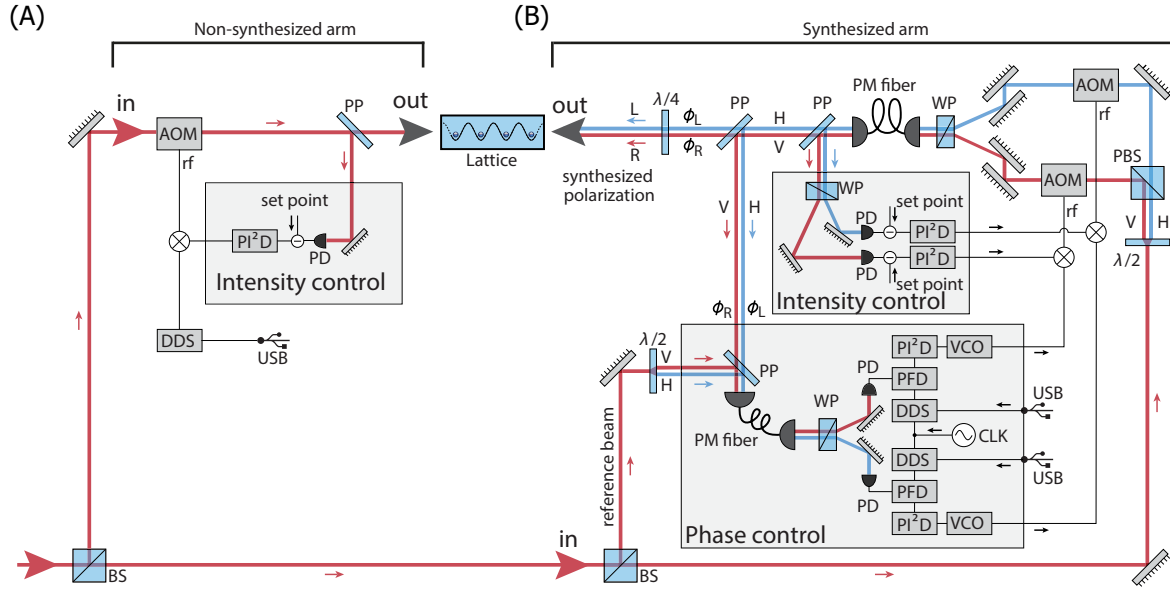


Figure 2.5: **Intensity and phase control of the lattice beams.** The two counter propagating laser beams that form the lattice are obtained from a common beam, split by a beam splitter (BS). One beam forms the non-synthesized arm (A) and the other one forms the synthesized arm (B). The setup shown in B is called polarization-synthesizer and is capable of producing any desired polarization (figure taken from [53]). The polarization of the non-synthesized arm is fixed, and only its intensity is controlled by a feedback loop. The polarization and amplitude of the two polarization components are controlled by four independent feedback loops as explained in the main text. The abbreviations are acousto-optic modulator (AOM), reference clock (CLK), direct digital synthesizer (DDS), horizontal linear polarization (H), polarizing beam splitter (PBS), photodiode (PD), phase-frequency detector (PFD), proportional-double-integral-derivative controller (PI²D), polarization maintaining (PM), pickup plate (PP), radio frequency (rf), universal serial bus (USB), vertical linear polarization (V), voltage-controlled oscillator (VCO), Wollaston prism (WP), half-wave plate ($\lambda/2$), and quarter-wave plate ($\lambda/4$).

reflected by a pickup plate after they have gone through their corresponding AOMs. Additionally, a fraction of the power is picked up before the AOMs and is used as a reference. The beams picked up before and after the AOM are overlapped¹¹, producing a beating signal with a frequency of around 80 MHz, corresponding to the frequency of the RF driving of the AOM. The beating signal, detected with a fast photodiode¹², is compared with a phase frequency discriminator¹³ to a reference RF signal generated by a DDS¹⁴. The phase difference is used as an error signal and sent to a lock box¹⁵, whose output controls a voltage controlled oscillator that finally drives the AOM. The phase of each beam can then be controlled by tuning the phase of the two separate reference RF signals produced by the DDS. The

The position of the two lattice components x_{\pm} are directly related to the relative phase between the two

¹¹ Similarly to the intensity control loop, the two polarization components are split by a wollastone prism in order to independently control the two components.

¹² Hamamatsu G4176-03

¹³ MC100EP140, ON Semiconductor

¹⁴ Direct digital synthesizer AD9954 from Analog Devices

¹⁵ A proportional-double-integral-derivative (PI²D) lock box D2-125 from Vescent Photonics

counter-propagating beams according to the following expression

$$x_{\pm} = \frac{\lambda (\phi_{\pm} - \phi_0)}{2 \cdot 2\pi}, \quad (2.18)$$

where ϕ_{\pm} is the phase of the synthesized beam corresponding to the σ_{\pm} -polarized component and ϕ_0 is the phase on the non-synthesized beam. This way, the position of the two lattice components are computer controlled via the DDS. The optical phase-locked loop reaches a bandwidth of around 800 kHz and a slew rate of $0.84 \text{ rad } \mu\text{s}^{-1}$. This is particularly important for the measurements presented in Chap. 5.

2.2 External degrees of freedom

Besides the internal degrees of freedom, the atomic quantum state has external degrees of freedom. The trapped atom can populate different motional energy levels (eigenstates) given by the solutions of the Schrödinger equation for an atom in the lattice potential. An example of the solutions for a potential depth of $25 \mu\text{K}$ is shown in Fig. 2.1B where the wave functions corresponding to the first 10 levels are plotted¹⁶. The following chapters in this thesis are devoted to study the external degrees of freedom, meaning the dynamics of the atomic wave packet in the trapping potential. The ability to control the internal atomic degrees of freedom (Sec. 2.1) is rather used as a tool to study the wave packet dynamics. In the following sections, the methods used to control and monitor the external degrees of freedom of the atoms trapped in the lattice potential are presented.

2.2.1 Motional ground state preparation

In Sec. 2.1.1 we have seen that after sub-Doppler cooling the temperature of the atoms is on the order of $10 \mu\text{K}$, corresponding to a ground state (lowest motional energy level) population of around 40%. In this section I describe the cooling technique, first realized by Förster et al., [64], used to increase the longitudinal ground state population up to around 98%. Cooling the atoms down to the motional ground state is desirable to avoid inhomogeneous effects [60]. Moreover, the state preparation in a single motional energy level is essential for the measurements discussed in Chapters 3, 4 and 5.

The cooling technique consists of a cycle that reduces the motional energy level of the atom using sideband-resolved microwave transitions. Sideband-resolved here means that the microwave pulses are spectrally narrower than the spacing between consecutive energy levels $\omega_{\text{vib}} = \omega_{n+1} - \omega_n$ where $\hbar\omega_n$ is the energy of the n^{th} level (see Fig. 2.6). This way it is possible to address transitions on a specific sideband. Particularly, transitions on cooling sidebands $n \rightarrow m$ with $m < n$ reduce the energy of the atom by $n - m$ energy quanta. The cycle used to cool the atoms to the ground state addresses the first cooling sideband to transfer the atoms from the motional level n of $|4, 4\rangle$ to the motional level $n - 1$ of $|3, 3\rangle$ (see Fig. 2.6). The atoms are then pumped back by the repumper beam ($F = 3 \rightarrow F' = 4$) and decay back, closing the cycle¹⁷. Importantly, the ground state of $|4, 4\rangle$ is a dark state of the process since there are no more resonant transitions once the atom reaches that state.

One essential ingredient that is required for the cooling process to work is the coupling between different motional levels. The local minima of the lattice potential are nearly harmonic, and it is well known that the wave functions corresponding to different energy levels in a harmonic potential are orthogonal. This means that the microwave driving field cannot couple different motional levels as long

¹⁶ The solutions are obtained numerically using the Strang split-step integration method [63]

¹⁷ If the atom decays to $F = 4$ with $m_F < 4$, the atom is pumped back to $|4, 4\rangle$ by the σ^+ -polarized optical pumping beam ($F = 4 \rightarrow F' = 5$) which is also turned on during the whole cooling process

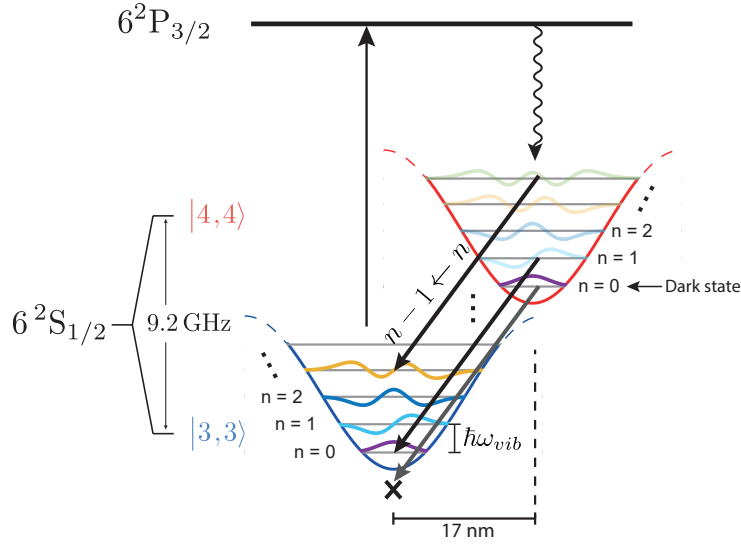


Figure 2.6: **Motional ground state cooling.** The microwave driving induces a transition from the motional level n of $|4, 4\rangle$ to the motional level $(n - 1)$ of $|3, 3\rangle$, therefore reducing the energy of the atom. The repumping beam ($F = 3 \rightarrow F' = 4$) transfers the atom to $6^2P_{3/2}$ from where it decays back to close the cycle. Once the atom reaches the ground state of $|4, 4\rangle$ there are no resonant transitions available, making it a dark state.

as the potentials corresponding to $|4, 4\rangle$ and $|3, 3\rangle$ are equal. Therefore, in order to enable the microwave sideband transitions, one of the spin potentials is longitudinally displaced by around $\Delta x = 17$ nm, lifting the orthogonality between different motional states [65] (see Fig. 2.6).

There are two sources of heating during the cooling cycle [65]: recoil heating and projection heating. The recoil heating is induced by the absorption and spontaneous emission of the microwave photons

$$\Delta E_{\text{rec}} = \hbar^2 k^2 / m, \quad (2.19)$$

where k is the wave vector of the microwave driving field. The projection heating, on the other hand, is produced by the non-vanishing projection of the motional states of $|3, 3\rangle$ onto the motional states of $|4, 4\rangle$ during the repumping process. The average energy increase per cycle repetition due to projection heating in the harmonic approximation is [65]

$$\Delta E_{\text{proj}} = m\omega_{\text{vib}}^2 \Delta x^2 / 2, \quad (2.20)$$

where $\hbar\omega_{\text{vib}}$ is the energy difference between consecutive vibrational levels and Δx is the relative displacement between the two lattice components. The effective energy change over one cooling cycle is then

$$\Delta E_{\text{tot}} = \Delta E_{\text{rec}} + \Delta E_{\text{proj}} - \hbar\omega_{\text{vib}}. \quad (2.21)$$

The condition to cool the atoms is $\Delta E_{\text{tot}} < 0$, known as Lamb-Dicke regime [65, 66]. In our case, the recoil heating is orders of magnitude smaller than $\hbar\omega_{\text{vib}}$ and can be neglected. The lattice displacement is chosen to be $\Delta x = 17$ nm which is a trade off between a high coupling between consecutive motional levels and a small projection heating.

The microwave sideband cooling only reduces the axial temperature of the atoms. However, some measurements, particularly the ones presented in Chap. 5, are sensitive to the transverse temperature of the atoms as well. In order to reduce the transverse temperature of the atoms, during molasses cooling

we superimpose to the optical lattice a blue-detuned donut-shaped beam. Thereby, we increase the confinement of the atoms in the direction transverse to the optical lattice. By subsequently ramping down the intensity of the donut beam adiabatically, we lower the transverse temperature of the atoms approximately by a factor of 3 (see Sec. 2.2.3). For more details about the donut-shaped beam see [58].

2.2.2 Robust measurement of motional ground state population

For the measurements presented in Chapter 5, a robust measurement of the ground state population fraction P_0 is required. One technique to obtain the ground state population, previously used in this group, consists in measuring the population fraction p_e^{cool} transferred by a microwave π -pulse tuned to the cooling sideband ($n \rightarrow n - 1$) and the fraction p_e^{heat} transferred by an equal pulse tuned to the heating sideband ($n \rightarrow n + 1$). The ground state population is then $P_0 = 1 - p_e^{\text{cool}}/p_e^{\text{heat}}$ [67]. However, since the spectral widths and positions of the sidebands depend on the temperature of the atoms [68], multiple points are needed in order to determine the height of each sideband.

We have used a more suitable technique, first proposed in [65], which requires a single point to determine the ground state population fraction. The technique consists in selectively removing from the trap all the atoms that populate higher motional states while retaining those in the ground state. To achieve this, all atoms are first transferred from $|4, 4\rangle$ to $|3, 3\rangle$ with a microwave π -pulse on the carrier transition, ($n \rightarrow n$) therefore preserving the population distribution of the motional levels¹⁸. Subsequently, the relative position $x_\uparrow - x_\downarrow$ between the σ^+ and σ^- components of the lattice is adiabatically increased from zero to around 17 nm to maximize the overlap between consecutive motional levels [65] i.e. maximize the efficiency of the microwave transitions on the motional sidebands. At this point, a 10-repetition removal cycle begins. The cycle starts with a microwave π -pulse resonant to the first cooling sideband ($n \rightarrow n - 1$) that transfers all atoms to $|4, 4\rangle$ except those in the ground state. The atoms transferred to $|4, 4\rangle$ are then removed by radiation pressure with a D2-line beam resonant to the $|F = 4\rangle \rightarrow |F' = 5\rangle$ transition. The ground state population is given by the remaining population fraction after the removal cycle finishes. The multiple repetitions of the removal cycle are required to: 1) Ensure that all excited atoms are removed, in spite of the imperfect efficiency of the $|3, 3\rangle \rightarrow |4, 4\rangle$ transfer. 2) Make the detection technique robust against changes of the longitudinal temperature of the atoms (i.e. equally accurate for high and low temperatures).

In Fig. 2.7B, two spectra measured with the technique previously described are shown. The horizontal axis corresponds to the frequency of the microwave driving field used for the 10 pulses of the pushout cycle. The power and duration of the pulses is the same for all points and is chosen so that the transfer on the first sideband ($n \rightarrow n \pm 1$) is maximized. The blue points correspond to atoms prepared in the longitudinal ground state as described in Sec. 2.2.1 while the orange points correspond to atoms not prepared in the ground state (only molasses cooling, see Sec. 2.1.1). The horizontal offset between the two spectra is on the order of 4 kHz and is within the long term fluctuations (on the order of hours) of the transition frequency due to external magnetic field fluctuations. The flat bottom of the 1st sideband makes the ground state population measurement robust against changes of the longitudinal temperature of the atoms as well as external magnetic field fluctuations.

The model used to fit the spectra is given by the following expression

$$P_{\text{GS}}(\nu) = B \sum_{n=0}^{\infty} p_n \left(1 - \sum_{m=0}^{\infty} \alpha_{n,m} e^{-\left(\frac{\nu - \nu_{\text{SB}} m}{\sqrt{2}\sigma}\right)^2} \right)^N, \quad (2.22)$$

¹⁸ This is done in a non-displaced lattice (no longitudinal displacement between σ^+ and σ^- components of the lattice) to suppress the transitions between different motional levels.

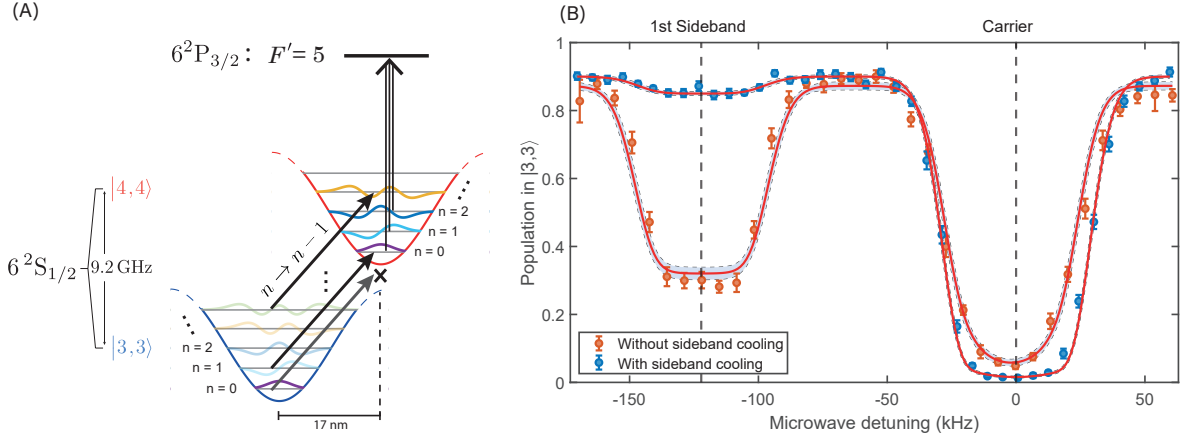


Figure 2.7: **Motional ground state population measurement.** (A) The ground state population is measured by removing all atoms except those that are in the ground state. The atoms that populate the excited motional levels are first transferred from $|3, 3\rangle$ to $|4, 4\rangle$ with a sideband-resolved microwave $\pi/2$ pulse. They are then removed from the lattice by radiation pressure with a beam resonant to the $F = 4 \rightarrow F' = 5$ transition. (B) Spectra measured with the sequence described in A, where the removal cycle was repeated 10 times. The horizontal axis is the frequency of the 10 microwave π -pulses. The vertical axis is the fraction of remaining atoms after the removal cycle. Orange points were measured with atoms that were not cooled into the longitudinal ground state, while blue points were measured with atoms cooled in the ground state with the method described in Sec. 2.2.1.

where B is the efficiency of the initial carrier π -pulse (from $|4, 4\rangle$ to $|3, 3\rangle$), p_n is the population probability of the n^{th} motional level, ν_{SB} is the longitudinal trap frequency, $\alpha_{n,m}$ is the π -pulse transfer efficiency from the n^{th} to the m^{th} level, σ is the spectral width of the π -pulse, and N is the number of repetitions of the pushout cycle (10 in our case). The sum over m corresponds to the different sidebands (each one at position $\nu_{\text{SB}}m$) while the sum over n corresponds to the contribution of the initial population p_n of each motional level to all sidebands. For the fits shown in Fig. 2.7B, the transfer efficiencies are theoretically computed from the Franck-Condon factors while the other parameters are free.

To understand the model, consider first the term corresponding to the sum over m

$$T_{\pi,n}(\nu) = \sum_{m=0}^{\infty} \alpha_{n,m} e^{-\left(\frac{\nu - \nu_{\text{SB}}m}{\sqrt{2}\sigma}\right)^2}. \quad (2.23)$$

This term represents the probability that an atom initially in the n^{th} motional level is transferred from $|3, 3\rangle$ to $|4, 4\rangle$ after a single π -pulse. This means, $(1 - T_{\pi,n})^N$ is the probability that the atom remains in $|3, 3\rangle$ after the N pushout repetitions. Therefore, given an ensemble of thermal atoms that populate the motional levels with probabilities p_n , the probability that the atoms remain in $|3, 3\rangle$ is given by the sum in Eq.(2.22), with B correcting for the fraction of the total population that is lost even before the removal cycle¹⁹. Notice that the term $1 - T_{\pi,n}$ has an inverted Gaussian-like shape and the N^{th} power is what produces the desired flat bottom.

¹⁹ The main contribution to the atom losses comes from the atoms that remain in $|4, 4\rangle$ after the initial carrier π -pulse. Those atoms are pushed out on purpose, otherwise they may be transferred to $|3, 3\rangle$ during the removal cycle

2.2.3 Measurement of potential depth and transverse temperature

The measurements presented in Chapter 5 require knowing the depth of the lattice potential U_0 as well as the transverse temperature T_{\perp} of the atoms after the state preparation. The two parameters are essential for the proper computation of the optimal control transport trajectories. In this section I explain the method used to simultaneously measure the two parameters.

When atoms prepared in the longitudinal ground state are transported by moving the lattice potential, the atoms may be heated up during the transport when the process is not adiabatic. The final longitudinal temperature of the atoms after transport, given a specific transport trajectory, depends on U_0 and T_{\perp} . Particularly, when the transport trajectory is linear, the process starts by a momentum kick (the lattice starts moving) that puts the atom in a coherent state that oscillates with a frequency that depends on the depth of the trapping potential. The transport then ends by a second momentum kick (the lattice stops moving) in the opposite direction. When the transport time is a multiple of the oscillation period, the atom goes back to the longitudinal ground state at the end of the transport, otherwise, the atom has a higher probability of populating the excited states. This is observed in the measurements shown in Fig. 2.8. The atoms were transported over a distance of one lattice site with a linear ramp, and the ground state population was measured with the technique presented in Sec. 2.2.2. The three plots in Fig. 2.8(A-C) correspond to measurements done in three different potential depths.

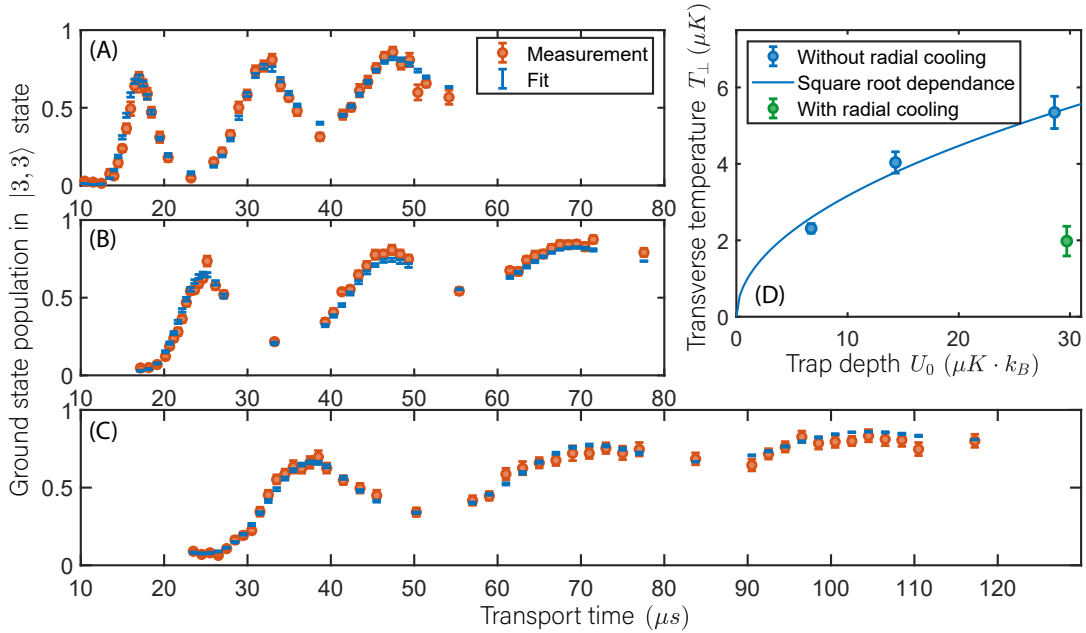


Figure 2.8: **Linear transport.** Atoms are transported by one lattice site with a linear transport ramp. The atoms receive a momentum kick at the beginning of the transport and a second momentum kick in the opposite direction at the end. For transport durations close to a multiple of the trapping period the ground state population after transport is close to unity, otherwise, they may end up in highly excited states. Here I show three examples of the measured ground state population after linear transport of different durations, in an optical lattice potential with a trap depth U_0 of (A) $(28.61 \pm 0.23) \mu\text{K}$ (B) $(14.31 \pm 0.13) \mu\text{K}$ and (C) $(6.72 \pm 0.06) \mu\text{K}$. The orange points are the measured ground state population and the blue points are the fit, from which the trap depth and transverse temperature are obtained. (D) transverse temperature versus trap depth U_0 obtained from the fit to the three measurements (blue points). The solid blue curve shows the expected square root scaling. The green point corresponds to the values obtained with radially cooled atoms.

The exact probability of occupying the ground state after a transport operation is obtained by simulating the wave packet evolution in the moving potential using the Strang split-step integration method [69]. More details on the simulation can be found in [63, 70]. The simulation takes into account the two-dimensional transverse distribution of the atoms assuming a Boltzmann distribution in a harmonic potential [65]

$$\mathcal{P}(r, T_{\perp}) = \frac{m\omega_{\perp}^2}{k_B T_{\perp}} r \exp\left(-\frac{m\omega_{\perp}^2 r^2}{2k_B T_{\perp}}\right), \quad (2.24)$$

where r is the transverse distance from the lattice axis and ω_{\perp} is the trapping frequency in the transverse directions. Moreover, given that the trapping frequency is two orders of magnitude smaller in the transverse directions than in the longitudinal direction, r is assumed to be constant during the transport duration (typically a few longitudinal oscillations). Since the lattice is formed by two counter-propagating beams with Gaussian profiles, the effective trap depth experienced by the atoms decreases with r and follows a Gaussian

$$U(r) = U_0 \exp\left(-\frac{2r^2}{w_{\text{DT}}^2}\right), \quad (2.25)$$

where w_{DT} is the waist of the lattice beams and $U_0 = U(0)$ is the depth along the axis. The ground state population after transport, for a thermal ensemble of atoms with transverse temperature T_{\perp} in a lattice potential of depth U_0 is then given by

$$P_{\text{GS}}(T_{\perp}, U_0) = \int_0^{\infty} dr P_{\text{GS}}(U(r)) \mathcal{P}(r, T_{\perp}), \quad (2.26)$$

where $P_{\text{GS}}(U(r))$ is the ground state population after transport assuming that all atoms experience a potential depth equal to $U(r)$.

The function in Eq.(2.26), with the integral replaced by a trapezoidal sum over about 10 different discrete values of r , is used as a fitting function on the data shown in Fig. 2.8. The free parameters are the transverse temperature T_{\perp} and the potential depth along the axis U_0 . This way, the linear transport is used as a thermometer to extract the transverse temperature of the atoms and the longitudinal potential depth. In Fig. 2.8D I plot the transverse temperature versus the trap depth obtained from the fits to the three measurements in Fig. 2.8(A-C). The transverse temperature clearly decreases with the trap depth, following a square root dependence. This is expected because the atoms are initially cooled by molasses cooling (see Sec. 2.1.1) in a potential depth of around 370 μK and then the depth is adiabatically lowered to the desired value. During the adiabatic lowering of the potential depth, the population distribution in the different motional levels is preserved, but the energy of each level decreases approximately proportional to the square root of the depth. This can be easily seen in the harmonic approximation where the energy of the n^{th} motional level is $E_n = (1/2 + n)\hbar\omega_{\text{HO}}$ with

$$\omega_{\text{HO}} = 2\pi \sqrt{\frac{2U_0}{m\lambda^2}}. \quad (2.27)$$

The harmonic approximation is reasonable given that only the first few bounded energy levels are populated after molasse cooling (at least 96% of the population is within the first half of the bounded states of the shallowest lattice used for the measurements). This explains the square root scaling of the temperature shown by the solid blue curve. The curve was computed based on the measurement corresponding to a depth of 28.61 μK , i.e. it shows the values expected from the square root scaling as computed from that single point.

As already mentioned in Sec. 2.2.1, the cooling in the transverse direction is improved by doing the

molasse cooling in a deeper transverse potential, induced by a blue-detuned donut-shaped beam that radially surrounds the atoms along the lattice. The donut-shaped beam is adiabatically turned off after molasse cooling therefore reducing the transverse temperature as shown by the green point in Fig. 2.8D.

2.2.4 Raman Ramsey interferometry

The measurements presented in chapter 3 and chapter 4 rely on quantifying the overlap between an evolving wave function and a reference wave function. For that purpose we use a technique called Ramsey interferometry which originated in the field of Nuclear Magnetic Resonance [71]. In this section I present the experimental sequence and the model used to extract both the modulus and phase of the overlap between the two wave functions. For simplicity, the two states of the π -Qubit will be simply called spin-up $|\uparrow\rangle := |4, 4\rangle$ and spin-down $|\downarrow\rangle := |3, 3\rangle$.

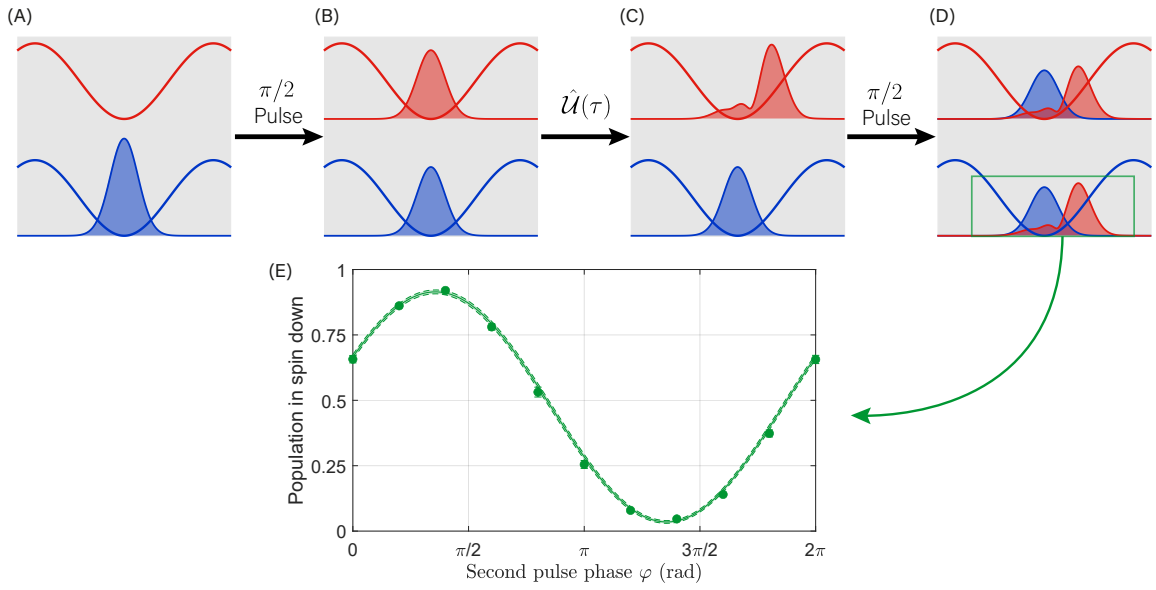


Figure 2.9: **Ramsey interferometry.** (A) The Ramsey interferometry sequence starts with all atoms in spin-down, typically prepared in an eigenstate of the trapping potential, Eq.(2.28). (B) A $\pi/2$ -pulse is applied at time $t = 0$, putting the atomic wave function in a balanced superposition between the two spin states, Eq.(2.29). (C) Each wave function evolves over a desired waiting time $t = \tau$ according to its corresponding potential, Eq.(2.30). The spin-down potential is typically kept static, meaning that the component of the wave function in spin down will also remain static (provided it was prepared in an eigenstate). (D) A second $\pi/2$ -pulse with a control phase φ_R with respect to the first one is applied at time $t = \tau$, Eq.(2.31). (E) All atoms in spin-up are removed and the remaining population fraction is measured. The remaining population fraction as a function of the control phase φ_R follows a sinusoidal fringe from which the overlap between the two spin components of the wave function is obtained, Eq.(2.32). The green circles correspond to the measured spin-down population while the green curve is the fit, with the dashed curves indicating the confidence interval.

The sequence starts by preparing the atom in an eigenstate of the spin-down potential, Fig. 2.9A

$$|\Psi(0)\rangle = \sqrt{p}|\downarrow\rangle \otimes |\psi(0)\rangle, \quad (2.28)$$

where $\psi(0)$ is an eigenstate of $U_{|3,3\rangle}(x)$ and $p \in [0, 1]$ is the overall efficiency of the state preparation. The value of p is mainly determined by the efficiency of the spin state preparation in $|4, 4\rangle$ (see Sec. 2.1.3)

and the efficiency of the microwave transfer from $|4, 4\rangle$ to $|3, 3\rangle$ (see Sec. 2.1.4). Subsequently, a Raman $\pi/2$ -pulse is applied at $t = 0$. The atom is therefore in a coherent balanced superposition of the two spin states, Fig. 2.9B

$$|\Psi_{\frac{\pi}{2}}(0)\rangle = \sqrt{p} \left[-i \sin\left(\frac{\theta}{2}\right) |\uparrow\rangle \otimes |\psi(0)\rangle + \cos\left(\frac{\theta}{2}\right) |\downarrow\rangle \otimes |\psi(0)\rangle \right]. \quad (2.29)$$

where $\theta = \pi/2 + \delta\theta$ is the Rabi angle induced by the pulse, with $\delta\theta$ being a possible deviation from a perfect $\pi/2$ rotation. The two components of the wave packet then evolve during a time τ in their corresponding potentials, Fig. 2.9C

$$|\Psi_{\frac{\pi}{2}}(\tau)\rangle = \sqrt{p} \left[-i \sin\left(\frac{\theta}{2}\right) |\uparrow\rangle \otimes |\psi_{\uparrow}(\tau)\rangle + \cos\left(\frac{\theta}{2}\right) |\downarrow\rangle \otimes |\psi_{\downarrow}(\tau)\rangle \right]. \quad (2.30)$$

where $\psi_{\uparrow}(\tau)$ and $\psi_{\downarrow}(\tau)$ denote the wave functions after an evolution time τ in the spin-up and spin-down potentials respectively. Subsequently, at time $t = \tau$, a second $\pi/2$ -pulse with a variable control phase φ_R relative to the first one, gives rise to an interference pattern, Fig. 2.9D

$$\begin{aligned} |\Psi_{\frac{\pi}{2}, \frac{\pi}{2}}(\tau)\rangle &= \frac{-i\sqrt{p}}{2} |\uparrow\rangle \otimes \left[\sin(\theta) |\psi_{\uparrow}(\tau)\rangle + \sin(\theta) e^{-i(\varphi_R + \delta_R \tau)} |\psi_{\downarrow}(\tau)\rangle \right] \\ &+ \frac{\sqrt{p}}{2} |\downarrow\rangle \otimes \left[(\cos(\theta) - 1) e^{i(\varphi_R + \delta_R \tau)} |\psi_{\uparrow}(\tau)\rangle + (\cos(\theta) + 1) |\psi_{\downarrow}(\tau)\rangle \right], \end{aligned} \quad (2.31)$$

where δ_R is the Raman detuning from the π -Qubit transition in the dark, i.e. when the Raman beams are off. We finally remove all atoms in spin-up and measure the remaining population in spin-down, which reads

$$p_{\downarrow} = \left| \langle \downarrow | \Psi_{\frac{\pi}{2}, \frac{\pi}{2}}(\tau) \rangle \right|^2 = \frac{p}{2} \left[2 - \sin^2(\theta) (1 + \mathcal{V}(\tau) \cos(\varphi_R + \delta_R \tau - \varphi(\tau))) \right]. \quad (2.32)$$

where $\mathcal{V}(\tau)$ and $\varphi(\tau)$ are the modulus and phase of the overlap $\langle \psi_{\uparrow}(\tau) | \psi_{\downarrow}(\tau) \rangle$ respectively. An example of such measurement is shown in Fig. 2.9E where it can be seen that the spin-down population follows a simple sinusoidal fringe. The fringe has visibility $\mathcal{V}(\tau)$ and phase offset $\varphi(\tau) - \delta_R \tau$.

The overlap $\langle \psi_{\uparrow}(\tau) | \psi_{\downarrow}(\tau) \rangle$ is obtained by fitting Eq.(2.32) to the measured fringe. However, still one more step has to be done. In order to obtain the phase $\varphi(\tau)$, the linear phase acquired due to the Raman detuning $\delta_R \tau$ has to be removed from the phase obtained from the fringe fit. The term $\delta_R \tau$ is not at all negligible because δ_R is equal to the lightshift produced by the Raman beams, which is on the order of a few MHz. This is due to the fact that δ_R corresponds to the detuning when the raman beams are off, but the frequency of the raman beams is chosen such that it is resonant to the π -Qubit transition when they are on, to obtain the highest transfer efficiency. The measurements presented in chapter 3 and chapter 4 require knowing $\varphi(\tau)$ with a precision of a fraction of a radian, over times of the order of 100 μ s, meaning that δ_R needs to be known with a precision well below 1 kHz. This is actually achieved using Ramsey interferometry itself. The sequence is exactly as described in this section with the two lattice components static and in the same position (i.e. the intensity maxima of the two lattice components coincide). Since the wave packet is prepared in an eigenstate, and the potentials of the two spin components are the same, then the spin-up and spin-down components of the wave packet will remain in the eigenstate and both will acquire the same phase. Any phase accumulated by the measured fringe will then come from the Raman lightshift. An example of the accumulated phases, measured for different evolution times from a fraction of a μ s up to around 50 μ s, is shown in Fig. 2.10.

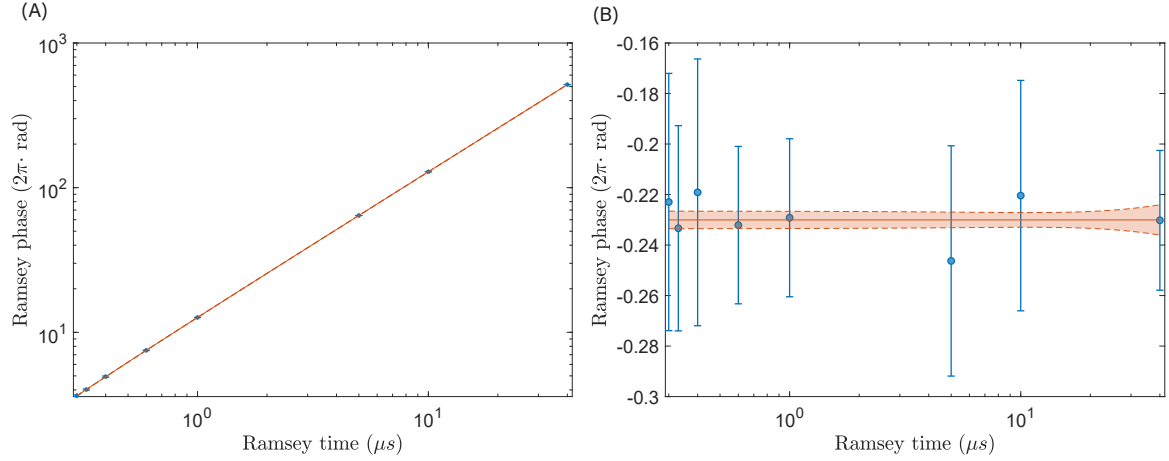


Figure 2.10: **Ramsey phase accumulation due to Raman lightshift.** Besides the dynamical phase $\varphi(\tau)$, the Ramsey fringes accumulate a phase $\delta_R \tau$ due to the Raman lightshift. **(A)** The blue points are the measured phases accumulated after different evolution times, exclusively due to the Raman lightshift, and the orange curve is a linear fit. **(B)** Same points and curve shown in A after subtracting the linear fit. The dashed curves and colored area represent the confidence interval of the linear fit.

2.2.5 Potential crosstalk compensation

In the measurements presented in Chapter 5, the $|4, 4\rangle$ spin state is used to study the dynamics of the trapped wave function in a position-modulated trapping potential. The $|4, 4\rangle$ state is ideal for that, since its potential doesn't depend on the relative position between the two σ -polarized lattices (see Eq.(2.10)). However, some of those measurements require a static wave function in $|3, 3\rangle$ that is used as a reference to be interfered with the evolving wave function in $|4, 4\rangle$. Such a reference wave function is prepared in the ground state of $|3, 3\rangle$ and, therefore, remains static as long as its potential remains static as well. However, from Eqs.(2.11, 2.15) we know that any modulation on the position or amplitude of the σ^+ -polarized lattice induces a modulation on the position and depth of the $U_{|3,3\rangle}$ potential. Figs. 2.11(A-C) illustrate an example where the position x_+ of the σ^+ -polarized lattice follows the trajectory shown in Fig. 2.11A with a constant amplitude. The induced modulation on the position and depth of the $U_{|3,3\rangle}$ potential is shown by the orange curves in Figs. 2.11(B,C).

The effect of the σ^+ -polarized lattice on $U_{|3,3\rangle}$ can be actively compensated with a modulation on the position and amplitude of the σ^- -polarized lattice. For all the measurements presented in this thesis the amplitudes of the σ^+ and σ^- lattice components are kept constant and equal between them. In that case, the position modulation induced by the σ^+ -polarized component on $U_{|3,3\rangle}$ can be suppressed by a modulation of the phase ϕ_- of the σ^- -polarized component²⁰

$$\phi_- = -\arcsin\left(\frac{\phi_+}{7f(\phi_+)}\right), \quad (2.33)$$

where the function $f(\phi_+)$ is a long analytical expression computed with Wolfram Mathematica [72]. An example of such compensation curve is shown as a dashed black line in Fig. 2.11B. The dashed curve is the required modulation of the σ^- -polarized component, according to Eq.(2.33), to suppress the orange curve that was induced by the modulation of the σ^+ -polarized component. Such compensation only suppresses the position modulation on $U_{|3,3\rangle}$, the induced depth modulation is still present. However, a

²⁰ We here remind the reader that the phase and the position of the lattice are related by Eq.(2.18).

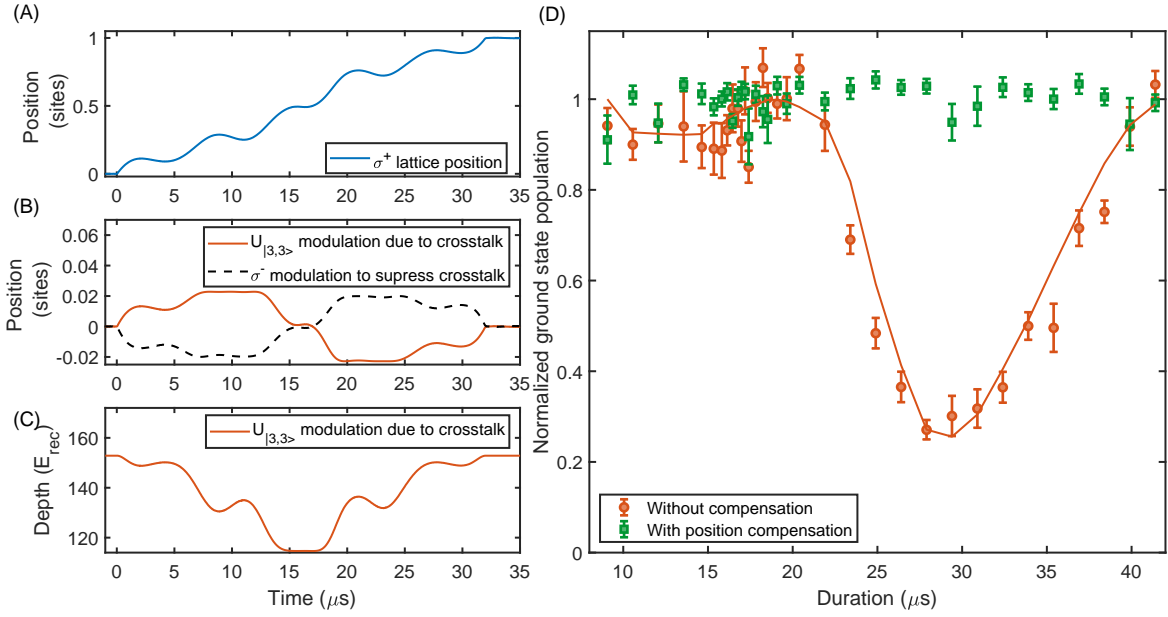


Figure 2.11: **Motional excitations due to lattice crosstalk.** Atoms initially prepared in the longitudinal ground state of $|3, 3\rangle$ may be heated up when the position or intensity of the σ^+ -polarized lattice component are modulated, see Eq.(2.11). (A) Example of a modulation on the σ^+ -polarized lattice position x_+ . (B) Position of the $U_{|3,3\rangle}$ potential (orange solid curve) induced by the modulation of the σ^+ -polarized component shown in A. And required modulation of the σ^- -polarized lattice component (dashed black curve) to suppress the induced modulation of the $U_{|3,3\rangle}$ potential. (C) Depth of the $U_{|3,3\rangle}$ potential induced by the modulation shown in A. In B and C, the position of the σ^- -polarized lattice x_- and the intensities of both lattice components I_{σ^\pm} are kept constant. (D) Measurement of the crosstalk effect on $|3, 3\rangle$. Atoms are prepared in the ground state of $|3, 3\rangle$. Subsequently, the position of the σ^+ -polarized lattice component is modulated with ramps similar to the one shown in A with different durations (horizontal axis of the plot). The ground state population after the modulation is measured (vertical axis) in the case when the crosstalk compensation Eq. (2.33) is done (green squares) and when it is not done (orange circles). The orange curve corresponds to the simulated ground state population.

compensation of the depth modulation is not required since most of the motional excitations are induced by the position modulation. This can be clearly seen in the results shown in Fig. 2.11D. Atoms were prepared in the ground state of $|3, 3\rangle$ and the σ^+ lattice component was modulated with sequences similar to the one shown in Fig. 2.11A but with different durations. Finally, the ground state population on $|3, 3\rangle$ was measured with the technique presented in Sec. 2.2.2. The measurement was done in two different situations: one in which the position compensation was done (green squares) and one in which no compensation was done (orange circles). It can be clearly seen that the position compensation is enough to suppress the motional excitations that are otherwise induced by the crosstalk.

Hello atom, how do you look like?

- Curious kid: "Hello atom, how do you look like?"
- ^{133}Cs atom: "I don't know, give me a mirror and I will tell you."
- Curious kid: "No problem, I got one here..."

3.1 Introduction

Imaging is a well known concept in the field of optics. From simple pinhole imaging up to time-resolved femtosecond holographic imaging in the sub-100 nm regime[73], a manifold of techniques have been developed to record the shape of an object in an image. Any imaging process requires some interaction with the imaged object and can, therefore, potentially disturb it. In the classical regime this generally does not pose a problem since the disturbances are typically negligible. Imaging a quantum object, on the other hand, is a different story. Extending the classical imaging to the quantum realm is a very challenging problem, since any interaction can produce substantial changes on the imaged object. Another difficulty comes from the fact that, unlike most classical objects, the exact state of a quantum object strongly depends on its environment. An atom trapped in our optical lattice potential looks different from the one freely flying inside the vacuum chamber. The answer to how does an atom look like thus depends on the external conditions, unlike a football that looks pretty much the same in my hands, on the table or on Ronaldo's foot.

The idea of observing a quantum object dates back to Werner Heisenberg who discussed the idea of using a microscope to observe an electron illuminated with light [38]. Since then, multiple techniques to image quantum objects have been developed and realized, including atomic density microscopy by nonlinear atomic response [41, 42], photoionization microscopy [74, 75], electron wave function measurement by angle-resolved photoemission [43], single photon holograms [44], atom-localization via position dependent Ramsey interferometry [76], recollision-based electron holography [77, 78], sequential measurement of complementary variables [45], among others. In this chapter I present a method to obtain a direct spatial image of a quantum wave packet $\psi(x, t)$ at any evolution time t with high accuracy, using Ramsey atom interferometry (see Sec. 2.2.4), and present the experimental results that correspond to the single-pixel version of the method. As we will see, even though the measurements correspond to single pixel images, they carry important information of the wave function as well as the trapping potential, allowing us to directly extract the eigenenergies of the Hamiltonian as well as the decomposition of the wave function in the eigenstate basis (Sec. 3.3). Additionally, from the behaviour of the images at short times, on the order of half an oscillation period, the first four Hamiltonian moments

are obtained (Sec. 3.4).

3.2 Single pixel image of a quantum wave packet

The imaging method presented in this chapter provides a direct time-resolved image of an evolving quantum wave function $\psi(x, t)$. The method consists of interferometrically comparing $\psi(x, t)$ to a static reference wave function $\Phi(x - x_p)$ parametrized by its position x_p . The interferometric signal provides the overlap between the two wave functions

$$O(x_p, t) = \int_{-\infty}^{\infty} dx \bar{\Phi}(x - x_p) \psi(x, t), \quad (3.1)$$

i.e., the convolution between $\psi(x, t)$ and $\bar{\Phi}(-x)$. The recorded overlap $O(x, t)$ represents the image of the evolving wave function $\psi(x, t)$. In fact, this imaging method is reminiscent of classical optical imaging. The spacial intensity distribution $I(x, t)$ (the image) measured by an optical imaging system at a given time t is given by the convolution between the intensity distribution of the object $I_o(x, t)$ and the point spread function of the imaging system $P(x)$ [79]

$$I(x_p, t) = (P * I_o)(x_p, t) = \int_{-\infty}^{\infty} dx P(x_p - x) I_o(x, t), \quad (3.2)$$

where x_p is the position of the pixel in the optical detector. Comparing Eq.(3.1) to Eq.(3.2), the analogy is clear, with $O(x, t)$ being the quantum analog of an optically recorded image $I(x, t)$ and $\bar{\Phi}(-x)$ being the quantum analog of the point spread function $P(x)$.

The measurements presented in this chapter were done with the reference wave function in one single position $x_p = 0$ and the recorded images $O(x_p = 0, t)$ are thus simply called $O(t)$ in the rest of the chapter. The recorded images are then identified as single-pixel images, following the analogy with an optical image recorded with a single pixel. The measurements make use of the hyperfine states $|F = 4, m_F = 3\rangle$ and $|F = 3, m_F = 3\rangle$, called spin-up and spin-down in this chapter, and are coupled with a pair of Raman beams (see Sec. 2.1.5). The imaging sequence starts by preparing the atom in a motional eigenstate of the spin-down potential¹. The spin-up potential (initially unpopulated) is displaced by a distance Δx as shown in Fig. 3.1A. At $t = 0$, a Raman $\pi/2$ pulse rotates the internal state into a coherent balanced superposition of the two spin states, effectively creating a copy of the spin-down wave function (blue) in the spin-up potential (red). Importantly, the component of the wave function in the spin-down potential is an eigenstate and remains stationary up to a phase, and its shape doesn't change. On the other hand, the component of the wave function in the spin-up potential is not an eigenstate, and thus it evolves in time, swinging back and forth in the trapping potential. After a desired evolution time t , the overlap between the two wave functions (Fig. 3.1B) is obtained by Ramsey interferometry as described in Sec. 2.2.4. The measurement is repeated for different evolution times to obtain time-lapse single-pixel images of the evolving wave packet. Notice that the wave functions prepared in the spin-up potential correspond to displaced number states, i.e. spatially displaced eigenstates $\psi_{n, \Delta x}(x) = \psi_n(x - \Delta x)$, where $\psi_n(x)$ is the n^{th} motional eigenstate. A similar measurement has been done in the past with cold ions in a harmonic potential [80].

In Fig. 3.2, some examples of the measured time-lapse single-pixel images $O(t)$ are shown. Fig. 3.2A illustrates the modulus $|O(t)|$ of the single-pixel images versus evolution time for wave packets initially

¹ To prepare the atoms in a specific eigenstate of $|F = 3, m_F = 3\rangle$, they are initially prepared in the ground state of $|F = 4, m_F = 4\rangle$ and transferred to $|F = 3, m_F = 3\rangle$ with a sideband resolved microwave pulse (see Sec. 2.1.4)

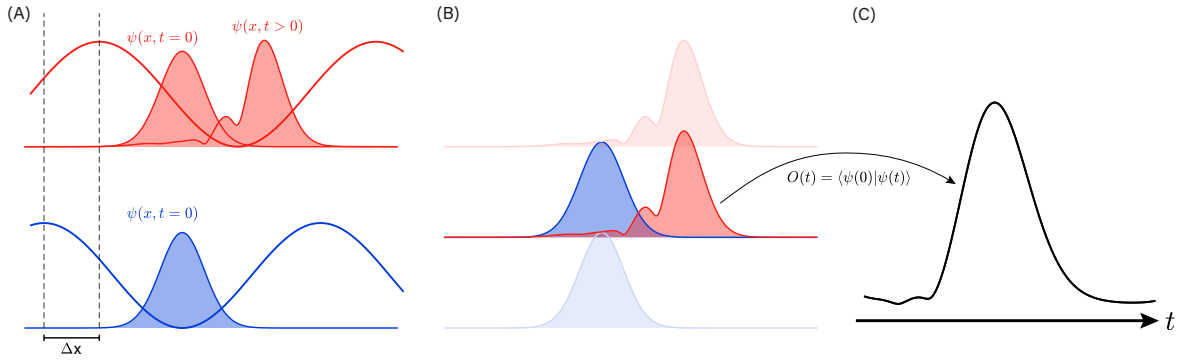


Figure 3.1: **Time-resolved single-pixel imaging.** The single-pixel image $O(t)$ of an evolving wave function at any time t is obtained by an interferometric comparison to a static reference wave function. (A) The atom is prepared in an eigenstate (blue) of the spin-down potential $\psi(x, t = 0)$. A Raman $\pi/2$ pulse creates a copy of it (red) in the spin-up potential, which is shifted by a distance Δx . The component in spin-up evolves over time while the component in spin-down doesn't, because it is an eigenstate. (B) After an evolution time t , the overlap between the two components is obtained by Ramsey interferometry, see Sec. 2.2.4. (C) The measured overlap $O(t)$ constitutes the time-resolved single-pixel quantum image of the wave function.

prepared in a displaced number state $n = 0$ with $\Delta x = 0.08\lambda/2$ (green), $n = 0$ with $\Delta x = 0.16\lambda/2$ (orange), $n = 1$ with $\Delta x = 0.16\lambda/2$ (blue) and $n = 2$ with $\Delta x = 0.2\lambda/2$ (black). Figs. 3.2(B-D) illustrate the phases $\varphi(t) = \arg(O(t))$ for $n = 0$ and $n = 1$. The solid black curves correspond to the theoretical expectation obtained from the simulation² of the wave packet dynamics and shows excellent agreement with the measurements. The evolution time is given in units of τ_{HO} , the oscillation period in the harmonic approximation³.

The imaged wave packets correspond to motional eigenstates initially displaced by a spatial distance from the bottom of the potential. As time evolves, the wave packet swings back and forth in the trapping potential. If the potential was harmonic, the wave packet evolution would be perfectly periodic. Since our trapping potential is sinusoidal instead, the anharmonicity breaks the periodicity of the evolution. For a small initial displacement, as in the case of the green traces in Fig. 3.2A that correspond to $n = 0$ with $\Delta x = 0.08\lambda/2$, the wave packet remains close to the bottom of the potential which is nearly harmonic. In that case, the wave packet evolution is almost periodic and both modulus and phase follow a nearly sinusoidal pattern, almost as in the case of a harmonic potential (see Sec. 3.5). Moreover, the oscillation period is very close to the harmonic period, only around 4% longer. For a larger displacement, as in the case of the orange traces that correspond to $n = 0$ with $\Delta x = 0.16\lambda/2$, the effects of the anharmonicity of the trapping potential are more evident. One of them is a more substantial elongation of the oscillation period to around 9% longer than the harmonic period. The other one is the reduction of the overlap maxima after every oscillation period. This happens because the components corresponding to different motional states do not perfectly rephase after every oscillation, as opposed to the harmonic case. The time-lapse images also allow us to resolve the double-peak and triple-peak structure of the wave functions corresponding to the first and second excited states respectively. This is illustrated in Fig. 3.3 for the case of the first excited state. The wave packet has two symmetric peaks and it swings back and forth in the trapping potential Fig. 3.3A. The shape of the wave packet deforms over time due to the anharmonic

² As mentioned in chapter 2, the simulation of the wave packet evolution is done using the Strang split-step integration method [69], and more details can be found in [63, 70]

³ In the harmonic approximation of the trapping potential (expansion up to the second order), the oscillation period is $\tau_{\text{HO}} = \sqrt{\lambda^2 m / (2U)}$ where λ is the lattice wavelength, m is the mass of the atom and U is the trap depth

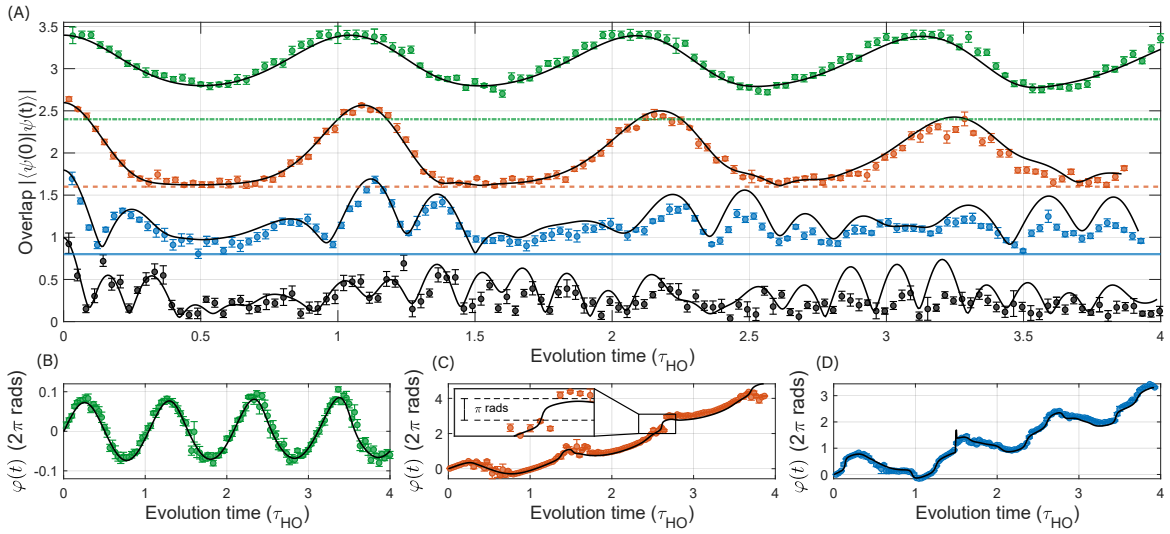


Figure 3.2: **Single-pixel time-lapse images of atomic wave packet evolution.** (A) Modulus of the single-pixel image versus evolution time $|O(t)|$ for wave packets prepared in $n = 0$ with $\Delta x = 0.08\lambda/2$ (green), $n = 0$ with $\Delta x = 0.16\lambda/2$ (orange), $n = 1$ with $\Delta x = 0.16\lambda/2$ (blue) and $n = 2$ with $\Delta x = 0.2\lambda/2$ (black). The evolution time is given in units of the oscillation period τ_{HO} in the harmonic approximation of the trapping potential. Each point is measured with the sequence illustrated in Fig.3.1. The measurements were done at a trap depth of around $27 \mu\text{K}$. For clarity, the different cases are vertically shifted, where the colored horizontal lines correspond to zero. (B), (C), (D) Phases $\varphi(t)$ of the single-pixel image for a wave packet initially prepared in $n = 0$ with $\Delta x = 0.08\lambda/2$ (green), $n = 0$ with $\Delta x = 0.16\lambda/2$ (orange) and $n = 1$ with $\Delta x = 0.16\lambda/2$ (blue) respectively (same cases shown in (A) except $n = 2$). The measurements are compared to the numerical simulation (solid black curves).

shape of the potential but the two peaks can still be clearly identified during the first oscillation, Fig. 3.3B. The different peaks observed in the recorded single-pixel image correspond to the moments when either one peak of the evolving wave packet coincides with one peak of the reference (numbered arrows 2 and 4) or when the two peaks coincide simultaneously (numbered arrows 1 and 5). The valley indicated by the arrow 3 correspond to the moment when the wave packet is at the farthest point from the initial position, i.e., after half an oscillation period.

3.3 Model-agnostic spectral decomposition

In Fig. 3.2 we have seen that the simulation of the system shows excellent agreement with the measurements. From the simulation we can certainly extract the eigenenergies and population probabilities of the wave packets, which characterize the wave packet evolution. But in this section we will see that a full simulation is not required to access that information. The energy spectrum of the trapping potential and the population probabilities of the wave function $\psi(x)$ in the basis of motional eigenstates are extracted with a simple method that doesn't rely on any predefined model. We only assume that the spectrum is discrete and that the population beyond a certain finite number of levels can be neglected.

As explained in Sec. 3.2, the atom is prepared in an eigenstate of the spin-down potential and a copy of it is produced in the spin-up potential. Therefore, at time $t = 0$ the wave function in spin-up $\psi_{\uparrow}(x, t = 0)$ and the wave function in spin-down $\psi_{\downarrow}(x, t = 0)$ coincide, and their expansion in the eigenstate basis of

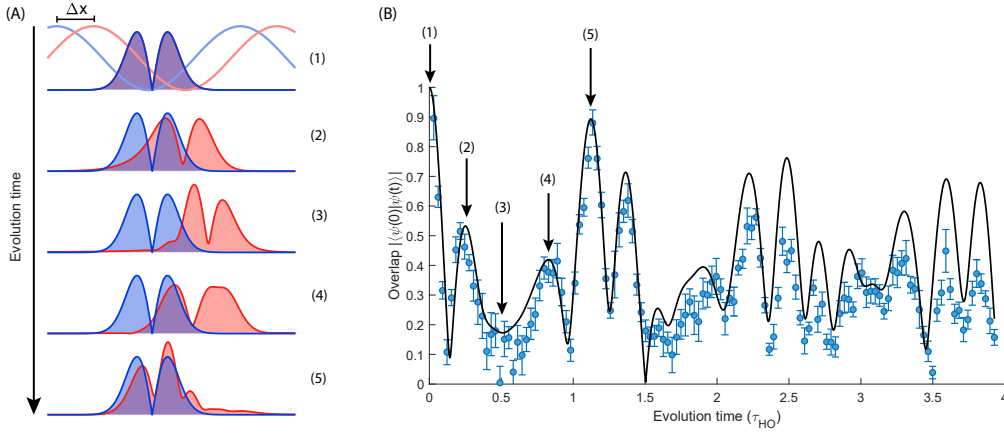


Figure 3.3: **Resolving double-peak structure of the first excited motional eigenstate.** (A) Evolution of a wave packet initially prepared in the spin-up potential in a displaced number state with $n = 1$ and $\Delta x = 0.16\lambda/2$ (red) that swings back and forth in the trapping potential. The wave packet in spin-down is in the eigenstate $n = 1$ ($\Delta x = 0$) and remains static (blue). The evolution is shown at 5 different times from $t = 0$ up to one oscillation period. The two lattice potentials are only shown for $t = 0$ for illustration purposes but they remain static at all evolution times. (B) Overlap between the two wave packets vs evolution time (also shown in Fig. 3.2A). The numbered arrows indicate the evolution times corresponding to the time shots shown in (A).

the spin-up potential reads

$$\psi_{\uparrow}(x, t = 0) = \psi_{\downarrow}(x, t = 0) = \sum_{n=0}^{\infty} c_n \psi_n(x), \quad (3.3)$$

where $\psi_n(x)$ is the n^{th} eigenstate of the spin-up potential and $c_n \in \mathbb{C}$. As time evolves, the spin-down wave function remains static and only acquires a global phase⁴

$$\psi_{\downarrow}(x, t) = e^{-i2\pi\nu_m t} \sum_{n=0}^{\infty} c_n \psi_n(x), \quad (3.4)$$

where m is the eigenstate number in which the wave function is initially prepared and $h\nu_m$ its energy with h being the Planck's constant. The spin-up is not in an eigenstate and each component thus evolves according to its corresponding eigenenergy

$$\begin{aligned} \psi_{\uparrow}(x, t) &= e^{-i\hat{H}t/\hbar} \sum_{n=0}^{\infty} c_n \psi_n(x) \\ &= \sum_{n=0}^{\infty} c_n e^{-i2\pi\nu_n t} \psi_n(x). \end{aligned} \quad (3.5)$$

The overlap between the spin-up, Eq.(3.4), and spin-down, Eq.(3.5), wave functions is then given by

$$O(t) = \sum_{n=0}^{\infty} p_n e^{-i2\pi(\nu_n - \nu_m)t} \quad (3.6)$$

⁴ $\psi_{\downarrow}(x, t)$ is written in terms of the eigenstates of the spin-up potential and this is why it is a sum of multiple terms. But it only acquires a global phase because it is actually trapped in the spin-down potential where it only occupies the m^{th} eigenstate.

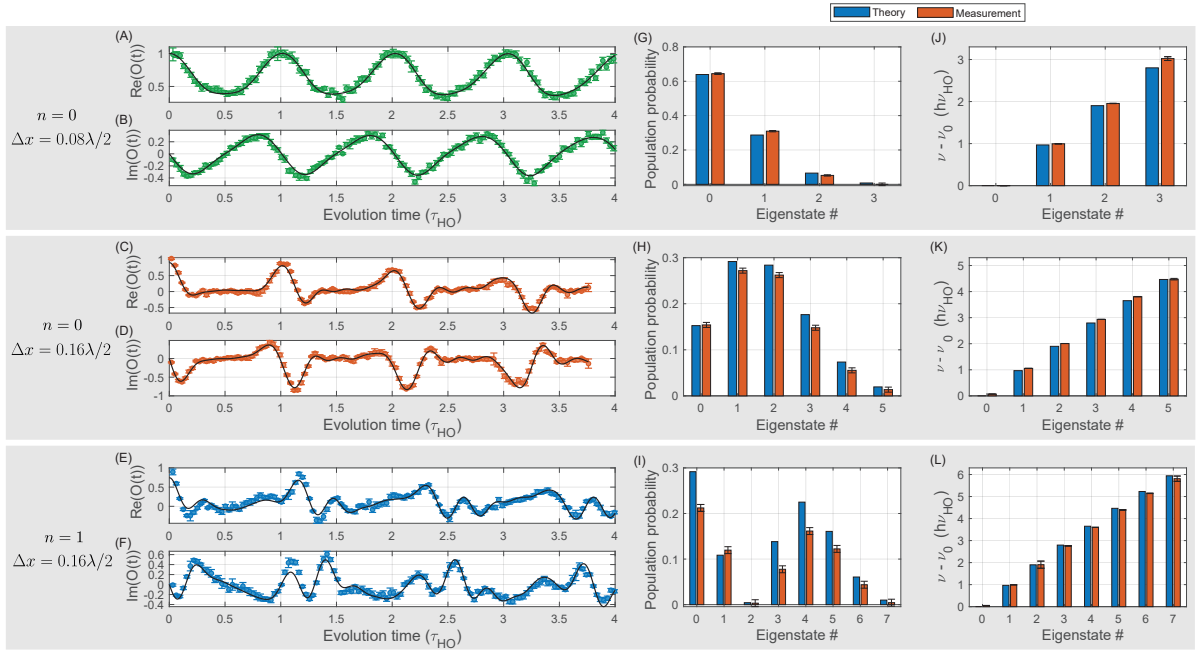


Figure 3.4: **Wave function spectral decomposition.** The recorded images shown in Fig. 3.2 are here shown in (A) to (F) split in their real and imaginary components. Simultaneous fits of the real and imaginary components were done using the complex-valued function (3.6) and shown as solid black curves. The population probabilities of the atomic wave packet and eigenenergies obtained from the fits are shown in (G-I) and (J-L) respectively (orange bars). The horizontal axis corresponds to the eigenstate number with zero being the ground state. The extracted values are compared to the theoretical values obtained from the simulation (blue bars). The energies are given in units of the Harmonic frequency $\nu_{\text{HO}} = 1/\tau_{\text{HO}}$ and with respect to the energy of the ground state ν_0 . The energies extracted from the fit in the case of the first excited state are given with respect to ν_1 . To give the values with respect to the ground state energy (as plotted in L) the value $\nu_0 - \nu_1$ obtained from the simulation is subtracted from them.

where $p_n = |c_n|^2$ is the population probability of the n^{th} eigenstate. Since the population probabilities are constant for time-independent Hamiltonians, the eigenenergies and population probabilities can be directly extracted by fitting the measured overlaps $O(t)$ with the expression in Eq.(3.6) with a finite number of terms. A simultaneous fit of the real and imaginary components has been applied to three of the measurements shown in Fig. 3.2. The measurements as well as the fits are shown in Fig. 3.4(A-F) split in their real and imaginary components. The number of eigenstates included in each fit is chosen up to the last component with a population probability above 1%; for the components with a small population probability the uncertainty of the fitted frequency diverges. The extracted population probabilities are shown in Fig. 3.4(G-I) and the eigenfrequencies in Fig. 3.4(J-L), all of them showing very good agreement with the theoretical values obtained from the simulation. It can be clearly seen that for a wave packet prepared in $n = 0$ with a small displacement of $\Delta x = 0.08\lambda/2$, most of the population is within the first four eigenstates, with the highest fraction still in the ground state. For a wave packet prepared in $n = 0$ with a larger displacement of $\Delta x = 0.16\lambda/2$, 6 eigenstates are populated, with the highest population fraction shifted up to the first and second excited states. In the two cases the population distribution has a shape similar to a Poisson distribution, which is the population distribution of a coherent state in a harmonic potential. In the case of a wave packet prepared in $n = 1$ with a displacement of $\Delta x = 0.16\lambda/2$, 8 eigenstates are populated and the population distribution clearly differs from the Poisson distribution.

The similarity to the population distribution of a coherent state in the case of the wave packets prepared in $n = 0$ is expected due to the nearly harmonic shape of the bottom of the lattice potential. This can also be seen in the energy spectrum; the first energy levels are very close to integer multiples of $h\nu_{\text{HO}}$ but the higher levels clearly deviate from the uniform energy spacing due to the anharmonic shape of the potential away from the bottom.

In the case of wave packets prepared in $n = 0$, an estimate of the width of the wave packet can be obtained from the extracted population. The ground state population is the square of the projection of the wave function into the ground state of the shifted potential, which under the harmonic approximation it is

$$p_0 = e^{-\frac{\Delta x^2}{2x_0^2}} \quad (3.7)$$

where x_0 is the width of the wave packet⁵. Using Eq.(3.7) to obtain x_0 from the extracted ground state populations shown in Figs. 3.4(G,H), a value of $x_0 = (37.8 \pm 0.3)$ nm is obtained from the measurement done at $\Delta x = 0.08\lambda/2$ and $x_0 = (38.3 \pm 0.3)$ nm from the one done at $\Delta x = 0.16\lambda/2$. Both values of x_0 correspond to around 8% of a lattice site and differ by less than 3% from the theoretical value.

3.4 Hamiltonian moments from recorded image traces

The eigenfrequencies ν_n of the Hamiltonian and the population probabilities p_n of the imaged wave function discussed in Sec. 3.3 completely characterize the evolution of the wave packet, Eq.(3.5). Alternatively, the wave packet evolution is also characterized by the Hamiltonian moments $\langle \hat{\mathcal{H}}^k \rangle = \langle \psi | \hat{\mathcal{H}}^k | \psi \rangle$, and the first two of them provide upper bounds to the rate of change of the evolving wave function, as we will see in chapter 4. The Hamiltonian moments can be computed from ν_n and p_n

$$\langle \hat{\mathcal{H}}^k \rangle = \sum_{n=0}^{\infty} p_n (h\nu_n)^k, \quad (3.8)$$

however, as we will see in this section, the Hamiltonian moments can also be directly extracted from the recorded images by a simple polynomial fit. Additionally, the method presented in this section has the advantage that it only requires the time-lapse single-pixel images at short evolution times (a fraction of an oscillation period) to extract the lowest order moments, as opposed to the method presented in Sec. 3.3 that requires a few oscillation periods. In this section, the first four moments are extracted from image traces recorded up to evolution times of only around half an oscillation period.

To obtain a relation between the Hamiltonian moments and the recorded images, let us expand the wave function $|\psi(t)\rangle$ over time

$$\begin{aligned} |\psi(t)\rangle &= \sum_{n=0}^{\infty} \frac{t^n}{n!} \left. \frac{d^n}{dt^n} |\psi(t)\rangle \right|_{t=0} \\ &= \sum_{n=0}^{\infty} \frac{(-it)^n}{n! \hbar^n} \hat{\mathcal{H}}^n |\psi(0)\rangle, \end{aligned} \quad (3.9)$$

where the Schrödinger equation $i\hbar d|\psi(t)\rangle/dt = \hat{\mathcal{H}}|\psi(t)\rangle$ has been used for the second equality, assuming that the Hamiltonian $\hat{\mathcal{H}}$ is time independent. The overlap $O(t)$ is then obtained by projecting into the

⁵ Here x_0 is the width of the normalized Gaussian wave function $\psi_0(x) = (x_0^2\pi)^{-1/4} e^{-x^2/(2x_0^2)}$

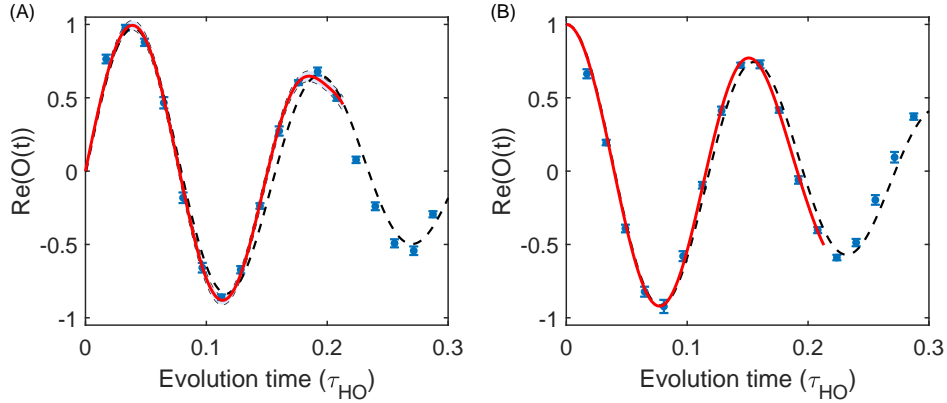


Figure 3.5: **Direct extraction of Hamiltonian moments** The Hamiltonian moments are obtained by fitting a polynomial to the recorded images at short times. The Hamiltonian moments are the coefficients of the fitted polynomials. The even order moments are obtained from the real component (A) and the odd order moments are obtained from the imaginary component (B). Here shown is an example corresponding to the wave packet prepared in $n = 0$ with $\Delta x = 0.45\lambda/2$. The measured values are shown as blue circles, the red solid curve is the fitted polynomial and the black dashed curve is the simulation.

state $\langle\psi(0)|$

$$\begin{aligned} O(t) &= \langle\psi(0)|\psi(t)\rangle \\ &= \sum_{k=0}^{\infty} \frac{(-it)^k}{k!\hbar^k} \langle\hat{H}^k\rangle. \end{aligned} \quad (3.10)$$

The Hamiltonian moments are thus the coefficients of the time expansion of $O(t)$. The first moments are directly obtained by fitting $O(t)$ with a polynomial fit. The real component contains the even order moments while the imaginary component contains the odd order moments. The real and imaginary components are independently fitted as in the example shown in Fig. 3.5 which corresponds to a lattice displacement of $\Delta x = 0.45\lambda/2$. The red curves are the polynomial fits and the dashed black curves are obtained from the simulation. The method doesn't rely on any predefined model and it works for any system that evolves under a time independent Hamiltonian.

A fit like the one shown in Fig. 3.5 has been done on 34 different time-lapse images corresponding to displaced number states with different displacements from $\Delta x = 0$ to $\Delta x = 0.5\lambda/2$ and motional states $n = 0$, $n = 1$ and $n = 2$. The extracted moments are shown in Fig. 3.6. The blue circles correspond to $n = 0$, the orange diamonds to $n = 1$ and the green triangles to $n = 2$. The values of the moments obtained with this method are given with respect to the eigenenergy of the reference wave function, i.e., a frame where the reference energy (zero energy) corresponds to the energy of the eigenstate in which the reference wave function is prepared. For comparison purposes, the values in Fig. 3.6 are all given with respect to the ground state's energy. The change of energy reference is explained in Appendix A. The experimental results are compared to the numerical calculation (solid lines). The excellent agreement between the theory and experiment confirms the validity of our extraction method.

Some features of the wave packets and the trapping potential are reflected in the mean energy (first moment). In Sec. 3.3 we have seen that the width of the ground state's wave packet is a few times smaller than a lattice site. Therefore, it is expected that as the wave packet is shifted, it will move up the potential hill, and its mean energy as a function of the shift Δx will have a shape similar to the potential.

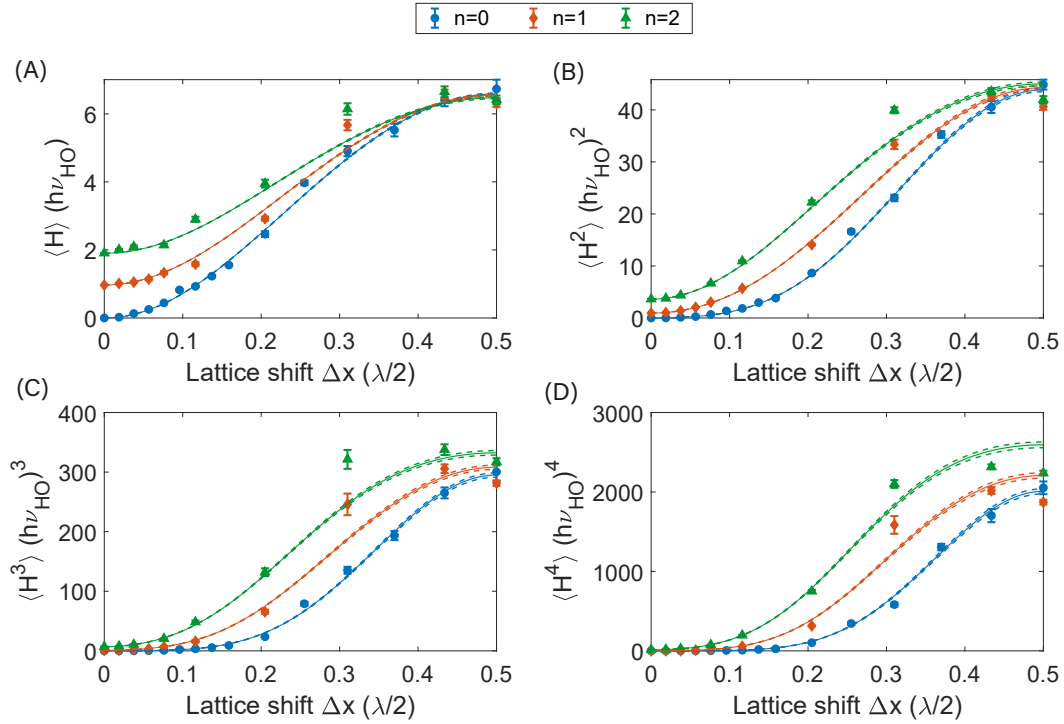


Figure 3.6: **HAMILTONIAN MOMENTS.** Extracted Hamiltonian moments $\langle \hat{H} \rangle$ (A), $\langle \hat{H}^2 \rangle$ (B), $\langle \hat{H}^3 \rangle$ (C) and $\langle \hat{H}^4 \rangle$ (D) obtained from the polynomial fit of the short time traces versus lattice displacement for $n = 0$ (blue circles), $n = 1$ (orange diamonds), and $n = 2$ (green triangles). The curves correspond to the theory obtained from the simulation.

In Fig. 3.6A it can be clearly seen that the mean energy indeed follows a shape similar to the sinusoidal shape of the lattice potential. Moreover, it can be seen that the mean energy in the case $n = 1$ (orange) also increases with Δx , but the energy increase is smaller. And in the case $n = 2$ (green), the energy increase is even smaller. This is due to the fact that, as n increases, the width of the wave packet also increases. Therefore, when the center of the wave packet is at the top of the potential, the probability distribution of a wave packet with $n = 0$ is concentrated at the top but the ones corresponding to higher excited levels ($n > 0$) extend further away from the top where the potential is lower. This is also why the mean energy of the excited levels is higher when $\Delta x = 0$, since a wave packet with $n = 0$ is concentrated at the bottom but the higher excited levels reach higher regions away from the bottom.

3.5 Phase of single-pixel images

In Fig. 3.2 we have seen that the phase $\varphi(t) = \arg(O(t))$ of the single-pixel images is nearly periodic when the displacement Δx is small, while for large displacements it accumulates an overall phase over time. Moreover, the accumulated phase may exhibit sharp jumps like the one observed in the case of a wave packet prepared in $n = 0$ with $\Delta x = 0.16\lambda/2$, inset in Fig. 3.2C. In this section I will discuss the origin of those features.

To get insight into what causes the phase accumulation, let us first look at the harmonic case. The phase of $O(t)$ in the case of a coherent state in a harmonic potential follows a sinusoidal curve $\varphi(t) = \Delta x^2 m \omega \sin(\omega t) / (2\hbar)$ and always comes back to zero after multiples of the oscillation period, irrespective of the displacement. Some examples of the phase versus time are shown in Fig. 3.7A for coherent states

corresponding to different displacements. And the trajectories of $O(t)$ in the complex plane for the same four cases are shown in Fig. 3.7B. The solid segments correspond to the first half of the oscillation period and the dashed segment to the second half. In the zoomed in region close to the origin, shown in Fig. 3.7C, it can be seen that the trajectories may get very close to the origin but they never encircle it. This is the reason why the phase goes back to zero once the trajectory closes. On the contrary, if a trajectory went around the origin, it would acquire an extra phase of 2π for every time it encircles the origin.

The reason why the closed trajectories of $O(t)$ corresponding to coherent states in a harmonic potential never encircle the origin, can be easily understood from a topological approach. Consider the case $\Delta x = 0$. In that case the wave function is in the ground state and remains static, which means $O(t) = \langle \psi(0) | \psi(t) \rangle = 1$ for all evolution times, i.e. the trajectory is just a point. As we continuously increase Δx , the trajectory $O(t)$ deforms continuously and acquires shapes similar to the ones shown in Fig. 3.7B. The trajectories may get close to the origin but never cross it because that would imply that for a certain value of Δx there is a time t for which $O(t) = \langle \psi(0) | \psi(t) \rangle = 0$, i.e. the wave function at time t would be orthogonal to the initial wave function. This is impossible for coherent states since the overlap between two coherent states can be arbitrarily small but never zero, irrespective of the displacement between them (see Appendix B). Therefore, irrespective of the value of the parameter Δx the closed trajectories never encircle the origin. In other words, in the case of coherent states in a harmonic potential, the single-pixel image traces are topologically protected against phase winding.

As opposed to the harmonic case, the phase of the single-pixel images of wave packets in the lattice potential may not come back to zero after every multiple of the oscillation period but rather wind up as time evolves. Fig. 3.7D shows the simulated phases for wave packets in the lattice potential, prepared in $n = 0$ with $\Delta x = 0.08\lambda/2$ and $\Delta x = 0.16\lambda/2$ (same curves shown in Fig. 3.2(B,C) next to the measurement). Their trajectories in the complex plane are shown in Fig. 3.7E. For illustration purposes, the first oscillation period is shown as a solid curve, the second as a dashed curve and the third one as a dotted curve. Clearly, for $\Delta x = 0.08\lambda/2$ the trajectory doesn't encircle the origin and the phase doesn't wind up. On the other hand, for $\Delta x = 0.16\lambda/2$ the trajectory in the complex plane encircles the origin three times (once in the second oscillation and twice in the third oscillation), and the phase indeed winds up by three times 2π . This means that the topological protection against phase winding is not present in the lattice potential.

By now we have seen that in the lattice potential, after the first few oscillation periods $O(t)$ encircles the origin when Δx is large and it doesn't encircle the origin when Δx is small. But a natural question arises at this point: in the case of a small Δx , will the trajectory eventually go around the origin if we wait long enough? And the answer is: no, if more than 50% of the population is in one single eigenstate. To see why this is the case, consider Eq.(3.6) in the case that the wave packet has more than 50% of the population in one eigenstate, i.e. $p_k > 0.5$ for some $k \in \mathbb{N}$. Then⁶

$$\begin{aligned}
 O(t) &= \sum_{n=0}^{\infty} p_n e^{-i2\pi(v_n - v_k)t} \\
 &= p_k + \sum_{n \neq k} p_n e^{-i2\pi(v_n - v_k)t} \\
 &= p_k + r
 \end{aligned} \tag{3.11}$$

⁶ Without loss of generality, we moved to the reference frame rotating at a constant angular frequency equal to $2\pi|v_m - v_k|$ where m corresponds to the eigenstate in which the reference wave function is prepared. Since the rotation is done around the origin, the change of frame has no influence on the distance between the origin and the trajectory

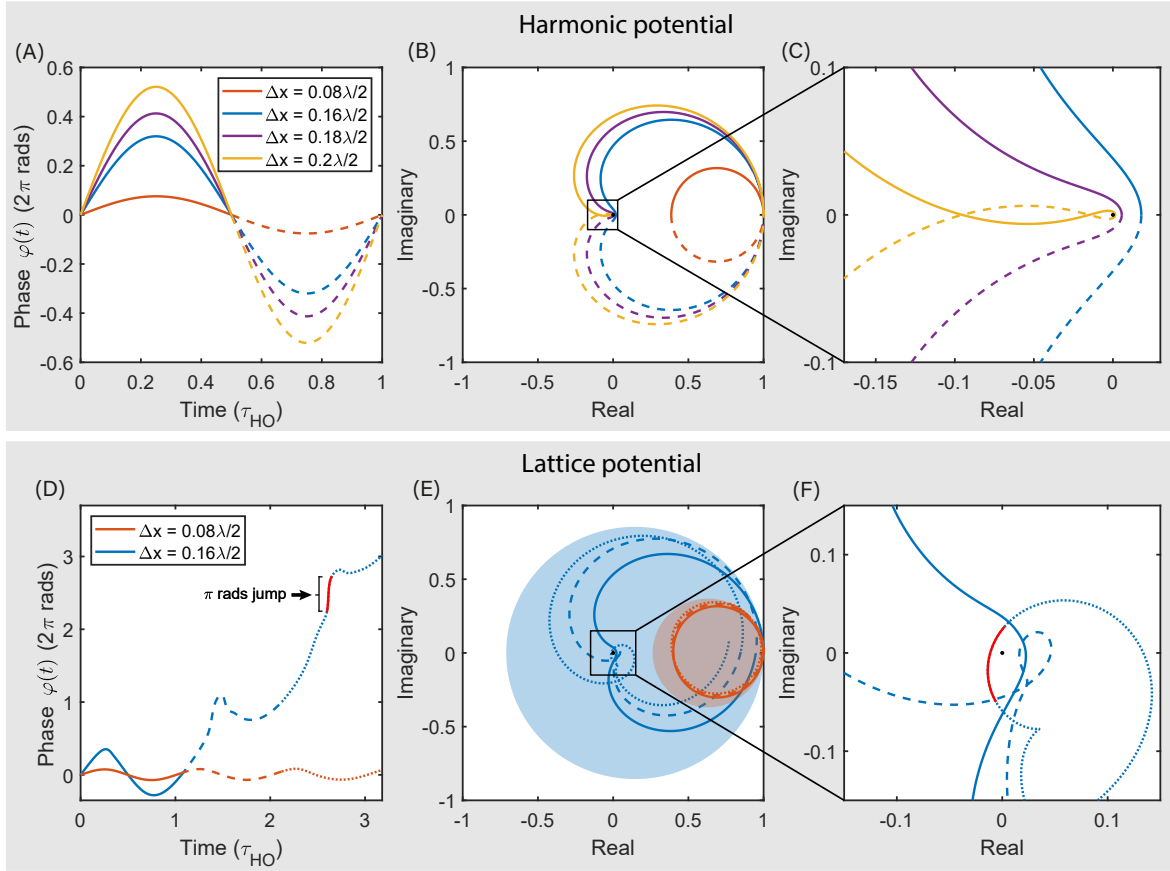


Figure 3.7: **Phase accumulation of single-pixel image traces.** (A) Phase $\varphi(t)$ of the single-pixel image traces $O(t)$ of coherent wave packets in a harmonic potential for different displacements Δx (obtained from simulation). (B) Trajectories followed by $O(t)$ in the complex plane for the same cases shown in A. The solid curves correspond to the first half of the oscillation period and the dashed curves to the second half. (C) Zoom in on the region close to the origin of the plot in B. The trajectories get arbitrarily close to the origin but never go around it. (D) Phase $\varphi(t)$ of the single-pixel image traces in the lattice potential for $n = 0$ with $\Delta x = 0.08\lambda/2$ (orange) and $\Delta x = 0.16\lambda/2$ (blue) over approximately three oscillation periods (obtained from simulation). (E) Trajectories followed by $O(t)$ in the complex plane for the same cases shown in D. The colored background circles illustrate the area that must contain the trajectories of $O(t)$ according to Eq.(3.11). The solid segments of the curves correspond to the first oscillation period, the dashed segments correspond to the second period, and the dotted segments to the third period. (F) Zoom in on the region close to the origin of the plot in E. From E and F it is clear that for $\Delta x = 0.08\lambda/2$, the trajectory never encircles the origin. For $\Delta x = 0.16\lambda/2$, in the first period the trajectory doesn't encircle the origin, in the second period it encircles it once and in the third period it encircles it twice. The accumulated phase shown in D winds up by a factor of 2π radians for every time that $O(t)$ encircles the origin in the complex plane. And a sharp jump of π radians is observed when the trajectory of $O(t)$ in the complex plane passes close to the origin (red segment in D and F).

where r is a complex number with modulus $|r| \leq 1 - p_k < 0.5$ (from triangle inequality). Therefore, the trajectory has to be inside the circle with center at $p_k > 0.5$ and radius $|r| < 0.5$, which doesn't contain the origin. Two examples of the circles defined by Eq.(3.11) are represented by the colored background in Fig. 3.7E for wave packets in the lattice potential with $\Delta x = 0.08\lambda/2$ (orange) and $\Delta x = 0.16\lambda/2$ (blue). In the case $\Delta x = 0.08\lambda/2$, the ground state population is above 50%, therefore, the trajectory cannot reach the origin and thus cannot encircle it. On the other hand, for $\Delta x = 0.16\lambda/2$ the maximum

population is below 50% and can (but doesn't have to) encircle the origin. Note that this also means that $p_k > 0.5$ is a sufficient (but not necessary) condition to have no phase winding. In fact, since the trajectory has to be inside the circle defined by Eq.(3.11), the phase is bounded by

$$|\varphi(t)| \leq \arcsin\left(\frac{1-p_k}{p_k}\right) \text{ when } 0.5 \leq p_k \leq 1, \quad (3.12)$$

at all evolution times (Appendix C). Moreover, note that Eq.(3.12) is valid for any trapping potential, since Eq.(3.11) is independent of the potential.

Another feature that can be easily understood from the trajectories in the complex plane is the possible discontinuities in $\varphi(t)$. If the trajectory of $O(t)$ in the complex plane crosses the origin, the phase suffers a discontinuous jump of π radians. If the trajectory passes close to the origin, the phase is not mathematically discontinuous but still has a very abrupt increase or decrease of π radians. This is observed in the case corresponding to $n = 0$ with $\Delta x = 0.16\lambda/2$ at $t \approx 2.6\tau_{\text{HO}}$ highlighted as a red segment in its phase, Fig. 3.7D, and its trajectory in the complex plane, Fig. 3.7F. This can also be observed in the measurement corresponding to the same parameters (see inset in Fig. 3.2C).

3.6 Outlook

In this chapter we have seen that a lot of information can be extracted from the images recorded with the reference wave function restricted to a single position, i.e. Eq.(3.1) restricted to one fixed value of x_p . An N -pixel version of the measurement can be done by repeating the single-pixel measurement N times, with the reference wave function placed at N different positions x_i with $i \in [1 : N]$ and $x_{i+1} - x_i = \delta x$ for some chosen spacing δx . In that case, the wave function $\psi(x, t)$ can be reconstructed at the N discrete positions $\psi_i(t) := \psi(x_i, t)$ at any desired evolution time t . Let the reference wave function be $\Phi(x)$ and let $\Phi_{j,i} := \Phi(x_i - x_j)$. The measured overlap is then given by the discrete version of Eq.(3.1)

$$\begin{aligned} O_j(t) &= \int_{-\infty}^{\infty} dx \bar{\Phi}(x - x_j) \psi(x, t) \\ &\approx \sum_{i=1}^N \bar{\Phi}(x_i - x_j) \psi(x_i, t) \delta x^2 \\ &= \sum_{i=1}^N \bar{\Phi}_{j,i} \psi_i(t) \delta x^2 \end{aligned} \quad (3.13)$$

which we can write as

$$\vec{O}(t) = \bar{P} \vec{\psi}(t) \quad (3.14)$$

where $\vec{O}(t) = (O_1(t), \dots, O_N(t))$ is the vector of measured overlaps, $\vec{\psi}(t) = (\psi_1(t), \dots, \psi_N(t))$ is the imaged wave function vector and P is the matrix with elements $\delta x^2 \Phi_{j,i}$. If the matrix P is invertible, then the imaged wave function is computed from the measured overlaps as

$$\vec{\psi}(t) = \bar{P}^{-1} \vec{O}(t). \quad (3.15)$$

This way, the whole dynamical evolution can be imaged with the proposed method.

In Sec. 3.5 we have seen that the trajectories of the single-pixel image traces in the complex plane in the case of coherent states in a harmonic potential never wind up around the origin. In fact, we have seen that the trajectories are topologically protected against winding. On the other hand, in the case of wave

packets in the lattice potential the trajectories may wind up after a few oscillation periods. Some natural questions arise from this observation: Is the topological protection against winding also present in some anharmonic potentials or only in the harmonic potential? When there is non-zero winding, is it possible to define a winding number associated to each trajectory? For which type of trapping potentials can a winding number be defined? Can we observe topological phase transition between winding numbers with the method presented in this chapter? A clear difficulty in defining a winding number is the fact that the trajectories have to be closed, otherwise the winding number is not well defined. But these are all interesting questions that we are planning to investigate in the future.

How fast am I allowed to drive Mr. Heisenberg?

- ^{133}Cs atom: “Mr. Heisenberg, How fast can I drive?”
- Werner Heisenberg: “That depends on how well you know yourself my friend.”

4.1 Introduction

We all remember the famous Heisenberg uncertainty principle from our first course on quantum mechanics. Specially its two most common versions: the position-momentum uncertainty relation $\Delta p \Delta x \geq \hbar/2$ and the energy-time uncertainty relation $\Delta E \Delta t \geq \hbar/2$. Werner Heisenberg came out with these results in 1927 [38] from his analysis on the observation of an electron with light. A more general result was derived by Robertson in 1929 [81], for any pair of observables $\Delta O_1 \Delta O_2 \geq |\langle [O_1, O_2] \rangle|/2$ where $\Delta O^2 = \langle \psi | O^2 | \psi \rangle - \langle \psi | O | \psi \rangle^2$ is the standard deviation of the observable O associated to the quantum state ψ . Heisenberg’s position-momentum relation is clearly a case of Robertson’s result, since p and x are both observables, and the relation is valid for any quantum state. On the other hand, the energy-time relation cannot be directly generalized to any quantum state using Robertson’s result because time is not an observable. In fact, even nowadays the energy-time uncertainty relation sometimes creates confusion because time and energy are wrongly regarded as a pair of canonical variables [82, 83] giving rise to situations where Δt doesn’t have a concrete meaning.

An alternative to Heisenberg’s energy-time uncertainty relation, valid for any quantum system, was proposed by two Soviet physicists, Leonid Mandelstam and Igor Tamm (here called MT bound) [27]

$$|\langle \psi(0) | \psi(t) \rangle| \geq \cos\left(\frac{\Delta E t}{\hbar}\right) \quad \text{for } t \in [0, \tau_{\text{MT}}], \quad (4.1)$$

where $\psi(t)$ is the wave function at time t evolving under a Hamiltonian¹ \mathcal{H} , and $\tau_{\text{MT}} := \pi\hbar/(2\Delta E)$ is the minimum time to reach an orthogonal state according to the MT bound. The inequality has a clear interpretation: given an evolution time t , it sets a bound to the minimum overlap between the initial and the evolved wave functions. Later, Norman Margolus and Lev B. Levitin proposed a similar inequality (here called ML bound) with the same interpretation [28]

$$|\langle \psi(0) | \psi(t) \rangle| \geq \cos\left(\sqrt{\frac{\pi E t}{2\hbar}}\right) \quad \text{for } t \in [0, \tau_{\text{ML}}], \quad (4.2)$$

¹ The energy spread is the standard deviation of the Hamiltonian $\Delta E^2 = \langle \psi | \mathcal{H}^2 | \psi \rangle - \langle \psi | \mathcal{H} | \psi \rangle^2$.

where $E = \langle \mathcal{H} \rangle$ is the mean energy measured with respect to the ground state's energy, and $\tau_{\text{ML}} := \pi\hbar/(2E)$ is the minimum time to reach an orthogonal state according to the ML bound.

Experimental demonstrations of the MT and ML bounds have been done in the past for systems that can be effectively reduced to a two-level system [40, 84, 85]. In this chapter, our results on the experimental verification of the bounds in a multi-level system are presented. To our knowledge, this is the first demonstration of the bounds beyond effective two-level systems. This way we have given more value to the bounds by extending their validation towards more complex systems. This is relevant for quantum technologies, that rely on systems that typically make use of a higher number of states than a simple two level system. The platform used to realize the measurements consists of a single atom trapped in a static optical lattice potential, with the atom initially prepared in a displaced number state i.e. an eigenstate spatially displaced by some desired distance (between zero and one lattice site). Verifying the MT and ML bounds requires measuring the overlap $O(t) = \langle \psi(0) | \psi(t) \rangle$, as well as the energy spread and mean energy of the wave function. The overlap $O(t)$ corresponds to the interferometric single-pixel image of the evolving wave packet discussed in Chapter 3, while the energy spread and the mean energy are extracted from the behaviour of $O(t)$ in the limit of small times, with a method similar to the one used to obtain the Hamiltonian moments² in Chapter 3. As expected, we have found that the evolving wave packets satisfy the unified bound. Moreover, a crossover from a region where the MT bound is more restrictive to a region where the ML bound is more restrictive is observed, Fig. 4.1. The crossover is only observed when the wave packet has an energy spread higher than its mean energy, $\Delta E > E$. In that case, the wave packet evolution is limited by the MT bound at evolution times below the crossover time $\tau_c := \tau_{\text{MT}}^2/\tau_{\text{ML}}$, while at longer times it is limited by the ML bound, Fig. 4.1A. If $E > \Delta E$, on the other hand, the wave packet evolution is limited by the MT bound at all evolution times within the region of applicability, i.e. up to the orthogonalization time τ_{MT} , Fig. 4.1B.

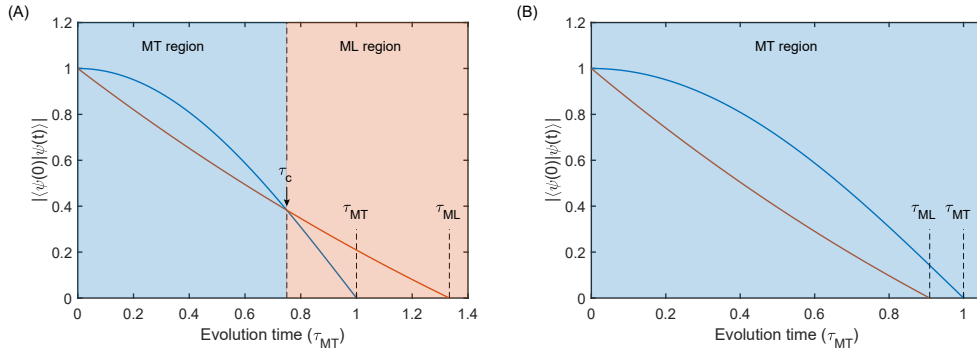


Figure 4.1: **Crossover between Mandelstam-Tamm and Margolus-Levitin bounds.** Illustration of the bound imposed by the MT and ML bounds. The blue and orange curves represent the minimum overlap allowed by the MT and ML bounds respectively. The blue and orange backgrounds distinguish the time region where either the MT or the ML bound is more restrictive respectively. (A) If $\Delta E > E$, the MT bound is more restrictive up to the crossover time τ_c while the ML bound is more restrictive at times beyond the crossover. (B) If $E > \Delta E$, the MT bound is more restrictive at all times.

The MT bound can be alternatively written in terms of the Fubini-Study metric [86, 87], $\mathcal{D}[\psi(0), \psi(t)] := \arccos |\langle \psi(0) | \psi(t) \rangle|$ as

$$\mathcal{D}[\psi(0), \psi(t)] \leq \frac{\Delta E t}{\hbar} \quad \text{for } t \in [0, \tau_{\text{MT}}]. \quad (4.3)$$

² Even though the energy spread can be computed from the first two energy moments measured in Sec. 3.4, we here use a method that extracts the energy spread from $O(t)$ in a direct way, providing a more accurate value.

And equivalently, the ML bound can be written as

$$\mathcal{D}[\psi(0), \psi(t)] \leq \sqrt{\frac{\pi E t}{2\hbar}} \quad \text{for } t \in [0, \tau_{\text{ML}}]. \quad (4.4)$$

The Fubini-Study metric provides a measure of the distance between the two states $\psi(0)$ and $\psi(t)$. This way, the inequalities impose a limit on the maximum distance between the initial and final states (Fig. 4.2A), in other words they impose a maximum speed limit of quantum evolution. Interestingly, it has been proved that the actual path length covered by a quantum state over an evolution time t is always $\ell(t) = \Delta E t / \hbar$ [30], which happens to be equal to the maximum distance between $\psi(0)$ and $\psi(t)$ according to the MT bound Eq.(4.3). This could lead to the wrong conclusion that the MT bound is always saturated. To clarify this, it is important to distinguish between the total path length and the distance between the initial and final states, as illustrated in Fig. 4.2B. Both ψ_1 and ψ_2 follow trajectories with a path length equal to $\ell(t)$, but ψ_1 reaches a longer distance between initial and final states. With this at hand, the MT bound can be written in geometric terms as $\mathcal{D}[\psi(0), \psi(t)] \leq \ell(t)$, i.e. the maximum distance between the initial and final states cannot be larger than the path length $\ell(t)$. This brings us to another important question covered in this chapter: how close is the evolution of the system to the fundamental speed limit. Or in other words, how close is $\mathcal{D}[\psi(0), \psi(t)]$ form $\ell(t)$? This question is important if you want to improve the performance of a quantum system by speeding up the required operations, since it will tell you how much room for improvement is potentially available. In this chapter, the deviation from the MT bound is quantified for wave packets prepared in 34 different initial states. We have found that as ΔE increases, the deviation decreases and converges to a small value, meaning that the wave packet evolves at a rate close to the limit imposed by the MT bound even though multiple levels are populated. This is in contrast with the intuitive but wrong idea that the MT bound is only meaningful for effective two-level systems and quickly deviates from the actual evolution rate (providing absurdly small values) as soon as many levels are populated. Such wrong idea arises from the fact that the MT and ML bounds have been proved to be saturated only by effective two-level systems [39]. A strong deviation from the bounds is observed in some systems as we will see in chapter 5, but the results in this chapter show that this is not always the case.

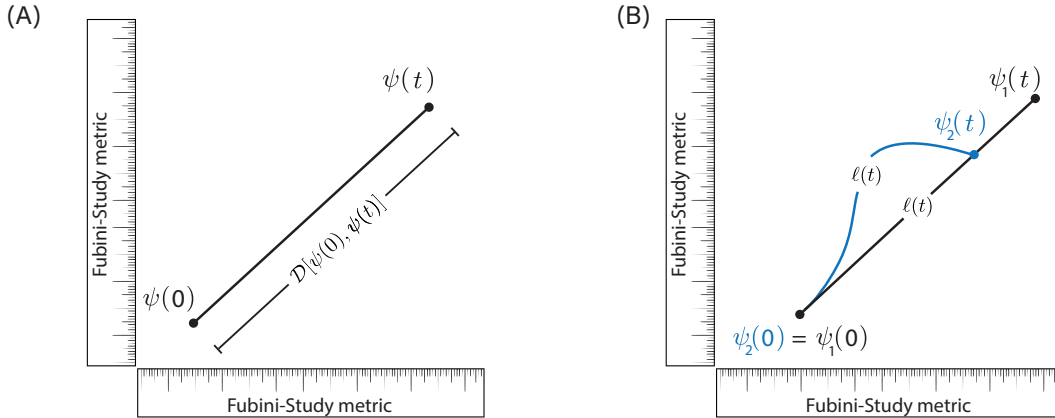


Figure 4.2: **Fubini-Study metric.** (A) The Fubini-Study metric provides a measure of the distance between two quantum states. (B) The quantum state ψ_1 evolves along the black curve while ψ_2 evolves along the blue curve. The path length is $\ell(t)$ in both cases but the distance between initial and final states is shorter for ψ_2 .

Observing quantum-speed-limit crossover with matter wave interferometry

Gal Ness,¹ Manolo R. Lam,² Wolfgang Alt,² Dieter Meschede,² Yoav Sagi,¹ and Andrea Alberti^{2,*}

¹*Physics Department, Technion – Israel Institute of Technology, IL-32000 Haifa, Israel*

²*Institut für Angewandte Physik, Universität Bonn, D-53115 Bonn, Germany*

(Dated: April 13, 2021)

Quantum mechanics sets fundamental limits on how fast quantum states can be transformed in time. Two well-known quantum speed limits are the Mandelstam–Tamm (MT)¹ and the Margolus–Levitin (ML)² bounds, which relate the maximum speed of evolution to the system’s energy uncertainty and mean energy, respectively. Here, we test concurrently both limits in a multi-level system by following the motion of a single atom in an optical trap using fast matter wave interferometry. Our data reveal two different regimes: one where the MT limit constrains the evolution at all times, and a second where a crossover to the ML limit is manifested at longer times. We take a geometric approach to quantify the deviation from the speed limit, measuring how much the matter wave’s quantum evolution deviates from the geodesic path in the Hilbert space of the multi-level system. Our results, establishing quantum speed limits beyond the simple two-level system, are important to understand the ultimate performance of quantum computing devices and related advanced quantum technologies^{2,3}.

Introduction.—The celebrated energy-time uncertainty relation was given a rigorous interpretation by Mandelstam and Tamm (MT) as a lower bound on the time it takes a quantum system to evolve into a different state¹. A second independent bound was formulated by Margolus and Levitin (ML) in terms of the mean energy relative to the ground state². The maximum of these two times provides a unified bound for the quantum speed limit^{4–6}.

In the simplest scenario of a two-level system (qubit), both limits yield the same minimum time to reach an orthogonal state, which is the Rabi flopping time. The same holds for systems that can be effectively mapped onto two-level Hamiltonians, as was demonstrated by previous experimental investigations^{7–9}. However, devices for quantum simulation and information processing rely on a far greater number of states, and often include a nonvanishing coupling to the continuum. It is therefore essential to test quantum speed limits beyond the restricted Hilbert space of a qubit.

In this work, we study quantum speed limits in a clean manifestation of a multi-level system—a single atom in a potential well of finite depth. The potential supports many bound states, yet at the same time it possesses a continuum of free-particle states, which allow the atom to leave the trap. Using a fast excitation-interrogation scheme, we investigate the ideal case of a time-independent Hamiltonian \hat{H} , where the quantum dynamics originates from an initial motional excitation of the atom—a matter wave. In the limit of small excitations, we recover the qubit case, where the quantum evolution involves mainly two states. However, by increasing the excitation extent, we depart from this limit in a well-controlled manner to probe the multi-level contribution, up to the point that the atom populates mostly

unbound states in the continuum. Our measurements reveal that both speed limits provide relevant bounds on the system’s quantum dynamics. This result is in stark contrast to the case of a driven multi-level system, where the MT bound yields an excessively short time scale¹⁰.

The MT bound constrains^{11–13} the two-time state overlap $|\langle\psi(0)|\psi(t)\rangle|$ from below by means of the energy uncertainty ΔE ,

$$|\langle\psi(0)|\psi(t)\rangle| \geq \cos\left(\frac{\Delta E t}{\hbar}\right), \quad (1a)$$

in the domain $0 \leq t \leq \tau_{\text{MT}} \equiv \pi\hbar/(2\Delta E)$. Here, τ_{MT} is the MT orthogonalization time, i.e., the minimum duration for the evolved state to become orthogonal to the initial one. The energy uncertainty follows¹⁴ the conventional definition $\Delta E^2 = \langle\hat{H}^2\rangle - \langle\hat{H}\rangle^2$.

The ML bound, on the other hand, constrains⁴ the two-time state overlap from below by the mean energy $E = \langle\hat{H}\rangle$,

$$|\langle\psi(0)|\psi(t)\rangle| \geq \cos\left(\sqrt{\frac{\pi E t}{2\hbar}}\right), \quad (1b)$$

in the domain $0 \leq t \leq \tau_{\text{ML}} \equiv \pi\hbar/(2E)$, with the ground state energy chosen to be zero. Similarly, τ_{ML} represents the minimum orthogonalization time according to the Margolus-Levitin bound.

The left-hand side of Eqs. (1a) and (1b) can be understood as a measure of the change of the time-evolved quantum state with respect to the original one. In fact, the two-time state overlap relates directly to the distance covered by the quantum state as measured by the Fubini-Study (FS) metric in the projective Hilbert space¹⁵, $\mathcal{D}[\psi(0), \psi(t)] \equiv \arccos|\langle\psi(0)|\psi(t)\rangle|$. This definition of distance allows interpreting the two inequalities as bounds on the quantum state’s rate of change, i.e., as quantum speed limits.

* alberti@iap.uni-bonn.de

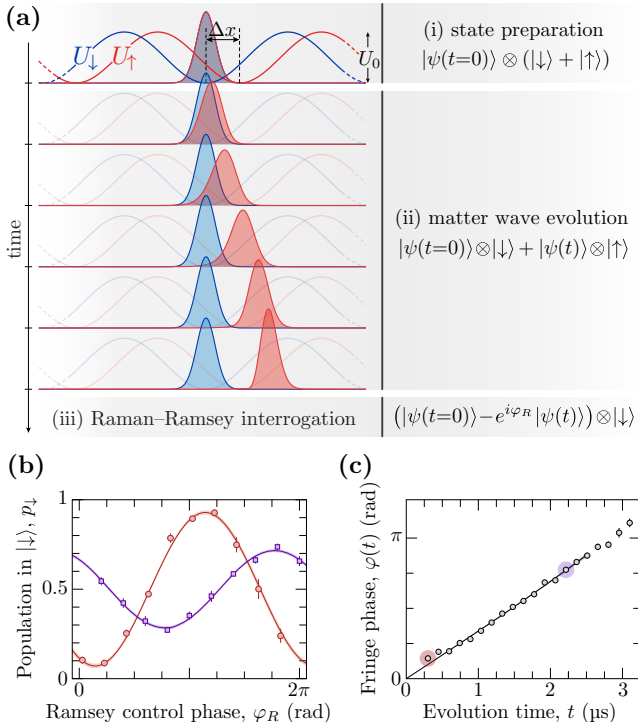


Figure 1. Fast matter wave interferometry for testing quantum speed limits (a) Illustration of the Raman-Ramsey measurement technique: (i) At $t=0$, the atom is placed in a superposition of $|\uparrow\rangle$ and $|\downarrow\rangle$ states, each subject to a different periodic potential, U_\uparrow and U_\downarrow . (ii) The atom with $|\uparrow\rangle$, initially displaced by Δx from the trap center, slides downhill and concurrently deforms by the anharmonicity of its potential. The atom with $|\downarrow\rangle$ is in a vibrational eigenstate ($n=0$ in this example), which remains unchanged. (iii) The probability of occupying $|\downarrow\rangle$ is measured as a function of the control Ramsey phase φ_R . The quantum states are displayed on the right-hand side up to a normalization factor. (b) Ramsey fringes measured as a function of φ_R for two selected evolution times, 300 ns and 2.2 μ s, with $\Delta x = 0.2 \lambda/2$. Solid lines are cosine functions fitted to the data, with shades denoting the 1- σ confidence regions. Data points are normalized to account for atom losses (5%), and error bars mark the standard error. (c) Fringe phase tracked as a function of time. Circled points correspond to the fringes displayed in (b). Solid line is a fifth-order polynomial fit containing only odd-power terms¹⁶, used to extract E based on Eq. (2).

Fast matter wave interferometry.—The basic idea of our experiment is as follows. We start with an atom in the vibrational level n of an optical trap (Appendix A), and then suddenly displace the trap minimum by a distance Δx . Subsequently, we let the atom slide down the potential hill, and after a time t , we use fast matter wave interferometry to measure how far its quantum state has evolved.

Our interferometry technique is illustrated in Fig. 1(a). At $t=0$, we put the atom in an equal superposition of two internal states, $|\uparrow\rangle$ and $|\downarrow\rangle$, using a fast Raman pulse (Appendix B). Each spin state is subject to a different

potential¹⁷, U_\uparrow and U_\downarrow (Appendix C). The atom in state $|\uparrow\rangle$ experiences a Δx -displaced potential, as described above. Conversely, the atom in state $|\downarrow\rangle$ is maintained unchanged (up to a global phase) in the vibrational eigenstate n of its trapping potential, where it is originally prepared¹⁸ before applying the Raman pulse. Thus, by such a splitting of the matter wave, we effectively create two copies of the same state, where one undergoes the intended downhill evolution, and the other remains stationary, serving as a reference for the state at $t=0$.

After a given evolution time t , we let the two copies interfere with each other by applying a second fast Raman pulse, akin to a Ramsey interrogation scheme. Crucially, both Raman pulses must be much shorter than the time scale for the quantum state evolution, $\max\{\tau_{MT}, \tau_{ML}\}$, which we anticipate to be in the microsecond range. In the experiment, we achieve pulse durations as short as 45 ns, thus ensuring that their action is nearly instantaneous and not affected by the trapping potential.

With this fast interrogation technique, we obtain all three quantities needed to test Eqs. (1a) and (1b): the two-time state overlap $|\langle\psi(0)|\psi(t)\rangle|$ as a function of time t , the mean energy E , and the energy uncertainty ΔE . To this purpose, we record the probability, p_\downarrow , to find the atom in state $|\downarrow\rangle$ as a function of the Ramsey control phase φ_R , i.e., the relative phase between the first and second pulse. This measurement yields a typical Ramsey fringe [Fig. 1(b)], characterized by a visibility $\mathcal{V}(t)$ and a phase $\varphi(t)$ (Appendix D). Importantly, these two quantities combined yield the complex-valued overlap integral, $\langle\psi(0)|\psi(t)\rangle = \mathcal{V}(t) \exp\{-i[\varphi(t) + E_n t/\hbar]\}$, where E_n is the energy of the stationary state n , with the ground state energy chosen to be zero ($E_0 \equiv 0$). Thus, the visibility directly gives us the two-time state overlap, i.e., the first of the three quantities to be measured.

We obtain E , the second quantity to be measured, from the phase of the Ramsey fringe, $\varphi(t)$, by expanding it for short times¹⁹,

$$\varphi(t) = (E - E_n)t/\hbar + O(t^3), \quad (2)$$

and knowing the energies E_n from sideband spectroscopy measurements¹⁸. Hence, tracking the phase evolution for short times, we extract E from the linear term of a fifth-order polynomial fit [Fig. 1(c)].

From the short-time expansion of the visibility¹³, we obtain the third quantity to be determined, ΔE :

$$\mathcal{V}(t) = 1 - (\Delta E t/\hbar)^2/2 + O(t^4). \quad (3)$$

This expansion establishes a relation between the short-time evolution and ΔE , which is well recognized in the literature on the quantum Zeno effect²⁰. It is important to underline that the MT bound of Eq. (1a) is a statement about the quantum evolution speed that, unlike Eq. (3), is not constrained to the short-time limit.

Testing quantum speed limits.—In Fig. 2 we present three representative data sets of the two-time state overlap, with $n=0$ and initial displacements Δx set to (a)

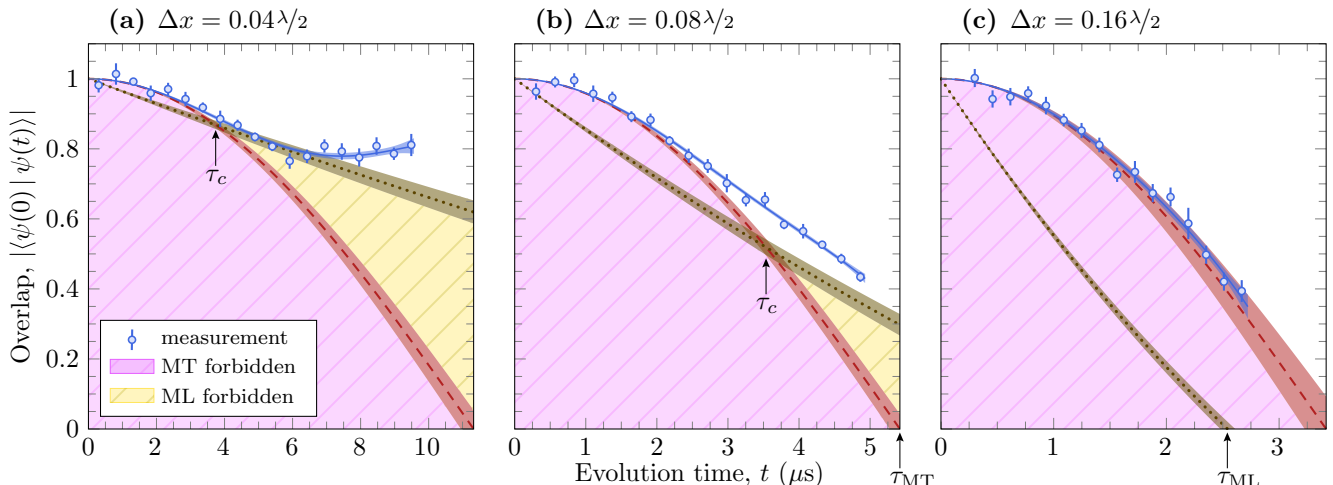


Figure 2. Quantum speed limits in a multi-level quantum system. Measured two-time state overlap vs evolution time for three displacements Δx from the trap center. The initial state is chosen with $n = 0$. Colored regions are those excluded by the MT (pink) and ML (yellow) bounds. The crossover time between the two speed limits is marked by τ_c . A sixth-order polynomial containing only even-power terms¹⁶ is fitted to the data points (solid line), from which we extract ΔE using Eq. (3). Shades around lines represent the 1- σ confidence region. Note that the x -axis domain extends up to τ_{MT} , whose value differs in each panel.

$0.04\lambda/2$, (b) $0.08\lambda/2$, and (c) $0.16\lambda/2$. Comparing the three data sets, we find that the two-state overlap drops at a faster rate for increasing values of Δx , meaning that the matter wave departs from its original state at a higher speed for increasingly larger excitations. We compare the data points to the lower bounds as predicted by the MT and ML speed limits in Eqs. (1a) and (1b). The regions excluded by the two bounds are hatched in different colors. The remaining region is the one allowed by the unified bound, defined by the maximum of the two limits. From this comparison, we make two important observations. The first is that all data points fall within the allowed region, thus giving the first experimental confirmation of the unified bound. Deviations from this bound are quantitatively studied below. The second observation is that a crossover between the two limits is manifested in panels (a) and (b): The two-time state overlap is bounded from below by the MT bound for short times ($t < \tau_c$) and by the ML for longer times ($t > \tau_c$).

Quantum-speed-limit crossover.—To research the condition and origin of this crossover, we test a wide spectrum of experimental conditions, leveraging the great degree of control and flexibility of our setup: The potential exerted onto the atom originates from an optical lattice. The lattice has a period of $\lambda/2 = 433\text{ nm}$ and is sufficiently deep to suppress tunneling between adjacent sites when the atom populates the low energy states (Appendix C). The initial displacement can be controlled with sub-nanometer precision over the full range, $0 < \Delta x \leq 0.5\lambda/2$. We excite mostly bound states for $\Delta x \ll \lambda/2$ and, vice versa, mostly unbound states in the continuum for Δx at around $0.5\lambda/2$. Large displace-

ments, $\Delta x > 0.25\lambda/2$, allow us, in particular, to test the speed limit for a nonharmonic potential, where the curvature of the potential is inverted. Furthermore, we vary the type of excitation by choosing the shape of the initial atomic wave packet to have $n = \{0, 1, 2\}$ nodes along the direction of the motional excitation. Since states with $n > 0$ differ starkly from Gaussian-like states, their quantum evolution is substantially different from that of semiclassical matter waves.

We examine 34 combinations of parameters, and record for each of them a data set as those shown in Fig. 2. Inspecting individually each data set shows that the vast majority are bounded by the MT limit only. However, in a few cases, a crossover to the ML bound is manifested at longer times, as exemplified in panels (a) and (b). To explain the crossover condition, we display in Fig. 3 the extracted energy uncertainty ΔE and mean energy E , in terms of the reciprocal of the MT and ML orthogonalization times. The inset highlights cases where the crossover is clearly visible. As revealed by the diagram, the crossover between Eqs. (1a) and (1b) occurs when the orthogonalization times satisfy the condition $\tau_{\text{MT}} < \tau_{\text{ML}}$. The region defined by this condition is identified in the diagram by shades of color, with the color representing the crossover time, $\tau_c = \tau_{\text{MT}}^2/\tau_{\text{ML}}$ ($0 < \tau_c < \tau_{\text{MT}}$). We call this the ML regime, since the quantum state evolution is constrained by the ML bound for $t > \tau_c$. Conversely, we call $\tau_{\text{MT}} > \tau_{\text{ML}}$ the MT regime, since the evolution is solely constrained by the MT bound for all times.

To obtain insight into the origin of the crossover, we gather the points in three different groups according to the quantum number n . Remarkably, the points falling in ML region are only those with $n = 0$, and in particular

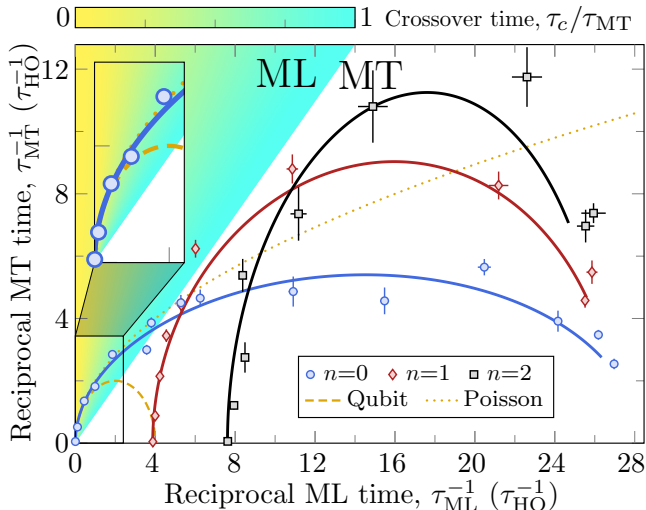


Figure 3. Quantum-speed-limit crossover. Measured orthogonalization times, τ_{ML} and τ_{MT} , displayed through their reciprocals, with n the quantum number characterizing the initial wave packet shape. Shades in color identify the ML regime, where a crossover manifests at time τ_c , as opposed to the MT regime, where no crossover occurs. Inset highlights data points in the ML regime. Points number 3, 5, 9 from the left of the series with $n = 0$ correspond to panels (a), (b), and (c) of Fig. 2. Solid lines show the expected curves computed with no free fitting parameter by numerical diagonalization of \hat{H} . The limiting case of a qubit (dashed line) and of a coherent excitation (dotted line) are also shown. Values are expressed in units of the reciprocal of the trap oscillation period, which is around 16 μ s.

those in the limit $\tau_{MT}^{-1} \lesssim \tau_{HO}^{-1}$, where $\tau_{HO} \equiv 2\pi/\omega_{HO}$ is the trap oscillation period in the harmonic approximation. This limit corresponds to small initial excitations, $\Delta E \lesssim \hbar\omega_{HO}$, when only very few levels are involved: mainly the original vibrational level n and with a small probability the additional levels $n \pm 1$ (or only level 1 when $n=0$). To understand why this limit falls in the ML regime, it is sufficient to consider the limiting case of a qubit subject to a static Hamiltonian. Representing the qubit as a spin precessing around a fixed axis at frequency $\omega_{HO}/(2\pi)$, one finds it always in the ML regime, as long as the lower level is more populated than the upper level (Appendix G).

By contrast, for large excitations, the distribution of the many excited levels is highly localized as a function of energy ($\Delta E < E$), yielding an evolution in the MT regime ($\tau_{MT} > \tau_{ML}$). An example interpolating the two limiting cases of small and large excitations is obtained by considering a coherent excitation in a harmonic potential (dotted line), where the population of the vibrational levels follows a Poisson distribution. Notably, this curve fits well only the $n = 0$ series for sufficiently small excitations. Its failure to fit the rest of the data reveals that the matter waves tested here include but are not limited to the semiclassical case of coherent excitations.

Deviation from the speed limit.—To gain insight into the mechanisms leading to deviations from the speed limit, we specifically consider the MT bound because it applies to both regimes. For a quantitative analysis, we take a geometric point of view, as proposed by Anandan and Aharonov¹³, which relies on the FS metric as a measure of the distance between states in Hilbert space. They showed that the length of the path traced by the time-evolved state equals $\ell(t) \equiv \pi t/(2\tau_{MT})$. On the other hand, the length of the shortest path (geodesic) connecting the initial state to that at time t amounts to the FS distance between the two states, $\ell_{geo}(t) \equiv \mathcal{D}[\psi(0), \psi(t)]$. The MT bound in Eq. (1a) can be expressed as $\ell(t) \geq \ell_{geo}(t)$, which has a clear geometrical interpretation—the MT bound is saturated only when the system evolves along a geodesic²¹. Using the definition of \mathcal{D} and the expansion in Eq. (3), we express the geodesic length as a series of powers of t/τ_{MT} :

$$\ell_{geo}(t)/\ell(t) = 1 - \frac{\pi^2\xi}{48} \left(\frac{t}{\tau_{MT}} \right)^2 + O(t^4), \quad (4)$$

where ξ is a dimensionless parameter empirically introduced to quantify the deviation of the state evolution from the geodesic. The foregoing geometrical condition, representing the MT bound, translates into $\xi \geq 0$.

We obtain the deviation coefficient ξ from a polynomial fit of the measured FS distance ℓ_{geo} for each data set examined above. The results are displayed in Fig. 4 as a function of the energy uncertainty ΔE . As expected, all data points fall within the allowed region. Surprisingly, however, the points coalesce around $\xi = 1$ regardless of the wave packet shape, the potential's anharmonicity, and for nearly all values of ΔE , save for the limiting case of very small excitations, discussed below. Such a coalescence hides a nontrivial relation with the energy uncertainty. In fact, for this result to hold, t in the power series in Eq. (4) must be expressed in units of τ_{MT} , which in turn depends on ΔE .

We attribute the observed strict deviations from the MT bound, $\xi > 0$, to the multi-level nature of our system. This result is in line with the well-known fact that only a qubit system can evolve along a geodesic²¹, and thus, saturate the MT bound. For a quantitative interpretation of the deviation coefficient, we derive its expression in terms of \hat{H} from the unitary evolution underlying the Schrödinger equation, $\xi = (\beta_2 - 1)/2$, where $\beta_2 = \langle (\hat{H} - E)^4 \rangle / \Delta E^4$ is the kurtosis of the energy spectrum. This expression reduces to $\xi = 1$ if we model the population of the vibrational levels by a Gaussian distribution as a function of energy.

It is nonetheless remarkable that the observed deviations are small on the scale of τ_{MT} . We explain this observation by the well-known fact in statistics that the majority of tailed distributions relevant to describe energy excitations have a kurtosis around 3, thus yielding $\xi \approx 1$ (Appendix E). Owing to the small factor $\pi^2\xi/48$ in Eq. (4), we therefore conclude that the MT speed limit establishes a relevant bound on the evolution rate of a

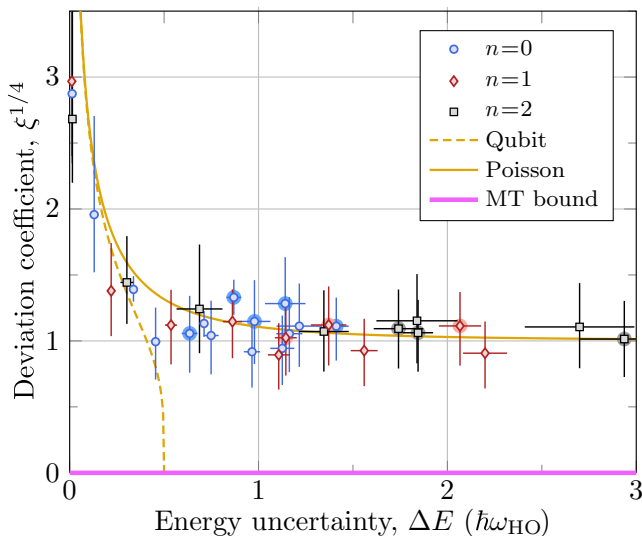


Figure 4. Deviations from the MT speed limit. The measured coefficient ξ is plotted vs ΔE for a wide spectrum of experimental conditions, varying the initial displacement Δx and the wave packet shape $n = \{0, 1, 2\}$. The pink line indicates the MT bound. Points corresponding to $\Delta x > 0.25 \lambda/2$ (nonharmonic regime) are highlighted by a surrounding circle. Note that for better visualization purpose the fourth root of ξ is plotted.

multi-level system subject to a time-independent Hamiltonian [see, e.g., Fig. 2(c)], in clear contrast to what observed in time-driven multi-level systems¹⁰.

The limit of small excitations, $\Delta E \lesssim \hbar\omega_{\text{HO}}$, reveals qualitatively different physics, with values of ξ significantly larger than 1. To obtain further insight, we consider the limiting case of a qubit, for which we find $\xi_{\text{qubit}} = 2(\Delta E_{\text{max}}^2/\Delta E^2 - 1)$, where $\Delta E_{\text{max}} = \hbar\omega_{\text{HO}}/2$ is the maximum energy uncertainty attainable by the qubit. This expression reveals a good agreement with the experimental data. It also shows that the bound is theoretically saturated ($\xi_{\text{qubit}} = 0$) for $\Delta E = \Delta E_{\text{max}}$, which occurs when the spin precesses along a great circle (the geodesic). In practice, however, this situation never occurs in our setup, since small excitations of the matter wave correspond to the case of the spin forming a very small angle with respect to the precession axis. In this limit, the evolved state is far from becoming orthogonal to the original one and, correspondingly, deviations from the MT bound are large on the scale of the orthogonalization time τ_{MT} . This situation is well exemplified by Fig. 2(a), which shows a cosine-like oscillation of the two-time state overlap, corresponding to a spin precessing with a small angle of about 40° . An interpolation between the qubit case ($\xi \gg 1$) and the foregoing multi-level Gaussian case ($\xi = 1$) is obtained considering the previous example of a Poisson distribution, which yields $\xi_{\text{HO}} = 1 + (\hbar\omega_{\text{HO}})^2/(2\Delta E)^2$. The comparison of this curve with the experimental data shows an excellent agreement, which also holds for $n = \{1, 2\}$ (Appendix F).

Concluding remarks.—Our study sheds light on two fundamental limits of quantum dynamics and their crossover. Thereby, we have uncovered the relevance of multiple levels in approaching the quantum speed limit. Unexpectedly, our measurements reveal that deviations from the MT bound are small in the case of multiple levels, despite the well-known fact that this bound can only be attained in a qubit system. Our results can find applications for quantum computing with continuous variables²², and quantum simulations in infinite-dimensional systems.

Key to our study is the ability to measure the two-time state overlap, which gives the FS distance covered by the evolving state. We emphasize the direct nature of this measurement, which, leveraging matter wave interferometry, does not require quantum state tomography nor any prior knowledge of the spectrum of \hat{H} . This technique is reminiscent of that used in Loschmidt echo experiments^{23,24}, with the notable difference that in our case one of the two branches of the Ramsey interferometer is held stationary in its initial state.

This work deals with quantum dynamics on the time scale of τ_{MT} . However, the same matter wave interferometer technique developed here can be used to explore quantum state evolution on a much longer time scale²⁵. We also envisage extensions of this technique to open quantum systems in order to measure the Bures distance (the FS distance analog) covered by mixed states under unitary²⁶ or non-unitary²⁷ evolutions. Understanding the quantum speed limit of open quantum systems is an important ongoing effort²⁸⁻³⁴.

Acknowledgments.—The authors would like to thank Jan Uckert for his contribution to the setup, Antonio Negretti for his critical reading, and Nir Davidson for helpful discussions. Also, the authors wish to pay tribute to Igor Mandelstam for his pioneering contribution, together with G. Landsberg, to the discovery³⁵ of Raman transitions, which are key to the fast interrogation scheme of this work. We thank C. Feuersänger for developing PGFPlots, which was used in this work. This research was supported by the Reinhard Frank Foundation in collaboration with the German Technion Society, and the SFB/TR 185 OSCAR of the German Research Foundation. G. N. is supported by the Helen Diller Quantum Center at the Technion, and M. R. L. by the German Academic Exchange Service.

Appendix A: Experimental sequence

An ensemble of ^{133}Cs atoms is cooled in a three-dimensional magneto-optical trap (MOT) and subsequently transferred into an optical trap consisting of a one-dimensional optical lattice formed by two counter-propagating laser beams with wavelength $\lambda \approx 866\text{ nm}$. About twenty atoms are sparsely loaded into the optical lattice, with a vanishing probability of having more than one atom per lattice site due to losses induced by light-assisted collisions. The initial number of atoms is measured by collecting the fluorescence light emitted by the atoms when these are illuminated by nearly resonant laser beams. Subsequently, the laser beams are kept on for an additional 10 ms with a reduced intensity and a larger detuning in order to cool the atoms into a low energy motional state. During loading, detection, and cooling of atoms, the lattice depth U_0 is set sufficiently large ($k_B \times 370\ \mu\text{K}$) to suppress the probability that an atom hops between lattice sites. Here, k_B denotes the Boltzmann constant.

For the preparation of the atom state and the subsequent experiments testing the quantum speed limits, the lattice depth is reduced to about $k_B \times 26\ \mu\text{K}$, corresponding to $270 E_R$, where $E_R = (2\pi\hbar)^2/(2m\lambda^2)$ is the recoil energy of an atom of mass m . Owing to the large value of U_0/E_R , tunneling between sites is completely negligible (Appendix C) when the atoms occupy a low energy motional state. For the low energy motional states, the trap potential can be approximated by a harmonic oscillator, with trap frequencies $\omega_{\text{HO}} \approx 2\pi \times 66\text{ kHz}$ in the direction longitudinal to the lattice, and $\approx 2\pi \times 1\text{ kHz}$ in the transverse directions. We note that the harmonic approximation in the longitudinal direction only applies in the limit of small excitations, i.e., for $\Delta x \lesssim \sqrt{\hbar/(m\omega_{\text{HO}})}$, or equivalently, $\Delta E \lesssim \hbar\omega_{\text{HO}}$. Also, due to the large difference between the two trap frequencies, the excitations in the longitudinal direction and in the transverse directions are decoupled.

We employ microwave sideband cooling¹⁸ to cool the atoms along the longitudinal direction into the vibrational ground state and, simultaneously, optically pump them to the Zeeman state $|F=4, m_F=4\rangle$ of the electronic ground state. A bias magnetic field of 3 G oriented in the lattice direction is used to define the quantization axis. The ground state population of the longitudinal motion is measured to be around $\gtrsim 96\%$ using sideband spectroscopy. Subsequently, a microwave π pulse transfers the atoms to state $|F=3, m_F=3\rangle$. By tuning the frequency of the pulse to be resonant with one of the motional sidebands, we selectively transfer the atoms into the desired vibrational level n of the U_{\downarrow} potential. The pulse fidelities are 95%, 85% and 68% for the eigenstates $n = \{0, 1, 2\}$, respectively. The atoms that are not successfully transferred remain in $|F=4, m_F=4\rangle$, and removed from the trap using an optical push-out pulse.

With the atom initialized in the vibrational level n , we adiabatically vary (Appendix C) in 300 μs the relative

position of the two lattices to reach the desired displacement, $0 < \Delta x \leq 0.5\lambda/2$, and then carry out the matter wave interferometer sequence (Appendix D), which consists of two fast $\pi/2$ pulses separated by a time t and resonant with the transition between the internal states $|\downarrow\rangle = |F=3, m_F=3\rangle$ and $|\uparrow\rangle = |F=4, m_F=3\rangle$.

After the second $\pi/2$ pulse, we remove the atoms in $|\uparrow\rangle$ with a second optical push-out pulse, increase the lattice depth, illuminate the atoms with nearly resonant light, and collect the emitted fluorescence light. We re-normalize the detected fluorescence by the fidelity of the π pulse used to prepare the atom in the vibrational level n , in order to compensate for the fraction of atoms removed by the first push-out pulse. The ratio between the re-normalized fluorescence and the initially detected one yields an estimate of p_{\downarrow} . To gain sufficient statistics, the sequence described above is repeated 10 times.

Appendix B: Fast Raman pulse setup

We employ a pair of phase-locked laser beams to drive the fast pulses of the matter wave interferometer by means of resonant two-photon transitions.

Before illuminating the atoms, the two beams are coupled into a common optical fiber and then sent through a double-pass acousto-optic modulator (AOM). By controlling the RF drive power of the AOM, we can temporally shape the intensity of the Raman pulses with nanosecond precision. On such a short time scale, the AOM intensity control exhibits a nonlinear response, which is taken into account and compensated using a look-up table. A second optical fiber is employed to overlap the Raman laser beams with one of the two laser beams forming the one-dimensional optical lattice (Appendix A). Thereby, we ensure that the Raman beams overlap perfectly with the optical trap, and that the momentum transferred to the atom by the Raman transition is negligible, since the two Raman beams are co-propagating.

The two Raman beams are red-detuned by about $2\pi \times 48\text{ GHz}$ from the cesium D_2 line. Because of the large detuning, the probability of an off-resonant photon scattering event during the pulse duration is negligible ($\approx 10^{-4}$). The frequency difference of the Raman beams is tuned to the hyperfine splitting of about $2\pi \times 9.2\text{ GHz}$, separating the two internal states $|\uparrow\rangle$ and $|\downarrow\rangle$. The two Raman laser beams illuminate the atoms with an individual power of 1.2 mW and the same circular polarization. This polarization enables σ -type transitions, since the quantization axis is collinear with the optical lattice (and, thus, with the Raman beams).

We achieve a high effective Rabi frequency $\Omega_R \approx 2\pi \times 6.5\text{ MHz}$ as a result of the high intensity of the Raman beams, which are tightly focused onto the atoms through a relatively small waist ($\approx 17\ \mu\text{m}$). Such a high intensity causes, in addition, a differential light shift of about 12 MHz, which is taken into account by tuning the frequency difference of the two Raman beams to be

resonant with the shifted transition. In the Ramsey interrogation scheme, this differential light field adds to the phase of the Ramsey fringe a linear shift in time by $81 \text{ rad } \mu\text{s}^{-1}$, which is subsequently subtracted from the Ramsey phase $\varphi(t)$.

The Rabi frequency Ω_R is mostly homogeneous over the entire ensemble of atoms, thus ensuring a high fringe visibility $\gtrsim 96\%$. We observe relative variations of less than one percent for atoms positioned at different lattice sites due to the collinearity of the Raman and lattice beams. Atoms have a small, but not vanishing temperature of about $1.5 \mu\text{K}$ in the directions transverse to the lattice, which cause to a distribution of the atoms' transverse positions and thus of the Rabi frequency. To reduce the inhomogeneous spread of the Rabi frequency, we use an additional blue-detuned hollow beam counter-propagating to the Raman beams to increase the confinement of atoms close to the optical axis, where the intensity of the Raman laser beams is maximal.

Appendix C: Spin-dependent optical lattice setup

The spin-dependent optical lattice setup is described in detail in Ref. ¹⁷. We employ two counter-propagating laser beams, each linearly polarized with an angle θ between their linear polarizations, to create two superimposed optical standing waves of right- and left-handed circularly polarized light. By controlling θ , we displace the two standing waves along their common axis by $\Delta x_{\text{sw}}(\theta) = (\theta/\pi)\lambda/2$ with sub-nanometer precision.

The light shift exerted on the atoms by the two standing waves gives rise to two spin-dependent optical lattices, U_{\uparrow} and U_{\downarrow} , which differ for the two spin states because of their specific polarization-dependent ac polarizability. At the wavelength λ , one can show that the potential U_{\uparrow} comprises two contributions proportional to the intensity of the right circularly polarized light (relative weight 7/8) and to the intensity of the left circularly polarized light (relative weight 1/8); the same expression holds for U_{\downarrow} , with the two polarization circularities being exchanged.

The two potentials, U_{\uparrow} and U_{\downarrow} , exhibit an ideal sinusoidal profile along the longitudinal direction, with a lattice constant equal to $\lambda/2$. Due to both standing waves contributing to the lattice potential, the displacement Δx between the two lattices has a slightly nonlinear dependence on the polarization angle,

$$\Delta x(\theta) = \frac{\tan^{-1}[3/4 \tan(\theta)]}{\theta} \Delta x_{\text{sw}}(\theta). \quad (\text{C1})$$

The trap depth U_0 is equal for both lattices. However, it slightly depends on the polarization angle θ ,

$$U_0(\theta)/U_0(0) = \sqrt{\frac{25 + 7 \cos(2\theta)}{32}} \quad (\text{C2})$$

again as a result of the contribution by both standing waves. The minimum trap depth is $U_0(\pi/2) = 3/4 U_0(0) \approx$

$200 E_R$ occurring when $\Delta x(\pi/2) = 0.5 \lambda/2$. Because the trap depth varies with θ (equivalently, Δx), the trap frequency also slightly depends on the displacement, $\omega_{\text{HO}}(\theta) = \sqrt{2U_0(\theta)/(m\lambda^2)}$.

In the deep lattice regime, $U_0 \gg E_R$, the atom has a negligible probability to tunnel to adjacent sites when it populates a low energy state. The low energy bands are virtually flat, and correspondingly the tunneling time is much longer than the microsecond time scale of the experiment. For example, the band with index $n = 0$ has a tunneling time greater than 1 year. By contrast, the energy bands with $n \gtrsim U_0/(\hbar\omega_{\text{HO}}) \approx 10$ resemble the dispersion relation of a free particle. The tunneling time varies nearly exponentially as a function of the band index n , changing by more than 12 orders of magnitude from $n = 0$ to $n = 10$. Hence, it is a very good approximation to consider states belonging to the low energy bands as effectively bound states, and vice versa states in the higher energy bands as unbound states.

Appendix D: Matter wave interferometry

The matter wave interferometer sequence shown in Fig. 1 is described in detail below. At time $t = 0$, the atom occupies $|\psi(0)\rangle \otimes |\downarrow\rangle$, where $|\psi(0)\rangle \equiv |n\rangle$ is one of the motional eigenstates of U_{\downarrow} potential. The first $\pi/2$ pulse, acting nearly instantaneously (Appendix B), puts the atom in a superposition both of spin states,

$$\frac{1}{\sqrt{2}} |\psi(0)\rangle \otimes (|\downarrow\rangle + |\uparrow\rangle), \quad (\text{D1})$$

where the atom's motional state remains unchanged during the short pulse. Afterwards, the atom is let evolve for a duration t , resulting in

$$\frac{1}{\sqrt{2}} \left[e^{-iE_n t/\hbar} |\psi(0)\rangle \otimes |\downarrow\rangle + |\psi(t)\rangle \otimes |\uparrow\rangle \right], \quad (\text{D2})$$

expressed in the frame rotating with the hyperfine frequency of the transition between the two spin states. A second fast $\pi/2$ lets the two branches of the superposition state interfere with each other, yielding

$$\frac{e^{-iE_n t/\hbar} |\psi(0)\rangle - e^{i\varphi_R} |\psi(t)\rangle}{2} \otimes |\downarrow\rangle + \frac{e^{-i(E_n t/\hbar + \varphi_R)} |\psi(0)\rangle + |\psi(t)\rangle}{2} \otimes |\uparrow\rangle, \quad (\text{D3})$$

where φ_R is the Ramsey control phase, which is varied by controlling the relative phase between the first and second pulse. Finally, a push-out pulse removes the atoms in state $|\uparrow\rangle$, and the probability p_{\downarrow} of occupying state $|\downarrow\rangle$ is measured as a function of φ_R , producing a typical Ramsey fringe,

$$p_{\downarrow}(\varphi_R) = \frac{1 - \mathcal{V}(t) \cos[\varphi_R - \varphi(t)]}{2}, \quad (\text{D4})$$

where the visibility $\mathcal{V}(t)$ and phase $\varphi(t)$ are related to the complex-valued overlap integral, $\langle \psi(0) | \psi(t) \rangle = \mathcal{V}(t) \exp\{-i[\varphi(t) + E_n t/\hbar]\}$. The fringe phase is shifted by an offset, $E_n t/\hbar$, where E_n is the energy of the vibrational level n with respect to the ground state, $E_0 = 0$, known by sideband spectroscopy¹⁸.

Appendix E: Tailedness of spectral distribution as a measure of deviation from MT bound

In the main text, the MT bound is shown to imply the inequality $\xi \geq 0$, where ξ is a coefficient accounting for the tailedness (kurtosis) of the spectral distribution of the excitation,

$$\xi = \frac{\langle (\hat{H} - E)^4 \rangle - \langle (\hat{H} - E)^2 \rangle^2}{2\langle (\hat{H} - E)^2 \rangle^2}. \quad (\text{E1})$$

A normal distribution has a deviation coefficient $\xi = 1$.

The distribution is said to be leptokurtic for $\xi > 1$ and platykurtic for $\xi < 1$. Leptokurtic are most of the tailed distributions describing excitations in a many-level system. By contrast, the most platykurtic distribution is notably the Bernoulli distribution with an equal probability of heads and tails, for which the deviation coefficient reaches its minimum possible value, $\xi = 0$. Such a distribution describes the excitation of a qubit with both eigenstates equally populated. Since the MT bound is saturated for this excitation, we thereby prove that $\xi = 0$ is not only a necessary but also a sufficient condition to saturate the MT bound.

It is interesting to observe that the numerator in Eq. (E1) is equal to the variance of $(\hat{H} - E)^2$, and must therefore be positive, thus providing an independent confirmation of the result derived from the MT bound.

Appendix F: Deviation coefficient in the harmonic approximation

At $t = 0$, the excited motional state is equal to the vibrational eigenstate $|n\rangle$ displaced by Δx ,

$$|\psi(0)\rangle = e^{-i\hat{p}\Delta x/\hbar} |n\rangle, \quad (\text{F1})$$

where \hat{p} is the momentum operator. In the harmonic approximation, valid for sufficiently small excitations, the

probability distribution for the case $n = 0$ is given by

$$p_{n=0}(n') = |\langle n' | \psi(0) \rangle|^2 = \frac{e^{-|\alpha|^2}}{n'!} |\alpha|^{2n'}, \quad (\text{F2a})$$

where $|\alpha| = \sqrt{m\omega_{\text{HO}}/(2\hbar)} \Delta x$ is the amplitude of the corresponding coherent state (m is the atomic mass). Using $p_{n=0}(n')$ to compute ξ in Eq. (E1), one obtains $\xi_{n=0} = 1 + (\hbar\omega_{\text{HO}})^2/(2\Delta E)^2$. Note that in the main text $\xi_{n=0}$ is denoted as ξ_{HO} .

For the other cases, $n = 1$ and $n = 2$, the probability distributions in the harmonic approximation are

$$p_{n=1}(n') = \frac{(|\alpha|^2 - n')^2}{|\alpha|^2} p_{n=0}(n'), \quad (\text{F2b})$$

$$p_{n=2}(n') = \frac{(|\alpha|^4 - 2r|\alpha|^2 + n'^2 - n')^2}{2|\alpha|^4} p_{n=0}(n'), \quad (\text{F2c})$$

yielding the coefficients $\xi_{n=1} = 1/3 + (\hbar\omega_{\text{HO}})^2/(2\Delta E)^2$ and $\xi_{n=2} = 7/25 + (\hbar\omega_{\text{HO}})^2/(2\Delta E)^2$, respectively. Notably, the expression of ξ exhibits for all three cases the same behavior in the limit of very small excitations, where mainly two states ($n = 0$) and three states ($n > 0$) are excited.

Appendix G: The qubit case

For very small excitations, $|\alpha| \ll 1$, the excited state in Eq. (F1) in the case of $n = 0$ reduces to two levels,

$$|\psi(0)\rangle \approx |0\rangle + |\alpha\rangle |1\rangle, \quad (\text{G1})$$

as in a qubit system.

In general, a qubit precessing with frequency $\omega_{\text{HO}}/(2\pi)$ around a fixed axis at an angle ζ has $\Delta E = \hbar\omega_{\text{HO}} \sin(\zeta)/2$, $E = \hbar\omega_{\text{HO}} \sin^2(\zeta/2)$ and the two-time state overlap

$$|\langle \psi(0) | \psi(t) \rangle| = \sqrt{1 - \sin^2(\zeta) \sin^2(\omega_{\text{HO}}t/2)}. \quad (\text{G2})$$

In the case the two states are equally populated, $\zeta = \pi/2$, the two-time state overlap in Eq. (G2) saturates the MT bound in Eq. (1a) for all times, $0 \leq t \leq \tau_{\text{MT}}$. In the case of no population inversion ($0 < \zeta < \pi/2$), as in Eq. (G1), we have $\Delta E > E$, meaning that the qubit is in the ML regime. For the other case of population inversion ($\pi/2 < \zeta < \pi$), we remark that a bound equivalent to the ML bound in Eq. (1b) can be derived considering the fact that the energy is limited from above,

$$|\langle \psi(0) | \psi(t) \rangle| \geq \cos \left[\sqrt{\cos^2(\zeta/2) \pi \omega_{\text{HO}} t/2} \right]. \quad (\text{G3})$$

-
- [1] L. Mandelstam and I. G. Tamm, “The Uncertainty Relation Between Energy and Time in Non-relativistic Quantum Mechanics,” *J. Phys. USSR* **9**, 249 (1945).
- [2] N. Margolus and L. B. Levitin, “The maximum speed of dynamical evolution,” *Physica. D* **120**, 188 (1998).
- [3] S. Lloyd, “Ultimate physical limits to computation,” *Nature* **406**, 1047 (2000).
- [4] V. Giovannetti, S. Lloyd, and L. Maccone, “Quantum limits to dynamical evolution,” *Phys. Rev. A* **67**, 052109 (2003).
- [5] L. B. Levitin and T. Toffoli, “Fundamental Limit on the Rate of Quantum Dynamics: The Unified Bound Is Tight,” *Phys. Rev. Lett.* **103**, 160502 (2009).
- [6] S. Deffner and S. Campbell, “Quantum speed limits: from Heisenberg’s uncertainty principle to optimal quantum control,” *J. Phys. A: Math. Theor.* **50**, 453001 (2017).
- [7] M. G. Bason, M. Viteau, N. Malossi, P. Huillery, E. Arimondo, D. Ciampini, R. Fazio, V. Giovannetti, R. Mannella, and O. Morsch, “High-fidelity quantum driving,” *Nat. Phys.* **8**, 147 (2011).
- [8] A. D. Cimmarusti, Z. Yan, B. D. Patterson, L. P. Corcos, L. A. Orozco, and S. Deffner, “Environment-Assisted Speed-up of the Field Evolution in Cavity Quantum Electrodynamics,” *Phys. Rev. Lett.* **114**, 233602 (2015).
- [9] S. van Frank, M. Bonneau, J. Schmiedmayer, S. Hild, C. Gross, M. Cheneau, I. Bloch, T. Pichler, A. Negretti, T. Calarco, and S. Montangero, “Optimal control of complex atomic quantum systems,” *Sci. Rep.* **6**, 34187 (2016).
- [10] M. R. Lam, N. Peter, T. Groh, W. Alt, C. Robens, D. Meschede, A. Negretti, S. Montangero, T. Calarco, and A. Alberti, “Demonstration of Quantum Brachistochrones between Distant States of an Atom,” *Phys. Rev. X* **11**, 011035 (2020).
- [11] G. N. Fleming, “A unitarity bound on the evolution of nonstationary states,” *Nuovo Cimento A Serie* **16**, 232 (1973).
- [12] K. Bhattacharyya, “Quantum decay and the Mandelstam-Tamm-energy inequality,” *J. Phys. A: Math. Theor.* **16**, 2993 (1983).
- [13] J. Anandan and Y. Aharonov, “Geometry of quantum evolution,” *Phys. Rev. Lett.* **65**, 1697 (1990).
- [14] The angle bracket notation denotes the expectation value of \hat{H} , or powers thereof, computed for the state $|\psi(t)\rangle$; as \hat{H} is time independent, so is its expectation value.
- [15] W. K. Wootters, “Statistical distance and Hilbert space,” *Phys. Rev. D* **23**, 357 (1981).
- [16] The even-power terms in Eq. (2) and the odd-power terms in Eq. (3) vanish due to the time-inversion symmetry of \hat{H} .
- [17] C. Robens, S. Brakhane, W. Alt, D. Meschede, J. Zopes, and A. Alberti, “Fast, High-Precision Optical Polarization Synthesizer for Ultracold-Atom Experiments,” *Phys. Rev. Appl.* **9**, 034016 (2018).
- [18] N. Belmechri, L. Förster, W. Alt, A. Widera, D. Meschede, and A. Alberti, “Microwave control of atomic motional states in a spin-dependent optical lattice,” *J. Phys. B: At. Mol. Phys.* **46**, 104006 (2013).
- [19] E. Sjöqvist, A. K. Pati, A. Ekert, J. S. Anandan, M. Ericsson, D. K. L. Oi, and V. Vedral, “Geometric Phases for Mixed States in Interferometry,” *Phys. Rev. Lett.* **85**, 2845 (2000).
- [20] S. Pascazio, “All You Ever Wanted to Know About the Quantum Zeno Effect in 70 Minutes,” *Open Systems & Information Dynamics* **21**, 1440007 (2014).
- [21] A. Uhlmann and B. Crell, “Geometry of State Spaces,” (Springer, Berlin, Heidelberg, 2009) p. 1.
- [22] S. L. Braunstein and P. van Loock, “Quantum information with continuous variables,” *Rev. Mod. Phys.* **77**, 513 (2005).
- [23] M. F. Andersen, A. Kaplan, and N. Davidson, “Echo Spectroscopy and Quantum Stability of Trapped Atoms,” *Phys. Rev. Lett.* **90**, 023001 (2003).
- [24] M. Cetina, M. Jag, R. S. Lous, I. Fritsche, J. T. M. Walraven, R. Grimm, J. Levinsen, M. M. Parish, R. Schmidt, M. Knap, and E. Demler, “Ultrafast many-body interferometry of impurities coupled to a Fermi sea,” *Science* **354**, 96 (2016).
- [25] M. R. Lam, G. Ness, W. Alt, D. Meschede, Y. Sagi, and A. Alberti, “Quantum imaging of an atomic wave packet reveals topological dynamics,” in preparation (2021).
- [26] D. Mondal and A. K. Pati, “Quantum speed limit for mixed states using an experimentally realizable metric,” *Phys. Lett. A* **380**, 1395 (2016).
- [27] K. Funo, N. Shiraishi, and K. Saito, “Speed limit for open quantum systems,” *New. J. Phys.* **21**, 013006 (2019).
- [28] M. M. Taddei, B. M. Escher, L. Davidovich, and R. L. de Matos Filho, “Quantum Speed Limit for Physical Processes,” *Phys. Rev. Lett.* **110**, 050402 (2013).
- [29] A. del Campo, I. L. Egusquiza, M. B. Plenio, and S. F. Huelga, “Quantum Speed Limits in Open System Dynamics,” *Phys. Rev. Lett.* **110**, 050403 (2013).
- [30] Y.-J. Zhang, W. Han, Y.-J. Xia, J.-P. Cao, and H. Fan, “Quantum speed limit for arbitrary initial states,” *Sci. Rep.* **4**, 4890 (2014).
- [31] D. P. Pires, M. Cianciaruso, L. C. Céleri, G. Adesso, and D. O. Soares-Pinto, “Generalized Geometric Quantum Speed Limits,” *Phys. Rev. X* **6**, 021031 (2016).
- [32] F. Campaioli, F. A. Pollock, F. C. Binder, and K. Modi, “Tightening Quantum Speed Limits for Almost All States,” *Phys. Rev. Lett.* **120**, 060409 (2018).
- [33] S. Deffner, “Quantum speed limits and the maximal rate of information production,” *Phys. Rev. Research* **2**, 013161 (2020).
- [34] E. O’Connor, G. Guarnieri, and S. Campbell, “Action quantum speed limits,” *Phys. Rev. A* **103**, 022210 (2021).
- [35] G. Landsberg and L. Mandelstam, “Über die Lichtstreuung in Kristallen,” *Z. Phys.* **50**, 769 (1928).

4.3 Summary

In this chapter we have verified the validity of the Mandelstam-Tamm and Margolus-Levitin inequalities for single atoms trapped in a static optical lattice potential. The bounds impose a maximum rate of change of the atomic wave packet evolution. The measurements here presented are the first experimental verification of the bounds for a multi-level system.

A crossover is observed from a region where the Mandelstam-Tamm is more restrictive to a region where the Margolus-Levitin bound is more restrictive. The crossover only happens when the energy spread of the evolving wave packet is higher than its mean energy. Otherwise, the Mandelstam-Tamm bound is more restrictive at all evolution times.

A geometric approach based on the Fubini-Study metric has been used to quantify the difference between the actual rate of change of the wave packets and the maximum rate of change imposed by the Mandelstam-Tamm bound. That has been done for wave packets prepared in 34 different initial states. Surprisingly, as the energy spread increases and more energy levels are populated, the wave packet evolution gets close to the bound. This is an important result since it reveals that the Mandelstam-Tamm bound is also relevant for some multi-level systems and not only for effective two-level systems.

Quantum drag racing

We made a drag race against quantum mechanics. We didn't win. We didn't loose. We got as far as it can be, a draw.

5.1 Introduction

In this chapter, our results on fast atom transport in optical lattices are presented, where the presence of a quantum speed limit is observed. The exact process consists in transporting the atoms, initially prepared in the motional ground state (Sec. 2.2.1), by a distance of one lattice site in the shortest possible time and in such a way that the atoms are back at their ground state at the end of the transport. We have observed that the atoms cannot be transported in a duration shorter than the quantum speed limit without compromising the transport's fidelity, quantified by the ground state population after the transport. In order to spatially move the atom, the position of the lattice is controlled as described in Sec. 2.1.6 and the atom is dragged by the lattice potential. The optimal transport trajectories are computed with optimal quantum control methods, which optimize the fidelity for a fixed distance and duration, experimentally measured with the technique presented in Sec. 2.2.2. The process can be thought of as a drag race with an additional rule: after accelerating from rest at the start line, the race car has to brake and reduce its speed back to zero (its ground state) exactly at the finish line (Fig. 5.1A). A low fidelity transport would then correspond to a race in which the pilot fails to stop the car exactly at the finish line, meaning that either the car doesn't reach the finish line at all, or it reaches it with a non-zero speed (it is not back at its ground state).

Atom transport without final motional excitations is essential for measurements that rely on matter wave interference, such as quantum walks and single atom interferometers. For this reason, we have realized a Mach–Zehnder single-atom interferometer with optimal control transport trajectories in order to verify if coherence is preserved during the transport process. The interferometer splits the atomic wave packet in two spin components (the hyperfine states $|3, 3\rangle$ and $|4, 4\rangle$), each one trapped by one of the two components of the spin-dependent lattice (Sec. 2.1.2). The spin state $|4, 4\rangle$ is transported by one lattice site and then transported back to its original position. Meanwhile, the component in the $|3, 3\rangle$ spin state is kept static and used as a reference. An unwanted position wobbling of the $|3, 3\rangle$ state, induced by the transport of the $|4, 4\rangle$ state, Eq.(2.11), is suppressed as explained in Sec. 2.2.5. The coherence of the transport operation is quantified by Ramsey interferometry and the results confirm that the optimal control transport operations preserve coherence. Coherent transport can be alternatively achieved by adiabatic transport. However, adiabatic processes are typically slow, meaning that the number of operations that can be realized within the coherence time of the system is reduced. By speeding up the transport operation

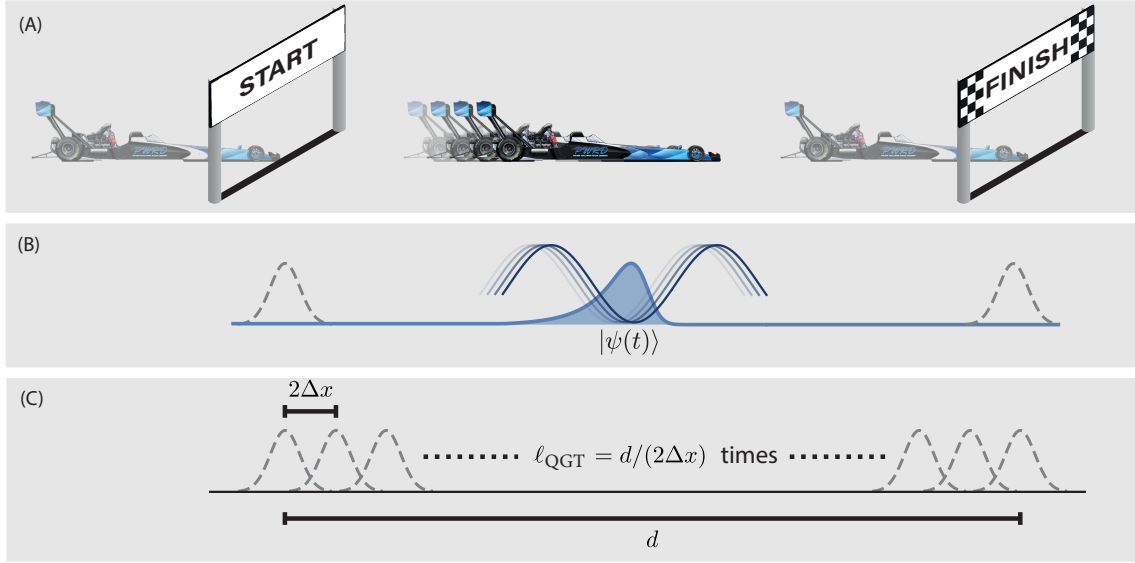


Figure 5.1: **Quantum drag race.** (A) Our atom transport operation is analogous to a usual drag race in which the car starts from rest and accelerates when the light turns green, except that we add the extra rule that the car has to go back to rest exactly at the finish line. (B) In the same way, our atom start at the initial position in the motional ground state and are transported to the target position in such a way that they are back in the motional ground state after the transport process. (C) The quantum geometric tensor provides a measure of distance between initial and target states in the Hilbert space. The distance defined by the quantum geometric tensor ℓ_{QGT} increases linearly with the spatial distance between the atomic wave packets d and can be seen as the number of local operations (between wave packets separated by a spatial distance $2\Delta x$, with Δx being the width of the wave packet) required to move the atom from the initial to the target position.

we are effectively increasing the number of operations that can be realized. This is why speeding up quantum processes is so important in the field of quantum technologies.

Given that reducing the duration of quantum processes is a common effort in quantum technologies, it is advantageous to have a good estimate of the fundamental limit that cannot be overcome by technical improvements on the system. In Chapter 4, we have seen that the Mandelstam-Tamm bound provides a good estimate of the minimum duration of quantum processes in some systems. However, it is well known that for complex systems that cannot be effectively reduced to a two-level system, the bound may provide absurdly small values [29]. In such cases the bound is useless and falls short of reflecting the true limit. The atom transport operations presented in this chapter belong to such type of processes. In fact, for long transport distances d for which the initial and target states are orthogonal, the minimum duration predicted by the Mandelstam-Tamm bound is independent of d , as opposed to the expectation that it scales with \sqrt{d} . We found out that this issue originates from the fact that for transport distances longer than the size of the atomic wave packet¹ $d \gg \Delta x$, the Fubini-Study distance [86, 87] between the initial and final states in the Hilbert space is always $\ell_{\text{geo}} = \pi/2$, independently of d . However, for initial and target states separated by such long spatial distances, the geodesic² according to the Fubini-Study metric is unphysical [29]. This is because a state following the geodesic would have to follow a Rabi-type transfer between two spatially distant locations, something impossible for massive particles. To solve

¹ Please note that in this chapter Δx refers to the width of the wave packet, as opposed to chapter 4 where it refers to the lattice displacement.

² In a metric space, the geodesic is the path that minimizes the distance between two states.

this, the process has to be restricted to the physically accessible states. This is done with the quantum geometric tensor (QGT), which depends on the controllable parameters of the system and defines a distance between quantum states in such a way that the geodesic is restricted to the physically accessible states. As a consequence, the distance defined by the quantum geometric tensor ℓ_{QGT} can be much longer than the distance defined by the Fubini-Studi metric ℓ_{geo} . In fact, in the case of atom transport by a distance d we find $\ell_{\text{QGT}} = d/(2\Delta x)$. Therefore, ℓ_{QGT} increases linearly with the transport distance as opposed to ℓ_{geo} which stagnates at $\pi/2$. Interestingly, ℓ_{QGT} can be thought of as the number of local operations required to transport the atom from the initial to the target position (Fig. 5.1C). With this at hand, we have derived an estimate of the minimum transport duration based on the quantum geometric tensor. We have found that the estimate is consistent with the theoretically expected scaling of the transport duration versus transport distance and is consistent with the experimental results as well.

Demonstration of Quantum Brachistochrones between Distant States of an AtomManolo R. Lam,¹ Natalie Peter,¹ Thorsten Groh¹, Wolfgang Alt¹, Carsten Robens^{1,2}, Dieter Meschede,¹ Antonio Negretti³, Simone Montangero⁴, Tommaso Calarco,⁵ and Andrea Alberti^{1,*}¹*Institut für Angewandte Physik, Universität Bonn, 53115 Bonn, Germany*²*MIT-Harvard Center for Ultracold Atoms, Research Laboratory of Electronics, and Department of Physics, Massachusetts Institute of Technology, Cambridge, Massachusetts 02139, USA*³*Zentrum für Optische Quantentechnologien, Fachbereich Physik, and The Hamburg Centre for Ultrafast Imaging, Universität Hamburg, 22761 Hamburg, Germany*⁴*Dipartimento di Fisica e Astronomia “G. Galilei,” Università degli Studi di Padova, and Istituto Nazionale di Fisica Nucleare, 35131 Padova, Italy*⁵*Forschungszentrum Jülich, 52428 Jülich, and Universität zu Köln, 50937 Köln, Germany* (Received 1 October 2020; revised 9 November 2020; accepted 21 January 2021; published 19 February 2021)

Transforming an initial quantum state into a target state through the fastest possible route—a quantum brachistochrone—is a fundamental challenge for many technologies based on quantum mechanics. In two-level systems, the quantum brachistochrone solutions are long known. These solutions, however, are not applicable to larger systems, especially when the target state cannot be reached through a local transformation. Here, we demonstrate fast coherent transport of an atomic wave packet over a distance of 15 times its size—a paradigmatic case of quantum processes going beyond the two-level system. Our measurements of the transport fidelity reveal the existence of a minimum duration—a quantum speed limit—for the coherent splitting and recombination of matter waves. We obtain physical insight into this limit by relying on a geometric interpretation of quantum state dynamics. These results shed light on a fundamental limit of quantum state dynamics and are expected to find relevant applications in quantum sensing and quantum computing.

DOI: [10.1103/PhysRevX.11.011035](https://doi.org/10.1103/PhysRevX.11.011035)

Subject Areas: Quantum Physics

I. INTRODUCTION

How fast can a quantum process be? Previous efforts to answer this question have resulted in fundamental insights into quantum state dynamics [1–7] and shed light on the ultimate physical limits to the rate of information processing [8–10]. Speeding up the dynamics of a quantum process is also key to advance quantum technologies [11–13], because faster processes can help us outrun detrimental decoherence mechanisms, and so boost the number of high-fidelity operations executed within the system’s coherence time [14–16].

The fact that a minimum time is required to accomplish a physical process has been known since Bernoulli’s famous brachistochrone problem [17], long before the advent of quantum physics. The origin of such a minimum time can be traced back to the maximum rate at which a physical

state can change in time, which is generally determined by the amount of physical resources (energy and type of control) available to carry out the process.

For quantum processes, a precise formulation of such a speed limit was first derived by Mandelstam and Tamm [1] considering the transformation of a quantum state $|\psi_{\text{init}}\rangle$ into an orthogonal one $|\psi_{\text{target}}\rangle$. They discovered that the duration τ_{QB} of the fastest process—the quantum brachistochrone—is bound by the inverse of the energy uncertainty [18],

$$\tau_{\text{QB}} \geq \tau_{\text{MT}} = \frac{\hbar\pi}{2\Delta E}, \quad (1)$$

providing a firm basis for Heisenberg’s time-energy uncertainty principle [19]. Most significantly, the Mandelstam-Tamm bound shows that the duration of a quantum process cannot vanish, unless infinitely large energy resources can be controlled. This bound was generalized to time-dependent Hamiltonians, making it applicable to a far larger class of quantum processes [2]. Further extensions have been obtained for generic target states not necessarily orthogonal to the initial one [20–22], open quantum systems [23–26], semiclassical systems [27,28], and optimal quantum control problems [29–33]. An experimental

*alberti@iap.uni-bonn.de

Published by the American Physical Society under the terms of the Creative Commons Attribution 4.0 International license. Further distribution of this work must maintain attribution to the author(s) and the published article’s title, journal citation, and DOI.

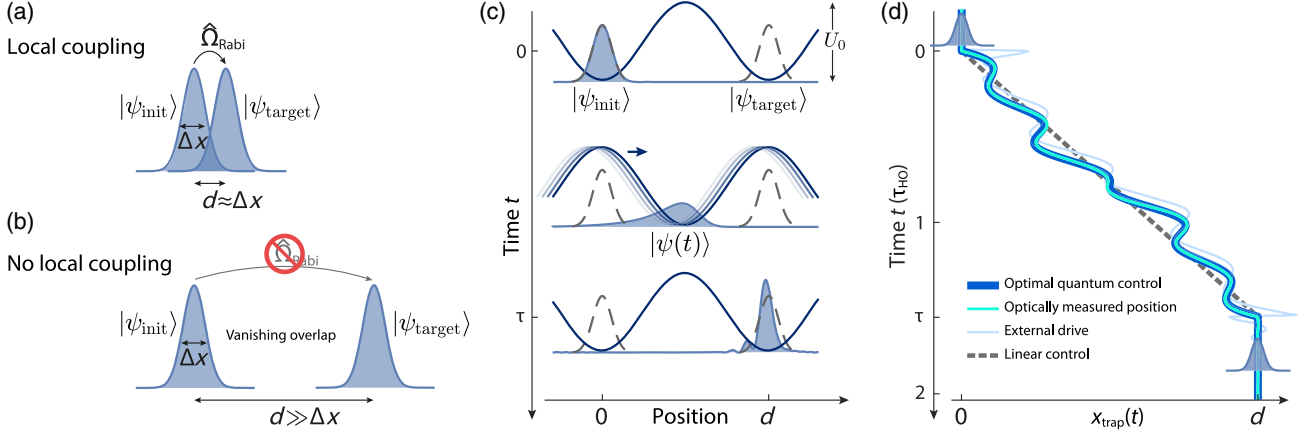


FIG. 1. Transporting a massive quantum particle to a distant state. (a) Direct local coupling $\hat{\Omega}_{\text{Rabi}}$ between the initial and target state can be realized when the two wave functions have nonzero spatial overlap. (b) Fundamentally, no direct local coupling between the two states can be realized for large separations, $d \gg \Delta x$, suppressing the possibility to attain the Mandelstam-Tamm bound. (c) Atom transport in an optical conveyor belt (sinusoidal potential curves), depicted at the initial, intermediate, and final time of the process. The probability distribution of the transported wave packet $|\psi(t)\rangle$ is shown (shaded area), together with that of the initial and target states (dashed lines). For illustration purposes, the chosen example shows a wave packet ending up in an excited state, corresponding to a low ($\mathcal{F} \sim 0.5$) transport fidelity. (d) Quantum brachistochrone trajectory $x_{\text{trap}}(t)$ of the optical conveyor belt (dark blue), corresponding to the diamond data point marked by an arrow in Fig. 2. The actual position of the conveyor belt (cyan), measured with 1 Å precision by optical interferometry, and the corresponding external drive (light blue), applied to steer the conveyor belt position, are also shown. For comparison, a linear transport ramp (dashed line) is displayed.

demonstration of the Mandelstam-Tamm bound in Eq. (1) was given in effective two-level systems using ultracold atoms [34,35] and superconducting transmon circuits [36].

II. QUANTUM BRACHISTOCHRONES BETWEEN DISTANT STATES

Today, it is understood [4,37,38] that the Mandelstam-Tamm bound in Eq. (1) can only be saturated (i.e., $\tau_{\text{QB}} = \tau_{\text{MT}}$) when the quantum dynamics can be reduced to that of a simple two-level system, i.e., when the target state can be reached directly by a Rabi oscillation [Fig. 1(a)]. Recently, however, Bukov *et al.* [7] pointed out that such a simple Rabi oscillation dynamics connecting the two states may be hard, or even impossible, to be realized in many-level systems. Thus, the authors questioned the usefulness of the Mandelstam-Tamm bound for these processes, since it fails to capture their true quantum speed limit (i.e., $\tau_{\text{QB}} \gg \tau_{\text{MT}}$).

A paradigmatic example of such a process would be “teleporting” a massive quantum object between distant quantum states through a Rabi oscillation, which is fundamentally impossible because no direct coupling between them [39] can be realized by physical local operators [Fig. 1(b)]. In fact, any physical operator $\hat{\Omega}_{\text{Rabi}}$ coupling directly the two states yields a vanishingly small Frank-Condon factor, $\langle \psi_{\text{init}} | \hat{\Omega}_{\text{Rabi}} | \psi_{\text{target}} \rangle \approx 0$.

In this work, we give the first experimental demonstration of coherent control of a physical process at its quantum speed limit beyond direct local operations. Specifically, we

consider the problem of transporting a trapped massive quantum particle to a distant location, separated by about 15 times the size of the wave packet, in the minimum possible time under the constraint of a fixed trap depth. The initial and target states are defined by the ground state of the trap potential centered at the two different locations. Because of the wide separation between the two states, it is fundamentally impossible for the massive quantum particle to reach the target state by a Rabi oscillation.

We see that inequality (1) fails to give a meaningful bound on the shortest transport duration τ_{QB} if we examine its scaling with respect to the transport distance d : While the minimum time τ_{QB} is naturally expected to increase with d , remarkably, the time τ_{MT} exhibits rather the opposite behavior, as it decreases with d (Appendix M). A way out of this conundrum is discussed below, adopting a geometric point of view on wave packet dynamics.

III. FAST ATOM TRANSPORT IN OPTICAL CONVEYOR BELTS

As of yet, transport experiments have been performed with trapped ions and ultracold atoms in the nearly harmonic low-energy portion of the trap potential [40–44], where fast, high-fidelity transport is enabled by effective protocols [45,46] known as shortcuts to adiabaticity. In order to reach the quantum speed limit, however, excitations of the wave packet beyond the low-energy range of the trap potential must be controlled, requiring precise knowledge of the full potential. For this purpose, we use a

one-dimensional optical lattice as a conveyor belt [47] to transport neutral atoms along its axis [Fig. 1(c)]. Its sinusoidal trap potential is inherently well defined over all spatial regions from trough to crest since it is created by optical interference of two counterpropagating laser beams (wavelength $\lambda \approx 866$ nm, lattice constant $\lambda/2$). We choose the trap depth U_0 of the order of $100E_{\text{rec}}$ in order to suppress tunneling of the initial state to adjacent sites; $E_{\text{rec}} = (2\pi\hbar)^2/(2m\lambda^2)$ is the recoil energy of an atom of mass m . We also maintain U_0 constant during the whole transport process to explore the scenario where the energy available to control a physical process is fundamentally limited; in fact, for an infinitely deep potential, no speed limit exists [45] in nonrelativistic quantum mechanics.

All transport experiments begin by preparing the matter wave of a ^{133}Cs atom into the motional ground state $|\psi_{\text{init}}\rangle$ of one of the sites of the optical conveyor belt (Appendix A), which is initially held at rest. Subsequently, we displace the conveyor belt within a given time τ to the desired target location following a chosen trajectory $x_{\text{trap}}(t)$ as a function of time t [Fig. 1(d)]. The target location is chosen to be one lattice site away ($d = \lambda/2$) from the initial location, corresponding to 15 times the initial size Δx of the wave packet. While the atomic wave packet is highly excited during transport, it ideally ends up in the ground state of the displaced potential, $|\psi_{\text{target}}\rangle$, once the optical conveyor belt is brought back to rest. We conclude the experiments by measuring (Appendix F) the fidelity of the transport process,

$$\mathcal{F}(\tau) = |\langle\psi_{\text{target}}|\psi(\tau)\rangle|^2, \quad (2)$$

quantifying the probability of occupying $|\psi_{\text{target}}\rangle$.

In the experiments, we control the position $x_{\text{trap}}(t)$ of the optical conveyor belt with high precision using a fast polarization synthesizer [48], reducing the position noise δx to much less than the size of the wave packet Δx ($\delta x \approx 0.1$ nm $\ll \Delta x \approx 25$ nm). We additionally suppress systematic distortions from the desired trajectory (Appendix E). Time-resolved measurements of $x_{\text{trap}}(t)$, carried out by on-site laser interferometry (Appendix D), reveal a nearly perfect agreement between the actual trajectory of the conveyor belt and the targeted one [Fig. 1(d)], with peak-to-peak discrepancies less than 10 nm.

IV. OPTIMAL TRANSPORT SOLUTIONS

For the transport of atoms, we choose a feed-forward quantum control approach [49]: we steer the conveyor belt along trajectories $x_{\text{trap}}(t)$ that are designed to maximize the transport fidelity. To obtain a trajectory $x_{\text{trap}}(t)$ of given duration τ , we take the solution for the corresponding classical problem (Appendix G) and subsequently optimize it using optimal quantum control methods [31,50,51] in order to achieve maximum fidelity $\mathcal{F}(\tau)$. For the fidelity

optimization, we employ numerical simulations of atom transport imposing two constraints: (1) $x_{\text{trap}}(t \leq 0) = 0$ and $x_{\text{trap}}(t \geq \tau) = d$ and (2) the Fourier spectrum of $x_{\text{trap}}(t)$ is limited to within the control setup bandwidth in order to ensure that $x_{\text{trap}}(t)$ is faithfully reproduced in the experiments (Appendix H).

The resulting optimal trajectories [Fig. 1(d)] exhibit a rather wiggling behavior, which is key to control excitations during transport. Disregarding the fast wiggles, the remaining behavior of $x_{\text{trap}}(t)$ is reminiscent of a constantly accelerated and decelerated trajectory for the first and second half of the transport duration. In addition, optimal trajectories notably start and finish with swift displacements, which are favorable to place the atomic wave packet where the trap potential is steep (Appendix G).

V. REVEALING THE QUANTUM SPEED LIMIT

Our measurements of the transport fidelity (Fig. 2) demonstrate that optimal quantum control solutions accomplish $\mathcal{F} \approx 1$ within experimental uncertainty for all transport times greater than τ_{QB} , occurring in the proximity of τ_{HO} , the oscillation period in the harmonic approximation of the trap potential (Appendix G). Crucially, for times shorter than τ_{HO} , the fidelity drops rapidly, revealing the existence of a minimum duration—a quantum speed limit—for the transport of matter waves. To our knowledge, this is the first observation of the quantum speed limit for a multilevel system, where the transition from a quantum-controllable to a quantum-noncontrollable process is sharply resolved by fidelity measurements. Our measurements reveal a rapid, yet smooth crossover around τ_{QB} , quite at variance with the analogous classical problem, where the transition between the two regimes is sudden [52].

We obtain insight about τ_{QB} by exploring the fidelity landscape $\mathcal{F}(\tau)$ as a function of τ , for different trap depths $U_0 \approx \{70, 150, 300\}E_{\text{rec}}$. By varying the trap depth, we change the number of effectively controlled energy levels (4,6,10, respectively), for which site-to-site tunneling is negligible over the transport duration τ . We determine the transition to a quantum noncontrollable process as the transport time at which the measured fidelity drops to $\mathcal{F}(\tau) \approx 0.5$ (inset of Fig. 2). Our measurements demonstrate that in the range of trap depths explored here, the quantum brachistochrone time τ_{QB} follows approximately τ_{HO} . Atom transport performed in a time close to τ_{HO} is notably much faster than its adiabatic counterpart, which requires on the contrary $\tau \gg \tau_{\text{HO}}$ (Appendix J). In Sec. VII we provide theoretical insight into the scaling of τ_{QB} , showing that the minimum transport time is bound from below by the classical brachistochrone time $\tau_{\text{CB}} \approx 0.8\tau_{\text{HO}}$ (hatched area in Fig. 2). This bound corroborates the experimentally observed scaling behavior of τ_{QB} with τ_{HO} , which quite differs from that of the MT bound τ_{MT} (dotted area in the same figure).

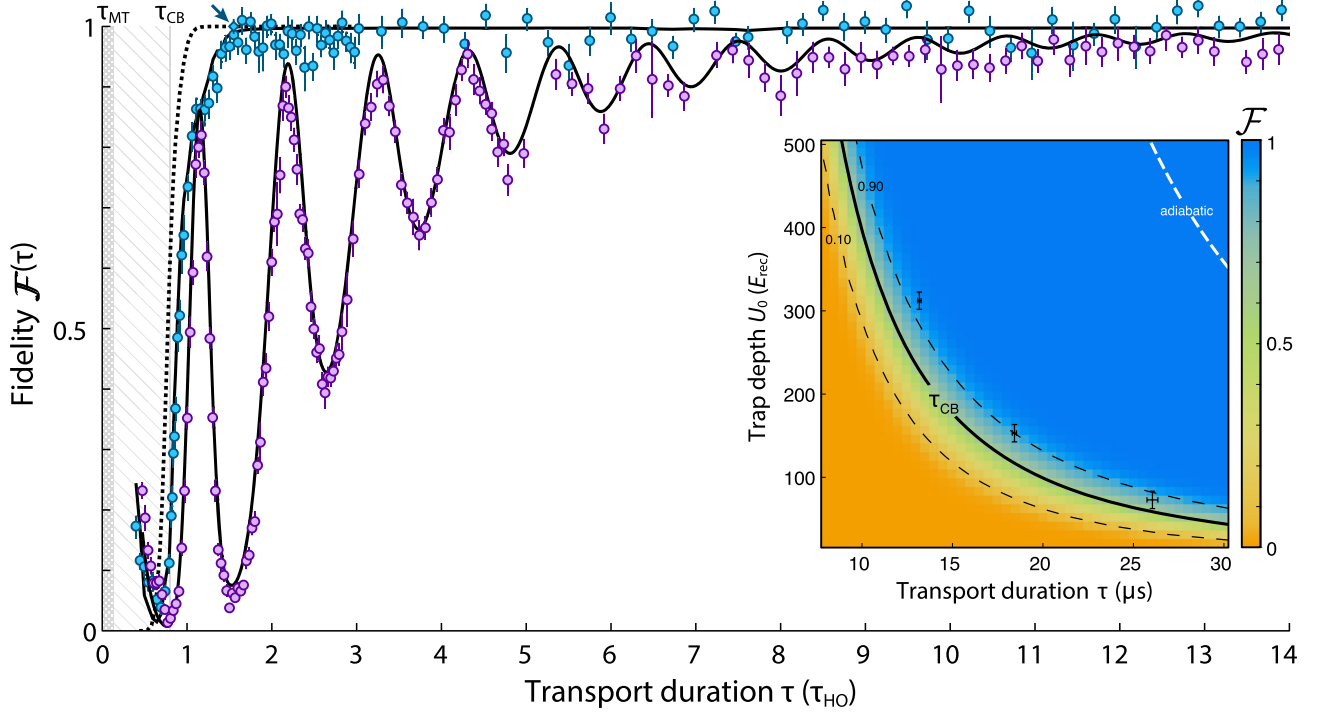


FIG. 2. Revealing the quantum speed limit. The fidelity $\mathcal{F}(\tau)$ of transporting an atom over one lattice site is measured as a function of the transport duration τ , expressed in units of the oscillation period $\tau_{\text{HO}} \approx 20 \mu\text{s}$, for a trap depth $U_0 \approx 150E_{\text{rec}}$. Blue points: optimal quantum control achieves near-unit fidelity for durations above the quantum brachistochrone time τ_{QB} (diamond point marked by an arrow), in the proximity of τ_{HO} . Hatched area: low-fidelity region as expected for durations shorter than the classical brachistochrone time τ_{CB} ; see Sec. VII. Dotted area: low-fidelity region predicted by the Mandelstam-Tamm bound τ_{MT} . Purple points: linear transport ramps achieve suboptimal fidelity. Black lines: computed fidelity based on numerical simulations of atom transport, assuming a transverse temperature $T_{\perp} \approx 1 \mu\text{K}$ (solid) and a zero-temperature case (dashed). Inset: the fidelity landscape computed numerically as a function of U_0 and τ for $T_{\perp} = 0$ (colored contour map) and the measured transition points (experimental data) where the fidelity reaches $\mathcal{F} \approx 0.5$. White lines: the oscillation period τ_{HO} , approximately representing the quantum brachistochrone time τ_{QB} , and the adiabatic limit ensuring fidelities $\mathcal{F} > 0.9$. Error bars represent one standard deviation.

To validate our experimental results, we employ numerical simulations of the transport process based on a one-dimensional model of the conveyor belt potential (Appendix C). A direct comparison of the computed fidelity with the measured $\mathcal{F}(\tau)$ reveals an excellent agreement with the simulations taking into account a thermal distribution in the transverse direction to the optical conveyor belt (Fig. 2). Relying on the numerical simulations, we are able to explain the rapid drop of fidelity observed when the transport duration is reduced below τ_{QB} : For short durations, high-energy excitations are created above the discrete spectrum of controlled energy levels, leading to a significant probability of tunneling to the neighboring sites and thus to a drop of fidelity. The occurrence of tunneling is especially evident in the limit of very short durations, $\tau \ll \tau_{\text{QB}}$. In this limit, in fact, the optical conveyor belt is displaced so fast that the atom has a considerable probability to remain in the very same state $|\psi_{\text{init}}\rangle$ where it was initially prepared. This possibility explains the apparent rise in fidelity for very short times observed in Fig. 2; such events could be singled out by

probing a small ensemble of individually resolved atoms, whose initial and final positions in the lattice can be precisely detected [53] in addition to measuring the ground state probability.

For comparison, we perform analogous transport experiments applying a simple linear transport ramp [Fig. 1(d)], corresponding to a bang-bang type of control (Appendix I), as opposed to optimal quantum control. In spite of its simplicity, bang-bang control enables faster-than-adiabatic high-fidelity transport, and finds wide applications in quantum technology [43]. The measured transport fidelity reveals maxima of $\mathcal{F}(\tau)$ when the transport duration is chosen to be a multiple of the oscillation period τ_{HO} (Fig. 2). In an ideal harmonic trap, these maxima are expected to reach unit fidelity owing to a perfect refocusing of motional excitations (Appendix I). Our measurements show, however, that such refocusing mechanism is only partially effective, owing to the anharmonicity of the conveyor belt potential. To reach fidelity values close to unity, long transport times are required, $\tau \gg \tau_{\text{HO}}$, rendering bang-bang control in

anharmonic potentials nearly as ineffective as adiabatic transport.

VI. COHERENT SPLITTING AND RECOMBINATION OF MATTER WAVES

To demonstrate that optimal quantum control transport is fully coherent, we conduct a second, closely related experiment, realizing a single-atom Mach-Zehnder interferometer. To this purpose, we create a copy of the initial atom wave packet with opposite spin direction, realizing a superposition of $|\uparrow\rangle$ and $|\downarrow\rangle$ states, subject to two fully independent, spin-selective optical conveyor belts [48]. Keeping the initial spin-down state at rest, we transport the spin-up state to the next lattice site employing an optimal quantum control trajectory of duration τ , and bring it back with the same trajectory reversed. We conclude the interferometer experiments by retrieving the contrast $\mathcal{C}(2\tau)$ of the interference fringe with a Ramsey interrogation scheme [54].

In analogy to our previous findings, the interferometer measurements reveal a high contrast for transport durations $\tau \gtrsim \tau_{\text{HO}}$, attesting to the fully coherent nature of the process (Fig. 3). The measured contrast is in fact directly related to the fidelity $\mathcal{F}_2(2\tau)$ of the process transporting the atomic wave packet back and forth: $\mathcal{C}(2\tau) = |\langle \psi_{\text{init}} | \psi(2\tau) \rangle| = \sqrt{\mathcal{F}_2(2\tau)}$. Moreover, if we make the assumption $\mathcal{F}_2(2\tau) \approx \mathcal{F}(\tau)^2$, we can trace $\mathcal{F}_2(2\tau)$ back to the single

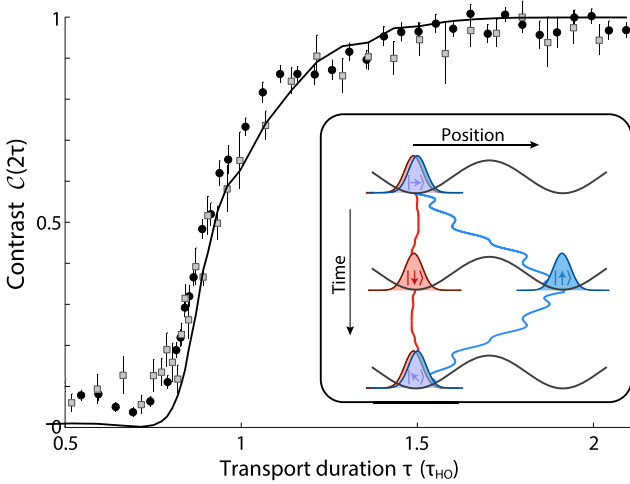


FIG. 3. Atom interferometry at the quantum speed limit. Square points: measured contrast $\mathcal{C}(2\tau)$ of the atom interferometer of duration 2τ , with the atom in $|\uparrow\rangle$ being transported with optimal quantum control back and forth. Circle points: measured fidelities $\mathcal{F}(\tau)$ from Fig. 2, reproduced here for comparison. Solid line: expected contrast obtained from numerical simulations assuming $T_{\perp} \approx 1 \mu\text{K}$. Error bars represent one standard deviation. Inset: the blue and red lines describe the movement of the spin-up and spin-down conveyor belts, ensuring that the atom in spin-down state remains effectively at rest, since the two spin-dependent potentials are not fully decoupled (Appendix B).

transport fidelity. The direct comparison of the measurements of the fidelity $\mathcal{F}(\tau)$ and contrast $\mathcal{C}(2\tau)$ reveals a striking similarity (Fig. 3). This comparison shows the importance of achieving high-fidelity transport operations for fully coherent quantum processes involving superposition of states.

VII. INTERPRETATION AND PHYSICAL INSIGHT

A basic interpretation of the quantum brachistochrone time τ_{QB} observed in the experiments is provided by the analog classical problem. There, the fastest process is realized when the particle is maximally accelerated for half of the time and then decelerated for the other half, with its position being centered at the points of steepest potential. This protocol results in the classical brachistochrone time, $\tau_{\text{CB}} = \tau_{\text{HO}} \sqrt{2n/\pi}$, where n represents the transport distance d expressed in units of the lattice constant $\lambda/2$ (Appendix G). When transporting a quantum particle, however, extra control is necessary to prevent too large spreading of the wave packet in the anharmonic potential [52], in particular when the wave packet approaches the points of steepest potential, where the trap loses its ability to confine. This additional requirement translates in a longer time to achieve a near-unit fidelity ($\tau_{\text{QB}} > \tau_{\text{CB}}$), yielding a lower bound on the quantum brachistochrone time,

$$\tau_{\text{QB}} > \tau_{\text{HO}} \sqrt{2n/\pi}, \quad (3)$$

where $n = 1$ is the case chosen for the experiments in this work. Comparing this bound to the measured data, which show near-unit fidelity for durations above τ_{HO} , validates the finding that the transport of atoms in our experiments attains the quantum speed limit.

Can the same bound in Eq. (3) be obtained from quantum mechanical principles? As we argued earlier, this question cannot be answered based on the Mandelstam-Tamm bound. Instead, we consider the quantum state evolution from a geometric point of view, as proposed by Anandan and Aharonov [2]. They prove that for every quantum process of duration τ , the average energy uncertainty ΔE [18] is related to the geometric path length of the time-evolved state $|\psi(t)\rangle$,

$$\ell = \int_0^{\tau} ds_{\text{FS}} = \Delta E \tau / \hbar, \quad (4)$$

measured by the Fubini-Study metric in the Hilbert space of quantum states, $ds_{\text{FS}}^2 = 1 - |\langle \psi(t+dt) | \psi(t) \rangle|^2$ [55]. Applying this relation to a quantum brachistochrone process, we directly obtain a lower bound on the quantum brachistochrone time, $\tau_{\text{QB}} > \hbar \ell_{\text{QB}} / \Delta E_{\text{upper}}$, provided that (I) the path length ℓ_{QB} of the process is known and (II) an

upper bound ΔE_{upper} on the average energy uncertainty can be provided.

To produce (I) and (II), we assume that at the quantum speed limit the wave packet is steadily accelerated in the first half and steadily decelerated in the second half, with its shape maintained close to that of a coherent state. Concerning point (I), under this assumption we can estimate the path length of the quantum brachistochrone process as the product of two factors (Appendix K),

$$\ell_{\text{QB}} \approx \frac{d}{2\Delta x} f\left(\frac{\tau_{\text{HO}}}{\pi\tau_{\text{QB}}}\right), \quad (5)$$

where $f(\xi) = \sqrt{1 + \xi^2} + \xi^2 \text{arccsch}(\xi)$ is a monotonically increasing function greater than 1 for positive arguments. Notably, the first factor in Eq. (5) coincides with the distance between the initial and final states as measured by the quantum geometric tensor (Appendix K),

$$\ell_{\text{QGT}} = \frac{d}{2\Delta x}. \quad (6)$$

In contrast to ℓ_{QB} in Eq. (5), ℓ_{QGT} is a purely geometric quantity independent of the dynamics of the process, since it represents the shortest path length as measured by the Fubini-Study metric in the restricted manifold of static states that are reachable via an adiabatic transformation of the control parameter x_{trap} (Appendix K). Equation (5) shows that ℓ_{QB} is larger than ℓ_{QGT} . This finding is in line with the conjecture put forth in Ref. [7] that ℓ_{QGT} is a lower bound on the path length ℓ of those processes that are realizable with the control parameters available (in this work, x_{trap}),

$$\ell \geq \ell_{\text{QGT}}. \quad (7)$$

The two factors in Eq. (5) can thus be interpreted as follows. The first factor ℓ_{QGT} is a measure of the change of $|\psi(t)\rangle$ when its position is moved across a distance d , which can be loosely understood as the number of local transformations necessary to carry out the transport process. The second factor f instead carries information about the dynamics, reflecting the change of $|\psi(t)\rangle$ when the momentum is varied during transport. Numerical simulations show that Eq. (5) approximates the actual ℓ_{QB} to within a few percent.

Concerning point (II), the determination of an upper bound on ΔE , we bound from above the potential contribution to the instantaneous energy uncertainty $\Delta E(t)$ by assuming the wave packet of size Δx to be positioned where the trap potential is steepest, at $\pm\lambda/8$ from the center of the site (Appendix K). By averaging over time [18], we thus find an upper bound ΔE_{upper} on ΔE , which remarkably can be expressed in the form

$$\Delta E < \Delta E_{\text{upper}} = \ell_{\text{QGT}} f\left(\frac{\tau_{\text{QB}}}{2n\tau_{\text{HO}}}\right) \frac{\hbar}{\tau_{\text{QB}}}, \quad (8)$$

where ℓ_{QGT} originates from the kinetic contribution to $\Delta E(t)$, whereas the second factor f stems from the trap potential contribution. Combining Eqs. (5) and (8) in the Anandan-Aharonov relation (4), we obtain

$$\tau_{\text{QB}} = \frac{\ell_{\text{QB}}}{\Delta E/\hbar} > \tau_{\text{QB}} f\left(\frac{\tau_{\text{HO}}}{\pi\tau_{\text{QB}}}\right) / f\left(\frac{\tau_{\text{QB}}}{2n\tau_{\text{HO}}}\right), \quad (9)$$

which, because of the monotonicity of f , directly translates in inequality (3), thus providing a positive answer to the question raised in the beginning. This result is consistent with the recent findings that the quantum speed limit is not a purely quantum phenomenon, but a universal property of the dynamics of physical states in Hilbert space [27,28].

The conjectured bound on the path length, Eq. (7), alone is not sufficient to yield a bound on τ_{QB} , since it does not take into account the dynamical contribution, represented by f in Eq. (5). Even so, this bound in Eq. (7) allows us to obtain novel insights applicable to any transport process that connects spatially distant states. In fact, using this bound, we find that ℓ is not just longer, but significantly longer than the geodesic—the shortest possible path as defined by the Fubini-Study metric—connecting the initial to the target state. The reason is that the geodesic coincides [56] with the path in Hilbert space traced by a Rabi oscillation ($\Omega = \pi/\tau$),

$$|\psi(t)\rangle = \cos(\Omega t)|\psi_{\text{init}}\rangle + \sin(\Omega t)|\psi_{\text{target}}\rangle, \quad (10)$$

whose length is $\ell_{\text{geo}} = \arccos(|\langle\psi_{\text{target}}|\psi_{\text{init}}\rangle|)$. Importantly, ℓ_{geo} levels off to $\pi/2$ for orthogonal states, regardless of the distance d separating the two states in real space, thus yielding $\ell \gg \ell_{\text{geo}}$ for $d \gg \Delta x$. The atom, in contrast, cannot evolve as in Eq. (10) because, as a massive particle, it cannot disappear from the initial location while reappearing at the target location [57], but must take a different much longer path.

The geometric relation just obtained, $\ell \gg \ell_{\text{geo}}$, is the fundamental reason why the Mandelstam-Tamm inequality falls short of giving a meaningful bound on the quantum brachistochrone duration, $\tau_{\text{QB}} \gg \tau_{\text{MT}}$. In fact, applying the Anandan-Aharonov relation (4) to the quantum brachistochrone process, we directly obtain $\tau_{\text{QB}} = \hbar\ell_{\text{QB}}/\Delta E \gg \hbar\ell_{\text{geo}}/\Delta E = \tau_{\text{MT}}$, where τ_{MT} designates here the Mandelstam-Tamm bound generalized [19] to the case of not necessarily orthogonal states.

VIII. CONCLUSIONS AND OUTLOOK

In this work, we have experimentally demonstrated high-fidelity transport of matter waves connecting spatially distant states in the shortest possible time, under the

constraint of a fixed trap depth. By splitting and recombining atomic matter waves, we showed that coherent quantum control is preserved at the quantum speed limit. By using geometric arguments, we showed how our transport experiments connecting distant states go beyond the quantum-speed-limit paradigm developed for single qubits and complex systems that can be effectively reduced to a two-level system [58], where the Mandelstam-Tamm bound is known to provide a meaningful lower bound on the shortest duration τ_{QB} . This work focused on a transport distance equal to one lattice site, which is the most relevant case for quantum walks [13]. Extending our results to much longer transport distances (Appendix L) is a very interesting goal, with applications in long baseline interferometry, which is key to boost the sensitivity of quantum sensors [59,60], to carry out fundamental tests of quantum superposition states [61], and to implement fault-tolerant quantum memories [62].

ACKNOWLEDGMENTS

We are indebted to Gal Ness, Yoav Sagi, Yutaka Shikano, Gonzalo Muga, Eugene Sherman, Jacob Sherson, and Carrie Ann Weidner for insightful discussions. This work is supported by the SFB/TR 185 OSCAR of the Deutsche Forschungsgemeinschaft (DFG). A. A. acknowledges support from the Reinhard Frank Foundation in collaboration with the German Technion Society, M. R. L. was supported by the Deutscher Akademischer Austauschdienst, A. N. acknowledges support from the Cluster of Excellence ‘‘CUI: Advanced Imaging of Matter’’ of the DFG, and C. R. is supported by a postdoctoral fellowship from the DFG.

APPENDIX A: ATOM TRAPPING AND COOLING

We load ^{133}Cs atoms from the background gas into a magneto-optical trap and subsequently transfer them into a superimposed one-dimensional optical lattice with a trap depth $U_0 \approx k_B \times 400 \mu\text{K} \approx 4000E_{\text{rec}}$, where k_B is the Boltzmann constant and $E_{\text{rec}} = (\hbar k)^2/(2m) = 2\pi\hbar \times 2 \text{ kHz}$ is the recoil energy; here, $k = 2\pi/\lambda$ is the wave number associated with the wavelength λ of the optical lattice, m is the mass of cesium atoms, and \hbar is the reduced Planck constant. The initial number of atoms is obtained by fluorescence imaging under near-resonant molasses illumination with an exposure time of 400 ms. A typical sample consists of 30 atoms loaded sparsely over 100 lattice sites. The molasses also cools the atoms further down by polarization gradient cooling. Adiabatically lowering the lattice trap depth to $k_B \times 80 \mu\text{K} \approx 800E_{\text{rec}}$ further cools the atoms down to around $10 \mu\text{K}$. This temperature corresponds to a longitudinal ground state population of around 40% as determined by microwave sideband spectroscopy.

A weak magnetic field of 3 G along the lattice axis provides a well-defined quantization axis. Relative to the quantization axis, we select two hyperfine states of

the ground state for the atom transport experiments, $|\uparrow\rangle = |F=4, m_F=4\rangle$ and $|\downarrow\rangle = |F=3, m_F=3\rangle$. In interferometer transport experiments, we use a superposition of both states, while for the other transport experiments we use state $|\uparrow\rangle$.

We cool the atoms down to the vibrational ground state along the longitudinal lattice direction by resolved sideband cooling using microwave radiation at 9.2 GHz [63]. More specifically, microwave sideband cooling is achieved by driving the cooling sideband $|\uparrow, n\rangle$ to $|\downarrow, n-1\rangle$, thereby removing one vibrational energy quantum $\hbar\omega_{\text{HO}}$, while simultaneously repumping the atoms to $|\uparrow\rangle$; here $\omega_{\text{HO}} = 2\pi$ denotes the harmonic oscillation frequency:

$$\omega_{\text{HO}} = 2\pi/\tau_{\text{HO}} = 2\pi\sqrt{\frac{2U_0}{m\lambda^2}}. \quad (\text{A1})$$

Microwave sideband transitions are enabled by displacing one of the spin potentials by around 17 nm along the lattice axis, lifting the orthogonality between different vibrational states. After sideband cooling for 20 ms, a longitudinal ground state population of typically 96% is reached.

In order to reduce the transverse temperature of the atoms, during molasses cooling we superimpose to the optical lattice a blue-detuned donut-shaped beam. Thereby, we increase the confinement of the atoms in the direction transverse to the optical lattice. By subsequently ramping down the intensity of the donut beam adiabatically, we lower the transverse temperature to $T_{\perp} \approx 1 \mu\text{K}$.

APPENDIX B: SPIN-DEPENDENT OPTICAL LATTICES

The optical lattice is operated at $\lambda = 865.9 \text{ nm}$, a so-called ‘‘magic’’ wavelength allowing atoms in the state $|\uparrow\rangle$ to be trapped only by the right-handed circularly polarized (R -polarized) light, while atoms in the state $|\downarrow\rangle$ are predominantly trapped by the left-handed circularly polarized (L -polarized) light. The dipole trap potentials for the two spin states are

$$U_{\uparrow} = -\alpha I_R, \quad (\text{B1a})$$

$$U_{\downarrow} = -\alpha\left(\frac{7}{8}I_L + \frac{1}{8}I_R\right), \quad (\text{B1b})$$

where I_R and I_L denote the intensity of the two circular polarization components of the lattice laser field, and the proportionality constant α only depends on cesium polarizability.

In order to create two fully independent optical conveyor belts transporting atoms selectively in either one of the two spin states, we employ a polarization-synthesized beam, where the phases ϕ_R and ϕ_L and the amplitudes of its left- and right-handed circularly polarized components are steered with high precision [48]. By interfering the

polarization-synthesized beam with a counterpropagating reference beam of fixed linear polarization, we create two perfectly superposed standing waves. The position of each standing wave,

$$x_{R,L}(t) = \frac{\lambda \phi_{R,L}(t) - \phi_0}{2\pi}, \quad (\text{B2})$$

is independently controlled by the phase $\phi_{R,L}(t)$ relative to the phase ϕ_0 of the counterpropagating reference beam. The conveyor belt potential for an atom in state $|\uparrow\rangle$ is simply

$$U_{\uparrow}(x, t) = -U_{0,\uparrow} \cos^2 \{k[x - x_{\uparrow}(t)]\}, \quad (\text{B3})$$

with $x_{\uparrow} = x_R$ and $U_{0,\uparrow} = \alpha I_R > 0$ being the trap depth; for the sake of notation, we simply use U_0 to refer to $U_{0,\uparrow}$ when only state $|\uparrow\rangle$ is involved. The conveyor belt potential for an atom in state $|\downarrow\rangle$ originates from the contribution of both polarization components, as indicated by Eq. (B1b), and takes the form

$$U_{\downarrow}(x, t) = -U_{\text{offs},\downarrow} - U_{0,\downarrow} \cos^2 \{k[x - x_{\downarrow}(t)]\}, \quad (\text{B4})$$

with

$$U_{0,\downarrow} = \frac{\alpha}{8} \sqrt{I_L^2 + 49I_R^2 + 14I_L I_R \cos(\phi_R - \phi_L)}, \quad (\text{B5a})$$

$$U_{\text{offs},\downarrow} = \frac{\alpha}{16} (I_L + 7I_R) - \frac{1}{2} U_{0,\downarrow}, \quad (\text{B5b})$$

$$x_{\downarrow} = \frac{\lambda}{4\pi} \arctan \left(\frac{I_L \sin(\phi_L) + 7I_R \sin(\phi_R)}{I_L \cos(\phi_L) + 7I_R \cos(\phi_R)} \right). \quad (\text{B5c})$$

Here, $U_{0,\downarrow} > 0$ and $U_{\text{offs},\downarrow} > 0$ are the contrast and offset of the spin-down conveyor belt potential (see Fig. 4).

The phase of each of the two polarization components $\phi_{R,L}(t)$ is controlled by two independent optical phase-locked loops (OPLLs) with respect to a common reference beam, using two acousto-optical modulators as actuators. The set points of the OPLLs are controlled by a direct digital frequency synthesizer (AD9954 by Analog Devices), enabling fast preprogrammed arbitrary phase ramps. The control system has a bandwidth of 800 kHz and a slew rate of $0.84 \text{ rad } \mu\text{s}^{-1}$. This slew rate limits the maximum speed of the lattice to 0.13 sites per μs (equivalently, 56 mm/s).

During the atom interferometer sequence described in the main text, the spin-down conveyor belt is kept static in order to preserve the spin-down wave function as a reference. To that purpose, we actively compensate the effect of the moving R -polarized standing wave onto U_{\downarrow} during the transport of the spin-up potential. We therefore suppress the position modulation with a compensation ramp ϕ_L (blue trajectory in the inset of Fig. 3 of the main text) that maintains x_{\downarrow} constant,

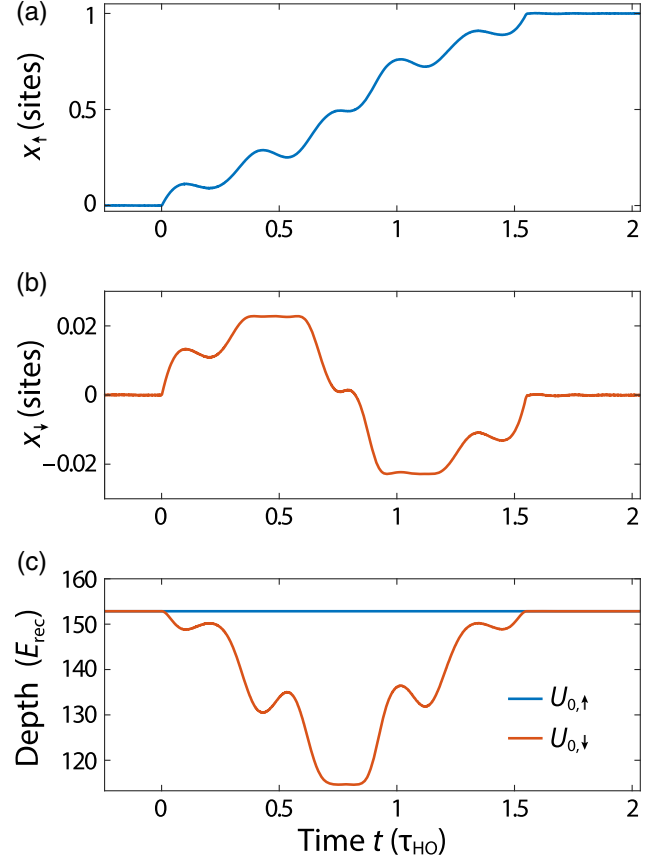


FIG. 4. Cross talk between spin-dependent potentials. Example of transport ramp as in Fig. 1(d) when varying $x_R(t)$ without compensating $x_L(t)$; i.e., $x_L(t) = x_L(0)$. (a) The position of the spin-up potential only depends on the R -polarized standing wave, $x_{\uparrow}(t) = x_R(t)$. The position (b) and depth (c) of the spin-down potential are modulated because of the cross-talk contribution from the moving R -polarized standing wave; see Eq. (B5).

$$\phi_L = -\arcsin \left(\frac{\phi_R}{7f(\phi_R)} \right), \quad (\text{B6})$$

where $f(\phi_R)$ is a rather involved analytical expression depending on ϕ_R . We do not compensate the depth modulation $U_{0,\downarrow}$, Fig. 4(c), because motional excitations of atoms in state $|\downarrow\rangle$ are predominantly caused by position modulation x_{\downarrow} , when the latter is not properly compensated.

APPENDIX C: SIMULATIONS OF ATOM TRANSPORT

For the numerical simulations of atom transport, we consider a one-dimensional model of the conveyor belt potential, as introduced in Appendix B, corresponding to the Hamiltonian:

$$\hat{H}(t) = \frac{\hat{p}^2}{2m} + U_0 \cos^2 \{k[\hat{x} - x_{\text{trap}}(t)]\}. \quad (\text{C1})$$

We assume that the atom occupies initially the lowest energy state of $\hat{H}(0)$. We compute the evolution of the wave packet in discrete time steps using the Strang split-step integration method [64].

In the transverse directions, a small, but nonzero temperature T_{\perp} characterizes the initial state of the atoms; see Appendix A. For the atom transport problem, the motion of atoms in the transverse directions can be considered as frozen. This assumption is justified by the large separation between the timescales of the longitudinal (20 μ s) and transverse (1 ms) motion. However, because of the thermal distribution of transverse positions, atoms experience a different trap depth U_0 depending on their distance from the lattice axis (inhomogeneous broadening). Such a distribution of trap depths reduces the transport fidelity, especially for short transport durations close to the quantum speed limit; see Fig. 2 of the main text. In the numerical simulations, we take into account the thermal distribution of transverse positions by assuming a two-dimensional Boltzmann distribution in the harmonic approximation of the transverse energy potential [63],

$$\mathcal{P}(r, T_{\perp}) = \frac{m\omega_{\perp}^2}{k_B T_{\perp}} r \exp\left(-\frac{m\omega_{\perp}^2 r^2}{2k_B T_{\perp}}\right), \quad (\text{C2})$$

where r is the transverse distance from the lattice axis and ω_{\perp} is the transverse trap frequency. The effective trap depth experienced by atoms as a function of r is

$$U_0(r) = U_0(0) \exp\left(-\frac{2r^2}{w_{\text{DT}}^2}\right), \quad (\text{C3})$$

where w_{DT} is the lattice beam waist and $U_0(0)$ is the depth on the lattice axis. The average fidelity for a thermal ensemble of atoms is then given by

$$\mathcal{F}(\tau, T_{\perp}) = \int_0^{\infty} dr \mathcal{F}(U_0(r)) \mathcal{P}(r, T_{\perp}), \quad (\text{C4})$$

where

$$\mathcal{F}(U_0) = |\langle \psi_{\text{target}} | \hat{V}(\tau, U_0) | \psi_{\text{init}} \rangle|^2. \quad (\text{C5})$$

Here, $\hat{V}(\tau, U_0)$ denotes the operator evolving the state for a time τ according to the Hamiltonian in Eq. (C1) with a trap depth U_0 . In practice, the integral in Eq. (C4) is replaced by a trapezoidal sum over about 10 different discrete values of r .

APPENDIX D: PRECISION OPTICAL MEASUREMENT OF TRANSPORT RAMPS

Measuring the actual trajectory of the conveyor belt with high precision is important to achieve high-fidelity transport operations. Indeed, knowledge of the actual trajectory

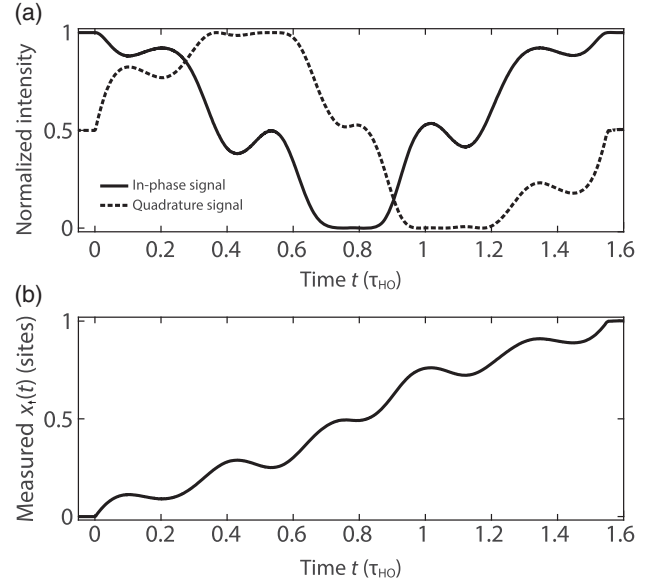


FIG. 5. Optical interferometric measurement of the trap trajectory. (a) Phase quadrature measurement of $\phi_R(t)$, showing the normalized intensities recorded after a Glan-Laser polarizer for the in-phase, $\{1 + \cos[\phi_R(t)]\}/2$, and the quadrature signal, $\{1 + \sin[\phi_R(t)]\}/2$. (b) Displacement $x_{\uparrow}(t) = (\lambda/2)\phi_R(t)/(2\pi)$ of the optical conveyor belt, reconstructed from the in-phase and quadrature signals.

allows us to compensate for deviations from the target optimal trajectory $x_{\text{trap}}(t)$; see Appendix E.

To that purpose, we developed an interferometric technique to reconstruct *in situ* the trajectory $x_{\uparrow}(t)$ and $x_{\downarrow}(t)$ of the optical conveyor belts for the two spin states: The conveyor belt trajectories are inferred via Eqs. (B3) and (B4) from the positions $x_R(t)$ and $x_L(t)$ of the R - and L -polarized optical standing waves, which are in turn obtained via Eq. (B2) from a time-resolved measurement of the optical phases $\phi_R(t)$ and $\phi_L(t)$ of the R - and L -polarized components that form the polarization-synthesized beam of the spin-dependent optical lattice.

The two phases are measured by using an optical phase quadrature detection scheme, which consists of inserting a Glan-Laser polarizer directly into the optical path of the polarization-synthesized beam, and detecting the intensity signal produced by the two interfering R - and L -polarized components. If, for example, we aim to detect $\phi_R(t)$, we then hold $\phi_L(t)$ constant at either $\phi_R(0)$ or $\phi_R(0) + \pi/2$. The recorded interference signals correspond to the in-phase and quadrature components of $\phi_R(t)$, respectively, from which it is straightforward to obtain $x_R(t)$; see Fig. 5.

APPENDIX E: AVOIDING DISTORTIONS CAUSED BY BANDWIDTH LIMITATION

Deviations from the target optimal trajectory, which are caused by the limited bandwidth of the control system,

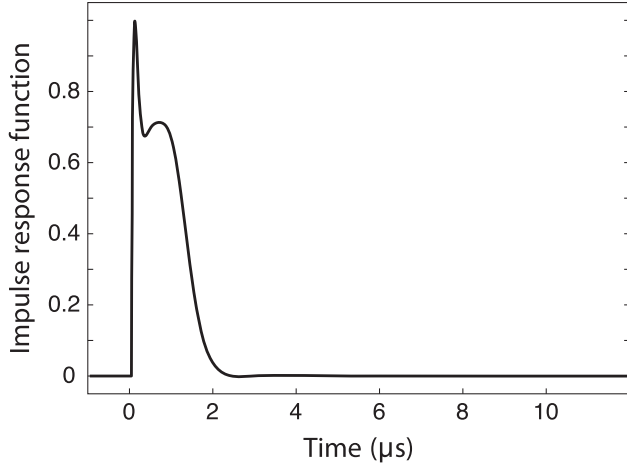


FIG. 6. Reconstructed impulse response function. The control bandwidth is mainly limited [48] by a time delay, which originates from the acousto-optical modulators employed in the optical phase-locked loop to control the phases $\phi_{R,L}(t)$; see Appendix A.

must be compensated in order to realize high-fidelity transport operations.

To that purpose, we initially assume a linear time-invariant control system, implying that its response to an external drive is fully characterized by its impulse response function. The impulse response function can be obtained as the derivative of the step response, which we measure with the technique described in Appendix D by recording the actual position of the conveyor belt after driving a sudden, small step of its position. The resulting impulse response function (Fig. 6) extends over a couple of microseconds, limiting the control bandwidth to below 1 MHz. By deconvolving the target optimal trajectory $x_{\text{trap}}(t)$ with the impulse response function, we obtain a first approximation of the external drive signal to be applied in order to avoid signal distortions.

In a second step, in order to also take into account nonlinearities of the control system, we iteratively reduce the residual deviations between the actual and the optimal target trajectory. In each iteration, the residual deviations are measured with the technique in Appendix D, and a fraction of them (typically 0.4 to avoid instabilities) is subtracted from $x_{\text{trap}}(t)$ before deconvolution. After 10 iterations, the difference between the measured and the target trajectories is over the whole transport duration below 2% of a lattice site, or equivalently, less than 10 nm. An example can be seen in Fig. 1(d) of the main text.

Using numerical simulations, we could verify that the deviations of the actual trajectory from the target one affected the transport fidelity by no more than 1%, which is within the experimental error. The reason why such deviations, which are comparable in size to the atomic wave packet, do not significantly affect the fidelity can be

explained in terms of two factors. (I) The target trajectory is an optimal one, meaning that the transport fidelity is affected by small deviations of the lattice trajectory only in second order. (II) The spectral distribution of the deviations from the target trajectory is important. High-frequency components, $\nu \gtrsim 3/\tau_{\text{HO}}$, are found to have small effect. In fact, the wave packet response at higher frequencies decreases akin to the response of a harmonic oscillator subject to a high-frequency drive.

APPENDIX F: PRECISION MEASUREMENT OF TRANSPORT FIDELITY

The fidelity \mathcal{F} of a transport operation is given by the fraction of atoms occupying the motional ground state $|\psi_{\text{target}}\rangle$ of the conveyor belt potential at the target position, as defined in Eq. (2) of the main text.

We measure the ground state fraction with a detection scheme that selectively removes atoms in higher motional states from the trap while retaining those in the ground state [63]: All atoms are first transferred from $|\psi_{\uparrow}\rangle$ to $|\psi_{\downarrow}\rangle$ with a fast microwave π pulse on the carrier transition, $|\uparrow, n\rangle \rightarrow |\downarrow, n\rangle$. Subsequently, the relative position $x_{\uparrow}(t) - x_{\downarrow}(t)$ between the spin-up and spin-down conveyor belts is adiabatically increased from zero to around 17 nm in order to enable microwave transitions on the motional sidebands. We perform 10 repetitions of a removal cycle, where first a microwave pulse on the sideband $|\downarrow, n\rangle \rightarrow |\uparrow, n-1\rangle$ transfers all atoms, except those in the ground state, to the spin-up state, and then a push-out beam resonant to the transition $|F=4\rangle \rightarrow |F'=5\rangle$ removes the transferred atoms by radiation pressure. The remaining fraction of atoms indicates the motional ground state population, with a typical statistical uncertainty at the 2% level.

To compensate for the imperfect initial state preparation, the reported values of the transport fidelity \mathcal{F} are normalized by the fidelity of the initial state preparation (around 96%; see Appendix A), which is measured by the same technique, but omitting the transport operation.

The fraction of atoms in the motional ground state, as measured with this scheme, does not discriminate whether the transported atom ends up in the ground state of the target site (true positive) or in that of an adjacent site of the optical lattice (false positive). The latter possibility has, however, a negligible probability to occur, unless the transport duration is significantly shorter than the quantum brachistochrone time τ_{QB} ; see Fig. 2 of the main text. Such false positive events could be separately detected and filtered out by resolving the individual lattice sites [53] in addition to measuring the ground state probability.

APPENDIX G: ANSATZ FOR OPTIMAL TRANSPORT TRAJECTORIES

For optimal control of the transport process (see Appendix H), it is important to start with a good ansatz

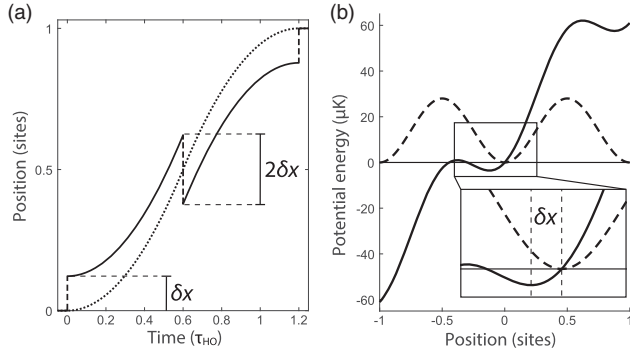


FIG. 7. Excitation-free classical trajectories. (a) The dotted curve shows the trajectory of a classical point particle being first constantly accelerated and then decelerated. The solid curve is the trajectory of the trap $x_{\text{ansatz}}(t)$, see Eq. (G2), required to drive the particle along the dotted curve. The example refers to $\tau = 1.2\tau_{\text{HO}}$ and $d = \lambda/2$, whereas δx is given by Eq. (G3). (b) The potential in the noninertial comoving frame (solid curve) is equal to the static potential (dashed curve) plus a linear tilt with slope $m\dot{x}_{\text{ansatz}}(t)$. The sudden shift by δx keeps the particle at the position of the potential minimum in the comoving frame, avoiding motional excitations (e.g., slosh motion).

of the transport trajectory $x_{\text{trap}}(t)$. We obtain it considering the classical analog of the atom transport problem: A classical point particle of mass m , initially at rest in a sinusoidal potential with lattice constant $\lambda/2$ and depth U_0 , is to be transported over a distance d in the shortest possible time such that it is again at rest after the transport. The optimal strategy evidently is to maximally accelerate the particle during the first half of the transport and maximally decelerate it during the second half. Thus, the optimal classical transport trajectory starts with a sudden lattice displacement equal to $\delta x = \lambda/8$, which places the particle at the point of steepest potential, where it is maximally accelerated. The lattice potential is then moved together with the particle in order to maintain maximum acceleration until the particle reaches half of the transport distance. At that point, the potential gradient is suddenly reversed by displacing the lattice by $-2\delta x$, thus ensuring maximum deceleration in the second half. The particle reaches the target position at zero speed, where a final sudden displacement by δx places the potential minimum at the particle's final position. The duration of this process is the classical brachistochrone time,

$$\tau_{\text{CB}} = \tau_{\text{HO}} \sqrt{2n/\pi}, \quad (\text{G1})$$

where $n = d/(\lambda/2)$ is the transport distance d expressed in number of lattice sites.

This protocol can be extended to any transport duration $\tau \geq \tau_{\text{CB}}$ by reducing the constant acceleration and deceleration below the maximum value, yielding the trajectory [Fig. 7(a)]

$$x_{\text{ansatz}}(t) = \begin{cases} 0 & \text{for } t \leq 0 \\ \frac{d}{2} \left(\frac{t}{\tau/2} \right)^2 + \delta x & \text{for } 0 < t < \tau/2 \\ d - \frac{d}{2} \left(\frac{\tau-t}{\tau/2} \right)^2 - \delta x & \text{for } \tau/2 < t < \tau \\ d & \text{for } t \geq \tau, \end{cases} \quad (\text{G2})$$

with

$$\delta x = \frac{\lambda}{4\pi} \arcsin \left[\left(\frac{\tau_{\text{CB}}}{\tau} \right)^2 \right] \leq \frac{\lambda}{8}. \quad (\text{G3})$$

The effect of the sudden steps by δx is best understood considering the dynamics from the reference frame comoving with the trap. There, the classical particle is constantly kept at the position of the minimum of the tilted potential, thus avoiding in this reference frame motional excitations (e.g., slosh motion); see Fig. 7(b).

We note that the same solution, $x_{\text{ansatz}}(t)$, was derived in Ref. [65] by minimizing the transport time for a particle confined within a distance δx from the center of a harmonic trap. The ansatz trajectory $x_{\text{ansatz}}(t)$ also resembles that proposed in Ref. [66], which is obtained by minimizing the anharmonic contribution of the trap potential. This condition, in fact, can be shown to be related to minimizing the slosh motion as achieved by $x_{\text{ansatz}}(t)$.

We also remark that a different type of transport control has been proposed, where the Hamiltonian $\hat{H}(t)$ in Eq. (C1) is extended with a linear potential term controllable in time, which could be realized by means of an additional optical lattice with a lattice constant about 10 times that of the conveyor belt lattice [67]. In fact, a time-dependent linear potential allows one in theory to perfectly counteract the noninertial forces experienced by the atom in the reference frame comoving with $x_{\text{trap}}(t)$, thereby enabling unity fidelity for arbitrary transport trajectories $x_{\text{trap}}(t)$. This approach requires, however, much greater energy resources, since the counteracting lattice to be effective must be about 10 times deeper than the conveyor belt lattice.

APPENDIX H: OPTIMAL QUANTUM CONTROL OF TRANSPORT TRAJECTORIES

Optimal quantum control searches for the trajectory $x_{\text{trap}}(t)$ that maximizes the transport fidelity $\mathcal{F}(\tau, T_{\perp})$ as defined in Eq. (C4) for a given transport duration τ and transverse temperature T_{\perp} . Relying on numerical simulations of the transport problem (see Appendix C), we search for an optimal transport trajectory in the form of a Fourier series,

$$x_{\text{trap}}(t) = d \frac{1 - \cos(\nu_1 t)}{2} + \sum_{j=1}^{j_{\text{max}}} b_j \sin(\nu_j t), \quad t \in [0, \tau], \quad (\text{H1})$$

where the frequencies $\nu_j = \pi j / \tau$ are chosen to satisfy the boundary conditions $x_{\text{trap}}(0) = 0$ and $x_{\text{trap}}(\tau) = d$. We choose the maximum frequency $\nu_{j_{\text{max}}}$ to lie within the bandwidth of our control system of around 800 kHz to ensure that x_{trap} can be faithfully reproduced in the transport experiments (see Appendix E). Importantly, the bandwidth constraint $\nu_{j_{\text{max}}}$ does not significantly affect the maximum attainable fidelity when the condition $\nu_{j_{\text{max}}} \gtrsim U_0 / (2\pi\hbar)$ is fulfilled, which is the case here.

Numerical simulations comparing the maximum fidelity reached by the optimization procedure as a function of the bandwidth of the control system show that the limitation to frequencies below $\nu_{j_{\text{max}}}$ has no significant effect in the range of parameters considered in this work. In fact, because $\nu_{j_{\text{max}}}$ is larger than $U_0 / (2\pi\hbar)$, the control system bandwidth allows driving any relevant transition, i.e., any transition between pairs of discrete states of the trap, for which tunneling to neighboring sites is negligible.

Moreover, we conjecture that the optimal transport trajectory satisfies the point symmetry $x_{\text{trap}}(t) = d - x_{\text{trap}}(\tau - t)$, which is equivalent to reducing the search parameter space to the even Fourier coefficients $\{b_{2j}\}$ and thus taking $b_{2j+1} = 0$. This conjecture is supported by numerical studies, showing that when the search parameter space is unconstrained, the weight of the odd coefficients is negligible compared to that of the even coefficients.

For a robust convergence of the search algorithm to a global optimum of $\mathcal{F}(\tau, T_{\perp})$, it is convenient to start the optimization procedure with good initial values of the coefficients $\{b_{2j}\}$ defining the transport trajectory. For this purpose, based on physical intuition, we consider the trajectory defined in Eq. (G2), $x_{\text{ansatz}}(t)$, which is designed to avoid motional excitations of a classical point particle. We project this ansatz into the form of Eq. (H1), thus obtaining the initial set of control parameters $\{b_{2j}\}$ for the numerical optimization procedure. We note here that alternative to $x_{\text{ansatz}}(t)$, one can choose as ansatz for the optimization procedure an optimal solution obtained for a slightly longer transport time [51].

While $x_{\text{ansatz}}(t)$ produces no motional excitations for a classical point particle, it does cause small, but not negligible wave packet deformations because of the anharmonicity of the potential. These excitations, if not counteracted via optimal quantum control, would result in a loss of transport fidelity $\mathcal{F}(\tau)$, which becomes especially significant for τ close to τ_{QB} . Our numerical optimization of the transport process shows that optimal quantum control of x_{trap} achieves this objective by avoiding too large motional excitations (e.g., breathing and slosh motion) in the

reference frame comoving with the conveyor belt during the whole transport process.

We here note that the degree of control can be increased by changing in time the trap depth, in addition to $x_{\text{trap}}(t)$. While for classical particles the shortest transport time is achieved when the trap depth is held constant, and equal to its maximum allowed value U_0 , for quantum particles the minimum time can in theory be reduced by controlling the trap depth in time, while keeping it below U_0 . Whether this additional control parameter allows a visible reduction of τ_{QB} will be investigated in future work.

Concerning the search algorithm, we use the interior-point method provided by MATLAB with the `fmincon` function, which allows us to include constraints. We use constraints to limit the gradient of the trajectory to the maximum slew rate of the control system (0.84 rad/ μs), which is determined by how fast the OPLL is able to track the change of its set point; see Appendix B.

We note that for transport over many lattice sites, more frequency components ν_j fit within the system bandwidth due to the longer transport time, resulting in a higher-dimensional search parameter space. In this case, using a reduced randomized basis of functions to represent $x_{\text{trap}}(t)$, as done by the DCRA algorithm [68], is expected to be preferable to exhaustively searching through the whole system bandwidth at once, as done here.

APPENDIX I: BANG-BANG CONTROL

A widely used transport method is the so-called bang-bang type of transport. We here compare the fidelities achieved with our optimal control optimization procedure to the fidelities of two types of bang-bang transport protocols: the linear transport and the parabolic transport. For the linear transport, $x_{\text{trap}}(t)$ follows a trajectory with constant speed from the initial to the target position. For the parabolic transport, $x_{\text{trap}}(t)$ is constantly accelerated with $\ddot{x}_{\text{trap}}(t) = a$ on the first half of the transport and constantly decelerated with $\ddot{x}_{\text{trap}}(t) = -a$ on the second half.

Both protocols are better understood in the reference frame comoving with the trap. During the linear transport, the wave packet is subject to two momentum kicks: one at the start and one at the end. During the parabolic transport, the wave packet is subject to three position kicks: one at the start by $-a/\omega$, one at half of the transport time by $2a/\omega$, and one at the end by $-a/\omega$. In both cases, motional excitations are created after the initial kick. However, the transport process can be timed so that the excitations created by the first and possibly middle kicks are undone by the last kick. The simulated infidelities of the two transport types are shown in Fig. 8 and compared to the infidelity of the optimal control transport as well as the adiabatic transport discussed in Appendix J. The ‘‘magic’’ transport durations for which the transport brings the wave packet back to a minimally excited state lie close to

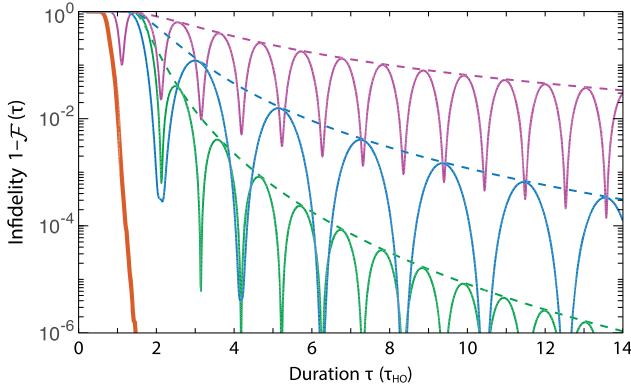


FIG. 8. Transport protocols compared. Infidelity computed numerically for the same conditions of Fig. 2 and $T_{\perp} = 0$ using different transport protocols. From top to bottom: a linear transport ramp (purple), parabolic control (blue), adiabatic control (green), optimal quantum control (thick red). The dashed lines represent the envelope functions according to Eqs. (I1a), (I1b), and (J2).

multiples of approximately the harmonic period. The small, but visible deviation from the harmonic period τ_{HO} can be understood to a very good approximation as the result of the anharmonic potential, which yields an effectively lower trap frequency $\tilde{\omega}_{\text{HO}} \approx \omega_{\text{HO}} - E_{\text{rec}}/\hbar$ and, correspondingly, an effectively longer oscillation period $\tilde{\tau}_{\text{HO}} \approx \tau_{\text{HO}}[1 + E_{\text{rec}}\tau_{\text{HO}}/(2\pi\hbar)]$.

The dashed lines are the envelopes (worst-case infidelities) derived in the harmonic approximation for the two bang-bang protocols:

$$\tau_{\text{linear}}(\mathcal{F}) = \tau_{\text{HO}} \frac{1}{\pi} \frac{\ell_{\text{QGT}}}{[-\log(\mathcal{F})]^{1/2}}, \quad (\text{I1a})$$

$$\tau_{\text{parabolic}}(\mathcal{F}) = \tau_{\text{HO}} \frac{2}{\pi} \frac{\sqrt{\ell_{\text{QGT}}}}{[-\log(\mathcal{F})]^{1/4}}. \quad (\text{I1b})$$

Their scaling with distance, $\ell_{\text{QGT}} \propto d$, indicates that the linear transport protocol is faster for short transport distances, whereas the parabolic transport is faster for long distances, since the trap can be accelerated to higher speeds. Both are, however, much slower than the transport operation obtained by optimal control, which is also shown for comparison in Fig. 8.

APPENDIX J: ADIABATIC LIMIT

Adiabatic transport minimizes excitations of the wave packet during the entire transport by using smooth transport ramps. As an example, we here consider ramps that follow a sinusoidal trajectory, which is continuous in position, velocity, and acceleration,

$$x_{\text{trap}}(t) = A \sin(2\pi t/\tau) + dt/\tau, \quad (\text{J1})$$

where $A = -d/(2\pi)$ is chosen such that $\dot{x}_{\text{trap}}(0) = 0$. For a given fidelity, we find in the harmonic approximation that the required worst-case duration of the adiabatic transport is

$$\tau_{\text{adiabatic}}(\mathcal{F}) = \tau_{\text{HO}} \sqrt{\frac{2}{3} + \left[\frac{\ell_{\text{QGT}}^2}{\pi^2 [-\log(\mathcal{F})]} \right]^{1/3}}. \quad (\text{J2})$$

This relation is shown as the dashed green curve in Fig. 8.

APPENDIX K: ESTIMATION OF GEOMETRIC PATH LENGTH AND ENERGY SPREAD

A very good, analytic approximation of the geometric path length can be obtained assuming that at the quantum speed limit the wave packet is steadily accelerated in the first half and steadily decelerated in the second half, meaning that the average position of the wave packet evolves as

$$\bar{x}_{\text{QB}}(t) \approx \begin{cases} 2d(t/\tau)^2 & \text{for } 0 < t < \tau/2 \\ -d + 4dt/\tau - 2d(t/\tau)^2 & \text{for } \tau/2 < t < \tau. \end{cases} \quad (\text{K1})$$

Numerical simulations confirm that this assumption, where $\bar{x}_{\text{QB}}(t)$ is a smooth function of time, is well fulfilled despite the much less regular shape of the optimal control transport trajectories $x_{\text{trap}}(t)$. Moreover, we assume that quantum optimal control preserves the wave packet $|\psi(t)\rangle$ close to a coherent state $|\alpha(t)\rangle$, avoiding too large spreading and deformation, in particular when it approaches the points of steepest potential, where the trap loses its ability to confine. The coherent state is specified by its phase space coordinates,

$$\alpha(t) = \frac{\bar{x}_{\text{QB}}(t)}{2\Delta x} + i \frac{m\dot{\bar{x}}_{\text{QB}}(t)}{2\Delta p}, \quad (\text{K2})$$

with the position and momentum width being $\Delta x \approx \sqrt{\hbar/(2m\omega)}$ and $\Delta p \approx \hbar/(2\Delta x)$. Thus, the geometric path length ℓ_{QB} , as defined in Eq. (4) of the main text, is obtained by integrating the Fubini-Study differential form,

$$ds_{\text{FS}} = |\dot{\alpha}(t)| dt, \quad (\text{K3})$$

over the duration τ . The integration produces

$$\ell_{\text{QB}} \approx \frac{d}{2\Delta x} f\left(\frac{\tau_{\text{HO}}}{\pi\tau_{\text{QB}}}\right), \quad (\text{K4})$$

which corresponds to Eq. (5) of the main text.

We note that the factor $d/(2\Delta x)$ can be identified with the geodesic length ℓ_{QGT} determined by the quantum geometric tensor [7,69]. In the atom transport problem,

the quantum geometric tensor $\chi_{\mu,\nu}$ reduces to a scalar quantity $\chi_{1,1}$ because of the single control parameter used to transport the atom, i.e., the conveyor belt position x_{trap} . Its value is specified by the differential form $ds_{\text{QGT}}^2 = dx_{\text{trap}}\chi_{1,1}dx_{\text{trap}} = 1 - |\langle \psi_0(x_{\text{trap}} + dx_{\text{trap}}) | \psi_0(x_{\text{trap}}) \rangle|^2$, where $|\psi_0(x_{\text{trap}})\rangle = \exp(-i\hat{p}x_{\text{trap}}/\hbar)|\psi_{\text{init}}\rangle$ denotes the ground state of the conveyor belt displaced to the position x_{trap} (\hat{p} is the momentum operator). The physical meaning of the quantum geometric tensor is that of the Fubini-Study metric in the restricted manifold of states reachable by an adiabatic transformation of the control parameter x_{trap} . An explicit computation of its value yields $\chi_{1,1} = (\Delta p/\hbar)^2$, from which we directly obtain

$$\ell_{\text{QGT}} = \int_0^d ds_{\text{QGT}} = \frac{d\Delta p}{\hbar} \approx \frac{d}{2\Delta x}, \quad (\text{K5})$$

where the last step follows from the approximately Gaussian shape of the ground state. Notably, the geodesic defined by the quantum geometric tensor, in stark contrast with the Fubini-Study geodesic, denotes a path that actual physical processes (e.g., adiabatic transformations) can follow. In contrast to ℓ_{QB} in Eq. (K4), ℓ_{QGT} is a purely geometric quantity independent of the out-of-equilibrium dynamics of the process. Its length ℓ_{QGT} does however scale with the transport distance d , and it can be loosely interpreted as the number of local transformations necessary to carry out the transport process.

For the determination of an upper bound on the energy spread ΔE , we rely on the same assumptions made to estimate ℓ_{QB} , i.e., an approximately coherent state evolving as specified in Eq. (K2). A direct calculation of the instantaneous energy spread yields

$$\begin{aligned} \Delta E(t) &= [\langle \psi(t) | \hat{H}^2(t) | \psi(t) \rangle - \langle \psi(t) | \hat{H}(t) | \psi(t) \rangle^2]^{1/2} \\ &\approx \left[\dot{\bar{x}}_{\text{QB}}^2(t) \Delta p^2 + \left(\frac{\partial U(x,t)}{\partial x} \right)^2 \Delta x^2 \right]^{1/2} [1 + \mathcal{O}(\eta^2)], \end{aligned} \quad (\text{K6})$$

where $U(x,t)$ refers to the lattice potential, as defined in Eqs. (B3) and (B4), the derivative of the potential is computed at $x = \bar{x}_{\text{QB}}(t)$, and $\eta^2 = E_{\text{rec}}/(\hbar\omega) = 1/\sqrt{4U_0/E_{\text{rec}}}$ is the Lamb-Dicke factor, which is negligible for the trap depths considered in this work. The two terms in Eq. (K6) correspond to the leading contributions to the energy uncertainty,

$$\Delta K(t) = \Delta p |\dot{\bar{x}}_{\text{QB}}(t)|, \quad (\text{K7a})$$

$$\Delta U(t) = \Delta x \left| \frac{\partial U(x,t)}{\partial x} \right|_{x=\bar{x}_{\text{QB}}(t)}, \quad (\text{K7b})$$

originating from the kinetic (ΔK) and potential (ΔU) energy. The origin of the two terms can be intuitively

understood if we consider the evolution of the wave packet in the reference frame comoving with $\bar{x}_{\text{QB}}(t)$. There, the wave packet is at rest and displaced from the center of the site by a distance $\bar{x}_{\text{QB}}(t) - x_{\text{trap}}(t)$, where the potential has a nonvanishing slope $\partial U/\partial x$, which explains the potential contribution $\Delta U(t)$. A Galilean transformation from the comoving to the laboratory reference frame introduces a term equal to $\dot{\bar{x}}_{\text{QB}}(t)\hat{p}$ to the Hamiltonian (Heisenberg representation), explaining the kinetic contribution $\Delta K(t)$.

We bound ΔU from above by replacing the derivative of the potential (i.e., the force applied to the wave packet) by its maximum value. For the conveyor belt potentials in Eqs. (B3) and (B4), the maximum of the derivative, $2\pi U_0/\lambda$, is reached at the positions $\pm\lambda/8$ relative to the center of the site, yielding the inequality

$$\Delta E(t) < [\dot{\bar{x}}_{\text{QB}}^2(t) \Delta p^2 + (2\pi U_0/\lambda)^2 \Delta x^2]^{1/2}. \quad (\text{K8})$$

Integrating this expression over time [18] gives an upper bound on the time-averaged energy uncertainty,

$$\Delta E < \Delta E_{\text{upper}} = \frac{\hbar}{\tau_{\text{QB}}} \ell_{\text{QGT}} f\left(\frac{\tau_{\text{QB}}}{2n\tau_{\text{HO}}}\right), \quad (\text{K9})$$

which corresponds to Eq. (8) of the main text.

We note that at the quantum speed limit, for very long transport distances, $n = d/(\lambda/2) \gg 1$, ΔE is dominated by the kinetic rather than the potential contribution,

$$\frac{\Delta K}{\Delta U} > \frac{\Delta p}{\Delta x} \frac{d/\tau}{2\pi U_0/\lambda} = n \frac{\tau_{\text{HO}}}{\tau} \propto \sqrt{n} \gg 1, \quad (\text{K10})$$

where ΔK and ΔU denote here the time average of $\Delta K(t)$ and $\Delta U(t)$, respectively; in this expression, the first inequality results from the foregoing upper bound on $\Delta U(t)$, whereas the proportionality assumption follows from the scaling $\tau \propto \tau_{\text{HO}}\sqrt{n}$ expected for a quantum brachistochrone process. Hence, we find that in the limit of $n \gg 1$, the energy uncertainty ΔE of a transport process at the quantum speed limit reduces to the time average of $\Delta K(t)$ in Eq. (K7a):

$$\Delta E \approx \frac{\hbar}{\tau_{\text{QB}}} \ell_{\text{QGT}}. \quad (\text{K11})$$

APPENDIX L: LIMIT OF LONG DISTANCES

To transport atoms over n lattice sites, the quantum brachistochrone time τ_{QB} is of the order of $\tau_{\text{HO}}\sqrt{n}$, as shown in Eq. (3) of the main text. In turn, such a transport time corresponds to velocities of the order of $n\lambda/\tau_{\text{QB}} = \sqrt{n}\lambda/\tau_{\text{HO}}$. Importantly, the transport velocity increases with \sqrt{n} when atoms are transported in the shortest possible time.

Experimentally, the maximum velocity at which atoms can be transported is determined by the maximum velocity at

which the optical conveyor belt can be displaced. In our setup, this maximum velocity is at around 50 mm/s, limited by the slew rate of the control system (see Appendix B).

Considering the foregoing scaling of the transport velocity with n , the maximum velocity of the conveyor belt presently limits the transport distance to about one lattice site, $n \approx 1$, over which atoms can be transported following a quantum brachistochrone for trap depths up to $300E_{\text{rec}}$, which have been considered in this work. We also note that the present optical-lattice control system [48] allows us to transport atoms over much longer distances with high fidelity, though in a time longer than τ_{QB} .

APPENDIX M: MANDELSTAM-TAMM BOUND IN THE LIMIT OF LONG DISTANCES

We investigate the scaling of the Mandelstam-Tamm bound of Eq. (1) in the main text in the limit of long transport distances. In its most general form [19], when the initial $|\psi_{\text{init}}\rangle$ and target $|\psi_{\text{target}}\rangle$ states are not necessarily orthogonal, the Mandelstam-Tamm time reads

$$\tau_{\text{QB}} \geq \tau_{\text{MT}} = \frac{\ell_{\text{geo}}}{\Delta E/\hbar}, \quad (\text{M1})$$

where ΔE represents the time-averaged energy uncertainty [18] and ℓ_{geo} denotes the geodesic length as measured by the Fubini-Study metric [55], $\ell_{\text{geo}} = \arccos(|\langle \psi_{\text{target}} | \psi_{\text{init}} \rangle|)$.

Concerning the numerator in Eq. (M1), it is evident that ℓ_{geo} levels off to its maximum value, $\pi/2$, since for long distances, $d \gg \Delta x$, the target state is effectively orthogonal to the initial state.

Concerning the denominator in Eq. (M1), it can be shown, see Eq. (K11), that for very long transport distances its expression is well approximated by

$$\Delta E/\hbar \approx \frac{d}{2\Delta x} \frac{1}{\tau_{\text{QB}}} \propto \sqrt{d}, \quad (\text{M2})$$

where the last step follows from the scaling $\tau_{\text{QB}} \propto \sqrt{d}$ expected for the quantum brachistochrone time τ_{QB} as a function of the transport distance d ; see Eq. (3) of the main text. The scaling of ΔE in Eq. (M2) results in the seemingly counterintuitive fact that τ_{MT} is a monotonically decreasing function of the distance, in stark contrast with the monotonically increasing behavior of τ_{QB} with respect to the distance. Note that with a different argument, the wrong scaling of the Mandelstam-Tamm bound was recognized before, studying the limit of very short transport durations in harmonic traps [46].

[1] L. Mandelstam and I. Tamm, *The Uncertainty Relation between Energy and Time in Non-Relativistic Quantum Mechanics*, *J. Phys. (Moscow)* **9**, 249 (1945).

- [2] J. Anandan and Y. Aharonov, *Geometry of Quantum Evolution*, *Phys. Rev. Lett.* **65**, 1697 (1990).
- [3] N. Margolus and L. B. Levitin, *The Maximum Speed of Dynamical Evolution*, *Physica (Amsterdam)* **120D**, 188 (1998).
- [4] L. B. Levitin and T. Toffoli, *Fundamental Limit on the Rate of Quantum Dynamics: The Unified Bound is Tight*, *Phys. Rev. Lett.* **103**, 160502 (2009).
- [5] D. P. Pires, M. Cianciaruso, L. C. Céleri, G. Adesso, and D. O. Soares-Pinto, *Generalized Geometric Quantum Speed Limits*, *Phys. Rev. X* **6**, 021031 (2016).
- [6] K. Funo, J.-N. Zhang, C. Chatou, K. Kim, M. Ueda, and A. del Campo, *Universal Work Fluctuations During Shortcuts to Adiabaticity by Counterdiabatic Driving*, *Phys. Rev. Lett.* **118**, 100602 (2017).
- [7] M. Bukov, D. Sels, and A. Polkovnikov, *Geometric Speed Limit of Accessible Many-Body State Preparation*, *Phys. Rev. X* **9**, 011034 (2019).
- [8] J. D. Bekenstein, *Energy Cost of Information Transfer*, *Phys. Rev. Lett.* **46**, 623 (1981).
- [9] L. B. Levitin, *Physical Limitations of Rate, Depth, and Minimum Energy in Information Processing*, *Int. J. Theor. Phys.* **21**, 299 (1982).
- [10] S. Lloyd, *Ultimate Physical Limits to Computation*, *Nature (London)* **406**, 1047 (2000).
- [11] D. Kielpinski, C. Monroe, and D. J. Wineland, *Architecture for a Large-Scale Ion-Trap Quantum Computer*, *Nature (London)* **417**, 709 (2002).
- [12] J. P. Home, D. Hanneke, J. D. Jost, J. M. Amini, D. Leibfried, and D. J. Wineland, *Complete Methods Set for Scalable Ion Trap Quantum Information Processing*, *Science* **325**, 1227 (2009).
- [13] M. Karski, L. Förster, J.-M. Choi, A. Steffen, W. Alt, D. Meschede, and A. Widera, *Quantum Walk in Position Space with Single Optically Trapped Atoms*, *Science* **325**, 174 (2009).
- [14] W. C. Campbell, J. Mizrahi, Q. Quraishi, C. Senko, D. Hayes, D. Hucul, D. N. Matsukevich, P. Maunz, and C. Monroe, *Ultrafast Gates for Single Atomic Qubits*, *Phys. Rev. Lett.* **105**, 090502 (2010).
- [15] S. van Frank, A. Negretti, T. Berrada, R. Bücker, S. Montangero, J. Schaff, T. Schumm, T. Calarco, and J. Schmiedmayer, *Interferometry with Non-Classical Motional States of a Bose-Einstein Condensate*, *Nat. Commun.* **5**, 4009 (2014).
- [16] V. M. Schäfer, C. J. Ballance, K. Thirumalai, L. J. Stephenson, T. G. Ballance, A. M. Steane, and D. M. Lucas, *Fast Quantum Logic Gates with Trapped-Ion Qubits*, *Nature (London)* **555**, 75 (2018).
- [17] L. Haws and T. Kiser, *Exploring the Brachistochrone Problem*, *Am. Math. Mon.* **102**, 328 (1995).
- [18] For a time-dependent Hamiltonian $\hat{H}(t)$, the energy spread is defined through an average $\Delta E := \tau^{-1} \int_0^\tau dt [\langle \psi(t) | \hat{H}(t)^2 | \psi(t) \rangle - \langle \psi(t) | \hat{H}(t) | \psi(t) \rangle^2]^{1/2}$ over the process duration τ [2].
- [19] S. Deffner and S. Campbell, *Quantum Speed Limits: From Heisenberg's Uncertainty Principle to Optimal Quantum Control*, *J. Phys. A* **50**, 453001 (2017).
- [20] G. N. Fleming, *A Unitarity Bound on the Evolution of Nonstationary States*, *Nuovo Cimento Soc. Ital. Fis.* **16A**, 232 (1973).

- [21] K. Bhattacharyya, *Quantum Decay and the Mandelstam-Tamm-Energy Inequality*, *J. Phys. A* **16**, 2993 (1983).
- [22] L. Vaidman, *Minimum Time for the Evolution to an Orthogonal Quantum State*, *Am. J. Phys.* **60**, 182 (1992).
- [23] C. M. Bender, D. C. Brody, H. F. Jones, and B. K. Meister, *Faster than Hermitian Quantum Mechanics*, *Phys. Rev. Lett.* **98**, 040403 (2007).
- [24] A. del Campo, I. L. Egusquiza, M. B. Plenio, and S. F. Huelga, *Quantum Speed Limits in Open System Dynamics*, *Phys. Rev. Lett.* **110**, 050403 (2013).
- [25] M. M. Taddei, B. M. Escher, L. Davidovich, and R. L. de Matos Filho, *Quantum Speed Limit for Physical Processes*, *Phys. Rev. Lett.* **110**, 050402 (2013).
- [26] S. Deffner and E. Lutz, *Quantum Speed Limit for Non-Markovian Dynamics*, *Phys. Rev. Lett.* **111**, 010402 (2013).
- [27] B. Shanahan, A. Chenu, N. Margolus, and A. del Campo, *Quantum Speed Limits across the Quantum-to-Classical Transition*, *Phys. Rev. Lett.* **120**, 070401 (2018).
- [28] M. Okuyama and M. Ohzeki, *Quantum Speed Limit Is Not Quantum*, *Phys. Rev. Lett.* **120**, 070402 (2018).
- [29] H. A. Rabitz, M. M. Hsieh, and C. M. Rosenthal, *Quantum Optimally Controlled Transition Landscapes*, *Science* **303**, 1998 (2004).
- [30] A. Carlini, A. Hosoya, T. Koike, and Y. Okudaira, *Time-Optimal Quantum Evolution*, *Phys. Rev. Lett.* **96**, 060503 (2006).
- [31] T. Caneva, M. Murphy, T. Calarco, R. Fazio, S. Montangero, V. Giovannetti, and G. E. Santoro, *Optimal Control at the Quantum Speed Limit*, *Phys. Rev. Lett.* **103**, 240501 (2009).
- [32] S. Lloyd and S. Montangero, *Information Theoretical Analysis of Quantum Optimal Control*, *Phys. Rev. Lett.* **113**, 010502 (2014).
- [33] R. Heck, O. Vuculescu, J. J. Sørensen, J. Zoller, M. G. Andreasen, M. G. Bason, P. Ejlertsen, O. Elíasson, P. Haikka, J. S. Laustsen, L. L. Nielsen, A. Mao, R. Müller, M. Napolitano, M. K. Pedersen, A. R. Thorsen, C. Bergenholtz, T. Calarco, S. Montangero, and J. F. Sherson, *Remote Optimization of an Ultracold Atoms Experiment by Experts and Citizen Scientists*, *Proc. Natl. Acad. Sci. U.S.A.* **115**, E11231 (2018).
- [34] M. G. Bason, M. Viteau, N. Malossi, P. Huillery, E. Arimondo, D. Ciampini, R. Fazio, V. Giovannetti, R. Mannella, and O. Morsch, *High-Fidelity Quantum Driving*, *Nat. Phys.* **8**, 147 (2012).
- [35] S. van Frank, M. Bonneau, J. Schmiedmayer, S. Hild, C. Gross, M. Cheneau, I. Bloch, T. Pichler, A. Negretti, T. Calarco, and S. Montangero, *Optimal Control of Complex Atomic Quantum Systems*, *Sci. Rep.* **6**, 34187 (2016).
- [36] A. Vepsäläinen, S. Danilin, and G. S. Paroanu, *Superadiabatic Population Transfer in a Three-Level Superconducting Circuit*, *Sci. Adv.* **5**, eaau5999 (2019).
- [37] D. C. Brody and D. W. Hook, *On Optimum Hamiltonians for State Transformations*, *J. Phys. A* **39**, L167 (2006).
- [38] G. C. Hegerfeldt, *Driving at the Quantum Speed Limit: Optimal Control of a Two-Level System*, *Phys. Rev. Lett.* **111**, 260501 (2013).
- [39] By direct coupling we refer to, “teleportation” Hamiltonians containing terms of the kind $|x+d\rangle\langle x|$, which displace the state by a finite amount d .
- [40] A. Couvert, T. Kawalec, G. Reinaudi, and D. Guéry-Odelin, *Optimal Transport of Ultracold Atoms in the Non-Adiabatic Regime*, *Europhys. Lett.* **83**, 13001 (2008).
- [41] R. Bowler, J. Gaebler, Y. Lin, T. R. Tan, D. Hanneke, J. D. Jost, J. P. Home, D. Leibfried, and D. J. Wineland, *Coherent Diabatic Ion Transport and Separation in a Multizone Trap Array*, *Phys. Rev. Lett.* **109**, 080502 (2012).
- [42] A. Walther, F. Ziesel, T. Ruster, S. T. Dawkins, K. Ott, M. Hettrich, K. Singer, F. Schmidt-Kaler, and U. Poschinger, *Controlling Fast Transport of Cold Trapped Ions*, *Phys. Rev. Lett.* **109**, 080501 (2012).
- [43] J. Alonso, F. M. Leupold, Z. U. Solèr, M. Fadel, M. Marinelli, B. C. Keitch, V. Negnevitsky, and J. P. Home, *Generation of Large Coherent States by Bang-Bang Control of a Trapped-Ion Oscillator*, *Nat. Commun.* **7**, 11243 (2016).
- [44] G. Ness, C. Shkedrov, Y. Florshaim, and Y. Sagi, *Realistic Shortcuts to Adiabaticity in Optical Transfer*, *New. J. Phys.* **20**, 095002 (2018).
- [45] M. Murphy, L. Jiang, N. Khaneja, and T. Calarco, *High-Fidelity Fast Quantum Transport with Imperfect Controls*, *Phys. Rev. A* **79**, 020301(R) (2009).
- [46] E. Torrontegui, S. Ibáñez, X. Chen, A. Ruschhaupt, D. Guéry-Odelin, and J. G. Muga, *Fast Atomic Transport without Vibrational Heating*, *Phys. Rev. A* **83**, 013415 (2011).
- [47] Y. Miroshnychenko, W. Alt, I. Dotsenko, L. Förster, M. Khudaverdyan, D. Meschede, D. Schrader, and A. Rauschenbeutel, *Quantum Engineering: An Atom-Sorting Machine*, *Nature (London)* **442**, 151 (2006).
- [48] C. Robens, S. Brakhane, W. Alt, D. Meschede, J. Zopes, and A. Alberti, *Fast, High-Precision Optical Polarization Synthesizer for Ultracold-Atom Experiments*, *Phys. Rev. Applied* **9**, 034016 (2018).
- [49] D. Guéry-Odelin, A. Ruschhaupt, A. Kiely, E. Torrontegui, S. Martínez-Garaot, and J. G. Muga, *Shortcuts to Adiabaticity: Concepts, Methods, and Applications*, *Rev. Mod. Phys.* **91**, 045001 (2019).
- [50] C. P. Koch, *Controlling Open Quantum Systems: Tools, Achievements, and Limitations*, *J. Phys. Condens. Matter* **28**, 213001 (2016).
- [51] Q.-M. Chen, R.-B. Wu, T.-M. Zhang, and H. Rabitz, *Near-Time-Optimal Control for Quantum Systems*, *Phys. Rev. A* **92**, 063415 (2015).
- [52] D. Sels, *Stochastic Gradient Ascent Outperforms Gamers in the Quantum Moves Game*, *Phys. Rev. A* **97**, 040302(R) (2018).
- [53] A. Alberti, C. Robens, W. Alt, S. Brakhane, M. Karski, R. Reimann, A. Widera, and D. Meschede, *Super-resolution Microscopy of Single Atoms in Optical Lattices*, *New. J. Phys.* **18**, 053010 (2016).
- [54] A. Steffen, A. Alberti, W. Alt, N. Belmechri, S. Hild, M. Karski, A. Widera, and D. Meschede, *Digital Atom Interferometer with Single Particle Control on a Discretized Space-Time Geometry*, *Proc. Natl. Acad. Sci. U.S.A.* **109**, 9770 (2012).
- [55] The Fubini-Study metric is the only Riemannian metric on the projective Hilbert space that, up to a constant factor, is invariant under all unitary transformations, thus including any possible coherent time evolution.

- [56] W.K. Wootters, *Statistical Distance and Hilbert Space*, *Phys. Rev. D* **23**, 357 (1981).
- [57] In the related problem of transporting a quasiparticle (e. g., transferring an atomic excitation via an optical resonator), nonlocal Rabi coupling between initial and final states is possible, once the fast degrees of freedom (e. g., propagation of light) are adiabatically eliminated. For the transport of a massive particle, such an effectively nonlocal coupling fundamentally does not exist.
- [58] T. Caneva, T. Calarco, R. Fazio, G.E. Santoro, and S. Montangero, *Speeding Up Critical System Dynamics through Optimized Evolution*, *Phys. Rev. A* **84**, 012312 (2011).
- [59] X. Zhang, R. P. del Aguila, T. Mazzoni, N. Poli, and G. M. Tino, *Trapped-Atom Interferometer with Ultracold Sr Atoms*, *Phys. Rev. A* **94**, 043608 (2016).
- [60] V. Xu, M. Jaffe, C. D. Panda, S. L. Kristensen, L. W. Clark, and H. Müller, *Probing Gravity by Holding Atoms for 20 Seconds*, *Science* **366**, 745 (2019).
- [61] C. Robens, W. Alt, D. Meschede, C. Emary, and A. Alberti, *Ideal Negative Measurements in Quantum Walks Disprove Theories Based on Classical Trajectories*, *Phys. Rev. X* **5**, 011003 (2015).
- [62] H.-J. Briegel, T. Calarco, D. Jaksch, J. I. Cirac, and P. Zoller, *Quantum Computing with Neutral Atoms*, *J. Mod. Opt.* **47**, 415 (2000).
- [63] N. Belmechri, L. Förster, W. Alt, A. Widera, D. Meschede, and A. Alberti, *Microwave Control of Atomic Motional States in a Spin-Dependent Optical Lattice*, *J. Phys. B* **46**, 104006 (2013).
- [64] S. MacNamara and G. Strang, *Operator Splitting*, in *Splitting Methods in Communication, Imaging, Science, and Engineering* (Springer International Publishing, Cham, Switzerland, 2016), pp. 95–114.
- [65] X. Chen, E. Torrontegui, D. Stefanatos, J. S. Li, and J. G. Muga, *Optimal Trajectories for Efficient Atomic Transport without Final Excitation*, *Phys. Rev. A* **84**, 043415 (2011).
- [66] Q. Zhang, J. G. Muga, D. Guéry-Odelin, and X. Chen, *Optimal Shortcuts for Atomic Transport in Anharmonic Traps*, *J. Phys. B* **49**, 125503 (2016).
- [67] A. Rodriguez-Prieto, S. Martínez-Garaot, I. Lizuain, and J. G. Muga, *Interferometer for Force Measurement via a Shortcut to Adiabatic Arm Guiding*, *Phys. Rev. Research* **2**, 023328 (2020).
- [68] N. Rach, M. M. Müller, T. Calarco, and S. Montangero, *Dressing the Chopped-Random-Basis Optimization: A Bandwidth-Limited Access to the Trap-Free L* , *Phys. Rev. A* **92**, 062343 (2015).
- [69] M. Kolodrubetz, D. Sels, P. Mehta, and A. Polkovnikov, *Geometry and Non-Adiabatic Response in Quantum and Classical Systems*, *Phys. Rep.* **697**, 1 (2017).

5.3 Summary

In this chapter, the existence of a quantum speed limit of atom transport beyond local coupling in optical lattices has been verified. Single atoms prepared in the motional ground state of the optical lattice potential were transported by a distance of one lattice site ($\approx 0.5 \mu\text{m}$) in durations as short as the minimum fundamental limit, known as quantum speed limit. Using optimal quantum control, the transport operations are optimized to bring the atoms back to their motional ground state at the end of the transport, even though they may populate highly excited states during the process. We observed that for transport durations shorter than the quantum speed limit, the ground state population inevitably drops below unity. Moreover, using matter wave interferometry we have verified that the transport operations preserve coherence for all transport durations above the quantum speed limit.

The minimum transport duration revealed by the measurements is much higher than the one predicted by the Mandelstam-Tamm inequality. In the past, it was well understood that this was due to the complexity of the system that cannot be approximated by a two-level system. There was, however, no theoretical estimate of the minimum transport duration consistent with our measurements. We here presented an estimate that explains our observations, based on a geometric approach that only considers the states that can be physically reached by the system.

Summary and Outlook

In this thesis I have reported some results on the study of matter wave dynamics of single atoms in optical lattices. Particularly, in chapter 3 I have presented my results on time-resolved single-pixel imaging of the atomic wave packets in a static optical lattice. Even though the recorded images are restricted to a single pixel, they allow the observation of the single, double and triple peak structure of the first three eigenstates of the trapping potential. Moreover, the time-resolved single-pixel images contain not only information about the wave function but also the trapping potential. In fact, the Hamiltonian moments, the energy spectrum of the Hamiltonian and the population probabilities in the basis of motional eigenstates are extracted from the single-pixel images. Moreover, the phase of the single-pixel images of atomic wave packets in the lattice potential reveals different topological properties as compared to wave packets in a harmonic potential. The phase acquired by the single-pixel image of a wave packet in a harmonic potential is topologically protected against phase winding, while for wave packets in the lattice potential the topological protection is broken. This observation opened room for new questions on possible topological properties that have been left for a future work. The questions include a possible definition of a winding number for wave packets in anharmonic potentials and the possibility of observing topological phase transitions with the imaging method presented in this thesis. Another extension to the work presented in chapter 3 is the generalization to multi-pixel imaging that could be obtained by spatially displacing the reference wave function to different locations, mimicking a multi-pixel detector.

In chapter 4, the single-pixel images of the atomic wave packets obtained with the method presented in chapter 3 have been used to verify the Mandelstam-Tamm (MT) and Margolus-Levitin (ML) bounds for atomic wave packets in a static lattice potential. The bounds set a limit to the maximum rate of change of the wave packet, known as quantum speed limit. The MT and ML bounds are characterized by the energy spread and the mean energy of the wave function respectively. The two bounds may predict different values, therefore, two regions in the time domain are defined: one where the MT bound is more restrictive and one where the ML bound is more restrictive. The two regions meet at the crossover time $\tau_c := \pi\hbar E/(2\Delta E)$ where the two bounds predict the same value. For evolution times shorter than τ_c the MT bound is more restrictive while for longer times the ML bound is more restrictive. The measurements here presented cover both regions and a transition from the MT region to the ML region is observed. Experimental demonstrations of the MT and ML bounds have been done in the past for effective two-level systems [40, 84, 85], however, to my knowledge this is the first demonstration of the MT and ML bounds in a multi-level system. Additionally, the difference between the maximum rate of change imposed by the MT bound and the measured rate of change of the atomic wave packets, quantified by the Fubini-Study metric, has been obtained for 34 different initial states. It has been found that, as the energy spread increases, the difference converges to a small value even though the wave packet populates many energy

levels thus deviating from a simple two-level system.

In chapter 5, the quantum speed limit was verified for a quantum process more involved than the one discussed in chapter 4, namely the transport of atomic wave packets without final vibrational excitations over distances much longer than the width of the wave packet. The existence of a minimum duration of a transport operation with limited resources has been verified. The atoms were transported with trajectories obtained by optimal quantum control which minimizes the final motional excitations. It was observed that the atoms, initially prepared in the motional ground state, are still in the ground state after the transport when the transport duration is above the quantum speed limit. For durations below the speed limit, however, a finite probability of populating higher motional levels is unavoidable. The minimum transport duration observed is well beyond the one predicted by the MT bound, but we have provided a theoretical estimate, based on geometric arguments, consistent with the measurements. Moreover, using atom interferometry we have verified that the transport operations preserve coherence.

In future measurements, the fast coherent atom transport operations over one lattice site could be directly applied on quantum walks experiments. The shorter duration of the transport process translates into a higher number of operations within the coherence time of the system. This is important when a minimum number of steps is required, as in the measurement of topological invariants with the split-step quantum-walk protocol [88]. An immediate extension of the work here presented is the transport over longer distances. This would increase the enclosed space-time area of an atom interferometer, therefore boosting its sensitivity [89, 90]. Computing optimal trajectories for longer transport distances requires a higher computational power since the size of the search space increases (for example a higher number of Fourier components). Moreover, the atoms transported over longer distances reach higher speeds. This brings more challenges from the technical side since the position control of the lattice has a maximum speed, limited by the slew rate of the optical phase-locked loop. This could be overcome substituting the feedback control by feedforward control [91].

In chapter 4 we have seen that atomic wave packets in a static optical lattice evolve at a rate very close to the limit imposed by the Mandelstam-Tamm bound. On the other hand, in chapter 5 we have seen that the quantum speed limit of excitation-less atom transport is orders of magnitude slower than the limit imposed by the Mandelstam-Tamm bound, but is consistent with the estimate obtained from geometric arguments. Future investigations along this line could bring up important insight about what determines the minimum duration of a quantum process. A deeper understanding of this topic can have important implications in quantum technologies, since it can help in identifying systems that can be potentially faster, an important criterion in a field that is in constant need of speeding up quantum processes.

Bibliography

- [1] M. R. Lam, N. Peter, T. Groh, W. Alt, C. Robens, D. Meschede, A. Negretti, S. Montangero, T. Calarco and A. Alberti, “Demonstration of Quantum Brachistochrones between Distant States of an Atom”, *Phys. Rev. X* 11 (1 2021) 011035 (cit. on p. v).
- [2] G. Ness, M. R. Lam, W. Alt, D. Meschede, Y. Sagi and A. Alberti, *Observing quantum-speed-limit crossover with matter wave interferometry*, 2021, arXiv: 2104.05638 [quant-ph] (cit. on p. v).
- [3] L. K. Grover, “Quantum Mechanics Helps in Searching for a Needle in a Haystack”, *Phys. Rev. Lett.* 79 (2 1997) 325 (cit. on p. 1).
- [4] L. K. Grover, “Quantum Computers Can Search Rapidly by Using Almost Any Transformation”, *Phys. Rev. Lett.* 80 (19 1998) 4329 (cit. on p. 1).
- [5] R. J. Hughes, D. M. Alde, P. Dyer, G. G. Luther, G. L. Morgan and M. Schauer, “Quantum cryptography”, *Contemporary Physics* 36.3 (1995) 149, eprint: <https://doi.org/10.1080/00107519508222149> (cit. on p. 1).
- [6] C. L. Degen, F. Reinhard and P. Cappellaro, “Quantum sensing”, *Rev. Mod. Phys.* 89 (3 2017) 035002 (cit. on p. 1).
- [7] J. Berezovsky, M. H. Mikkelsen, N. G. Stoltz, L. A. Coldren and D. D. Awschalom, “Picosecond Coherent Optical Manipulation of a Single Electron Spin in a Quantum Dot”, *Science* 320.5874 (2008) 349, ISSN: 0036-8075, eprint: <https://science.sciencemag.org/content/320/5874/349.full.pdf> (cit. on p. 1).
- [8] K.-M. C. Fu, S. M. Clark, C. Santori, C. R. Stanley, M. C. Holland and Y. Yamamoto, “Ultrafast control of donor-bound electron spins with single detuned optical pulses”, *Nature Physics* 4.10 (2008) 780, ISSN: 1745-2481 (cit. on p. 1).
- [9] A. Steane, “The ion trap quantum information processor”, *Applied Physics B* 64.6 (1997) 623, ISSN: 1432-0649 (cit. on p. 1).
- [10] J. P. Home, D. Hanneke, J. D. Jost, J. M. Amini, D. Leibfried and D. J. Wineland, “Complete Methods Set for Scalable Ion Trap Quantum Information Processing”, *Science* 325.5945 (2009) 1227, ISSN: 0036-8075, eprint: <https://science.sciencemag.org/content/325/5945/1227.full.pdf> (cit. on p. 1).
- [11] F. Del Santo and B. Dakić, “Two-Way Communication with a Single Quantum Particle”, *Phys. Rev. Lett.* 120 (6 2018) 060503 (cit. on p. 1).
- [12] M. Murphy, S. Montangero, V. Giovannetti and T. Calarco, “Communication at the quantum speed limit along a spin chain”, *Phys. Rev. A* 82 (2 2010) 022318 (cit. on p. 1).

- [13] S. G. Schirmer and P. J. Pemberton-Ross, “Fast high-fidelity information transmission through spin-chain quantum wires”, *Phys. Rev. A* **80** (3 2009) 030301 (cit. on p. 1).
- [14] V. Giovannetti, S. Lloyd and L. Maccone, “Quantum Measurement Bounds beyond the Uncertainty Relations”, *Phys. Rev. Lett.* **108** (26 2012) 260405 (cit. on p. 1).
- [15] S. Campbell, M. G. Genoni and S. Deffner, “Precision thermometry and the quantum speed limit”, *Quantum Science and Technology* **3.2** (2018) 025002 (cit. on p. 1).
- [16] V. Giovannetti, S. Lloyd and L. Maccone, “Advances in quantum metrology”, *Nature Photonics* **5.4** (2011) 222, ISSN: 1749-4893 (cit. on p. 1).
- [17] F. Campaioli, F. A. Pollock, F. C. Binder, L. Céleri, J. Goold, S. Vinjanampathy and K. Modi, “Enhancing the Charging Power of Quantum Batteries”, *Phys. Rev. Lett.* **118** (15 2017) 150601 (cit. on p. 1).
- [18] W. S. Warren, H. Rabitz and M. Dahleh, “Coherent Control of Quantum Dynamics: The Dream Is Alive”, *Science* **259.5101** (1993) 1581, ISSN: 0036-8075, eprint: <https://science.sciencemag.org/content/259/5101/1581.full.pdf> (cit. on p. 1).
- [19] H. Rabitz, R. de Vivie-Riedle, M. Motzkus and K. Kompa, “Whither the Future of Controlling Quantum Phenomena?”, *Science* **288.5467** (2000) 824, ISSN: 0036-8075, eprint: <https://science.sciencemag.org/content/288/5467/824.full.pdf> (cit. on p. 1).
- [20] A. Steane, C. F. Roos, D. Stevens, A. Mundt, D. Leibfried, F. Schmidt-Kaler and R. Blatt, “Speed of ion-trap quantum-information processors”, *Phys. Rev. A* **62** (4 2000) 042305 (cit. on p. 1).
- [21] J. Eisert, M. van den Worm, S. R. Manmana and M. Kastner, “Breakdown of Quasilocality in Long-Range Quantum Lattice Models”, *Phys. Rev. Lett.* **111** (26 2013) 260401 (cit. on p. 1).
- [22] M. Foss-Feig, Z.-X. Gong, C. W. Clark and A. V. Gorshkov, “Nearly Linear Light Cones in Long-Range Interacting Quantum Systems”, *Phys. Rev. Lett.* **114** (15 2015) 157201 (cit. on p. 1).
- [23] S. Deffner, “Quantum speed limits and the maximal rate of information production”, *Phys. Rev. Research* **2** (1 2020) 013161 (cit. on p. 1).
- [24] S. Deffner and E. Lutz, “Generalized Clausius Inequality for Nonequilibrium Quantum Processes”, *Phys. Rev. Lett.* **105** (17 2010) 170402 (cit. on p. 1).
- [25] V. Giovannetti, S. Lloyd and L. Maccone, “Quantum limits to dynamical evolution”, *Phys. Rev. A* **67** (5 2003) 052109 (cit. on p. 1).
- [26] P. Pfeifer, “How fast can a quantum state change with time?”, *Phys. Rev. Lett.* **70** (22 1993) 3365 (cit. on p. 1).

-
- [27] L. Mandelstam and I. G. Tamm, “The Uncertainty Relation Between Energy and Time in Non-relativistic Quantum Mechanics”, *J. Phys. USSR* 9 (1945) 249 (cit. on pp. 1, 37).
- [28] N. Margolus and L. B. Levitin, “The maximum speed of dynamical evolution”, *Physica. D* 120 (1998) 188 (cit. on pp. 1, 37).
- [29] M. Bukov, D. Sels and A. Polkovnikov, “Geometric Speed Limit of Accessible Many-Body State Preparation”, *Phys. Rev. X* 9 (1 2019) 011034 (cit. on pp. 1, 2, 52).
- [30] J. Anandan and Y. Aharonov, “Geometry of quantum evolution”, *Phys. Rev. Lett.* 65 (14 1990) 1697 (cit. on pp. 1, 39).
- [31] S. Deffner and E. Lutz, “Quantum Speed Limit for Non-Markovian Dynamics”, *Phys. Rev. Lett.* 111 (1 2013) 010402 (cit. on p. 1).
- [32] M. M. Taddei, B. M. Escher, L. Davidovich and R. L. de Matos Filho, “Quantum Speed Limit for Physical Processes”, *Phys. Rev. Lett.* 110 (5 2013) 050402 (cit. on p. 1).
- [33] A. del Campo, I. L. Egusquiza, M. B. Plenio and S. F. Huelga, “Quantum Speed Limits in Open System Dynamics”, *Phys. Rev. Lett.* 110 (5 2013) 050403 (cit. on p. 1).
- [34] S. P. Jordan, “Fast quantum computation at arbitrarily low energy”, *Phys. Rev. A* 95 (3 2017) 032305 (cit. on p. 1).
- [35] J. D. Bekenstein, “Energy Cost of Information Transfer”, *Phys. Rev. Lett.* 46 (10 1981) 623 (cit. on p. 1).
- [36] H. J. Bremermann, “Minimum energy requirements of information transfer and computing”, *International Journal of Theoretical Physics* 21.3 (1982) 203, ISSN: 1572-9575 (cit. on p. 1).
- [37] S. Lloyd, “Ultimate physical limits to computation”, *Nature* 406.6799 (2000) 1047, ISSN: 1476-4687 (cit. on p. 1).
- [38] W. Heisenberg, “Über den anschaulichen Inhalt der quantentheoretischen Kinematik und Mechanik”, *Zeitschrift für Physik* 43.3 (1927) 172, ISSN: 0044-3328 (cit. on pp. 1, 23, 37).
- [39] L. B. Levitin and T. Toffoli, “Fundamental Limit on the Rate of Quantum Dynamics: The Unified Bound Is Tight”, *Phys. Rev. Lett.* 103 (16 2009) 160502 (cit. on pp. 1, 39).
- [40] M. G. Bason, M. Viteau, N. Malossi, P. Huillery, E. Arimondo, D. Ciampini, R. Fazio, V. Giovannetti, R. Mannella and O. Morsch, “High-fidelity quantum driving”, *Nature Physics* 8.2 (2012) 147, ISSN: 1745-2481 (cit. on pp. 2, 38, 73).
- [41] S. Subhankar, Y. Wang, T.-C. Tsui, S. L. Rolston and J. V. Porto, “Nanoscale Atomic Density Microscopy”, *Phys. Rev. X* 9 (2 2019) 021002 (cit. on pp. 2, 23).
- [42] M. McDonald, J. Trisnadi, K.-X. Yao and C. Chin, “Superresolution Microscopy of Cold Atoms in an Optical Lattice”, *Phys. Rev. X* 9 (2 2019) 021001 (cit. on pp. 2, 23).

- [43] A. Mugarza, J. E. Ortega, F. J. Himpfel and F. J. Garcia de Abajo, “Measurement of electron wave functions and confining potentials via photoemission”, *Phys. Rev. B* 67 (8 2003) 081404 (cit. on pp. 2, 23).
- [44] R. Chrapkiewicz, M. Jachura, K. Banaszek and W. Wasilewski, “Hologram of a single photon”, *Nature Photonics* 10.9 (2016) 576, ISSN: 1749-4893 (cit. on pp. 2, 23).
- [45] J. S. Lundeen, B. Sutherland, A. Patel, C. Stewart and C. Bamber, “Direct measurement of the quantum wavefunction”, *Nature* 474.7350 (2011) 188, ISSN: 1476-4687 (cit. on pp. 2, 23).
- [46] D. Steck, “Cesium D line data”, (2010) (cit. on pp. 3, 6, 8).
- [47] A. M. Steane, M. Chowdhury and C. J. Foot, “Radiation force in the magneto-optical trap”, *J. Opt. Soc. Am. B* 9.12 (1992) 2142 (cit. on p. 3).
- [48] P. Zeeman, “On the influence of magnetism on the nature of the light emitted by a substance”, *American Journal of Physics* 16 (1897) 218 (cit. on p. 3).
- [49] R. Grimm, M. Weidemüller and Y. B. Ovchinnikov, “Optical Dipole Traps for Neutral Atoms”, *Advances in Atomic, Molecular and Optical Physics* 42.C (2000) 95 (cit. on pp. 3, 5).
- [50] M. Karski, “State-selective transport of single neutral atoms”, PhD thesis: Universität Bonn, 2010 (cit. on pp. 3, 8).
- [51] C. G. Townsend, N. H. Edwards, C. J. Cooper, K. P. Zetie, C. J. Foot, A. M. Steane, P. Szriftgiser, H. Perrin and J. Dalibard, “Phase-space density in the magneto-optical trap”, *Phys. Rev. A* 52 (2 1995) 1423 (cit. on p. 3).
- [52] J. Dalibard and C. Cohen-Tannoudji, “Laser cooling below the Doppler limit by polarization gradients: simple theoretical models”, *J. Opt. Soc. Am. B* 6.11 (1989) 2023 (cit. on p. 4).
- [53] C. Robens, S. Brakhane, W. Alt, D. Meschede, J. Zopes and A. Alberti, “Fast, High-Precision Optical Polarization Synthesizer for Ultracold-Atom Experiments”, *Phys. Rev. Applied* 9 (3 2018) 034016 (cit. on pp. 4, 10, 11).
- [54] D. Döring, “Ein Experiment zum zustandsabhängigen Transport einzelner Atome”, Master thesis, Universität Bonn, 2007 (cit. on p. 5).
- [55] A. Kastler, “Optical Methods of Atomic Orientation and of Magnetic Resonance*”, *J. Opt. Soc. Am.* 47.6 (1957) 460 (cit. on p. 8).
- [56] J. D. Miller, R. A. Cline and D. J. Heinzen, “Far-off-resonance optical trapping of atoms”, *Phys. Rev. A* 47 (6 1993) R4567 (cit. on p. 8).
- [57] R. A. Cline, J. D. Miller, M. R. Matthews and D. J. Heinzen, “Spin relaxation of optically trapped atoms by light scattering”, *Opt. Lett.* 19.3 (1994) 207 (cit. on p. 8).
- [58] C. Robens, “Testing the Quantumness of Atom Trajectories”, PhD thesis: Universität Bonn, 2017 (cit. on pp. 8, 10, 14).
- [59] L. Förster, “Microwave control of atomic motion in a spin dependent optical lattice”, PhD thesis: Universität Bonn, 2010 (cit. on p. 8).
- [60] S. Kuhr, W. Alt, D. Schrader, I. Dotsenko, Y. Miroshnychenko, A. Rauschenbeutel and D. Meschede, “Analysis of dephasing mechanisms in a standing-wave dipole trap”, *Phys. Rev. A* 72 (2 2005) 023406 (cit. on pp. 8, 12).

-
- [61] K. Bergmann, H. Theuer and B. W. Shore, “Coherent population transfer among quantum states of atoms and molecules”, *Rev. Mod. Phys.* **70** (3 1998) 1003 (cit. on p. 8).
- [62] I. Dotsenko, “Raman spectroscopy of single atoms”, Diplomarbeit, Universität Bonn, 2002 (cit. on p. 9).
- [63] T. Groh, “Fast transport of single atoms in optical lattices using quantum optimal control”, Master thesis, Universität Bonn, 2018 (cit. on pp. 12, 17, 25).
- [64] L. Förster, M. Karski, J.-M. Choi, A. Steffen, W. Alt, D. Meschede, A. Widera, E. Montano, J. H. Lee, W. Rakreungdet and P. S. Jessen, “Microwave Control of Atomic Motion in Optical Lattices”, *Phys. Rev. Lett.* **103** (23 2009) 233001 (cit. on p. 12).
- [65] N. Belmechri, L. Förster, W. Alt, A. Widera, D. Meschede and A. Alberti, “Microwave control of atomic motional states in a spin-dependent optical lattice”, *Journal of Physics B: Atomic, Molecular and Optical Physics* **46**.10 (2013) (cit. on pp. 13, 14, 17).
- [66] D. J. Wineland, C. Monroe, W. M. Itano, D. Leibfried, B. E. King and D. M. Meekhof, “Experimental Issues in Coherent Quantum-State Manipulation of Trapped Atomic Ions”, *Journal of research of the National Institute of Standards and Technology* **103**.3 (1998) 259, j33win[PII], issn: 1044-677X (cit. on p. 13).
- [67] D. Leibfried, R. Blatt, C. Monroe and D. Wineland, “Quantum dynamics of single trapped ions”, *Rev. Mod. Phys.* **75** (1 2003) 281 (cit. on p. 14).
- [68] S. Blatt, J. W. Thomsen, G. K. Campbell, A. D. Ludlow, M. D. Swallows, M. J. Martin, M. M. Boyd and J. Ye, “Rabi spectroscopy and excitation inhomogeneity in a one-dimensional optical lattice clock”, *Phys. Rev. A* **80** (5 2009) 052703 (cit. on p. 14).
- [69] S. MacNamara and G. Strang, “Operator Splitting”, *Splitting Methods in Communication, Imaging, Science, and Engineering*, Springer International Publishing, 2016 95 (cit. on pp. 17, 25).
- [70] N. Peter, “Optimal quantum control of atomic wave packets in optical lattices”, PhD thesis: Universität Bonn, 2018 (cit. on pp. 17, 25).
- [71] E. L. Hahn, “Spin Echoes”, *Phys. Rev.* **80** (4 1950) 580 (cit. on p. 18).
- [72] W. R. Inc., *Mathematica, Version 11.3*, Champaign, IL, 2018 (cit. on p. 20).
- [73] C. M. Günther, B. Pfau, R. Mitzner, B. Siemer, S. Roling, H. Zacharias, O. Kutz, I. Rudolph, D. Schondelmaier, R. Treusch and S. Eisebitt, “Sequential femtosecond X-ray imaging”, *Nature Photonics* **5**.2 (2011) 99, issn: 1749-4893 (cit. on p. 23).
- [74] C. Nicole, H. L. Offerhaus, M. J. J. Vrakking, F. Lépine and C. Bordas, “Photoionization Microscopy”, *Phys. Rev. Lett.* **88** (13 2002) 133001 (cit. on p. 23).
- [75] A. S. Stodolna, A. Rouzée, F. Lépine, S. Cohen, F. Robicheaux, A. Gijsbertsen, J. H. Jungmann, C. Bordas and M. J. J. Vrakking, “Hydrogen Atoms under Magnification: Direct Observation of the Nodal Structure of Stark States”, *Phys. Rev. Lett.* **110** (21 2013) 213001 (cit. on p. 23).
- [76] S. Kunze, G. Rempe and M. Wilkens, “Atomic-Position Measurement via Internal-State Encoding”, *Europhysics Letters (EPL)* **27**.2 (1994) 115 (cit. on p. 23).

- [77] Y. Huismans, A. Rouzée, A. Gijsbertsen, J. H. Jungmann, A. S. Smolkowska, P. S. W. M. Logman, F. Lépine, C. Cauchy, S. Zamith, T. Marchenko, J. M. Bakker, G. Berden, B. Redlich, A. F. G. van der Meer, H. G. Muller, W. Vermin, K. J. Schafer, M. Spanner, M. Y. Ivanov, O. Smirnova, D. Bauer, S. V. Popruzhenko and M. J. J. Vrakking, “Time-Resolved Holography with Photoelectrons”, *Science* 331.6013 (2011) 61, issn: 0036-8075 (cit. on p. 23).
- [78] M. Meckel, A. Staudte, S. Patchkovskii, D. M. Villeneuve, P. B. Corkum, R. Dörner and M. Spanner, “Signatures of the continuum electron phase in molecular strong-field photoelectron holography”, *Nature Physics* 10.8 (2014) 594, issn: 1745-2481 (cit. on p. 23).
- [79] J. Goodman, *Introduction to Fourier Optics*, McGraw-Hill Series in Electrical and Computer Engineering, 1996, isbn: 9780974707723 (cit. on p. 24).
- [80] C. Monroe, D. M. Meekhof, B. E. King and D. J. Wineland, “A “Schrödinger Cat” Superposition State of an Atom”, *Science* 272.5265 (1996) 1131, issn: 0036-8075, eprint: <https://science.sciencemag.org/content/272/5265/1131.full.pdf> (cit. on p. 24).
- [81] H. P. Robertson, “The Uncertainty Principle”, *Phys. Rev.* 34 (1 1929) 163 (cit. on p. 37).
- [82] J. Hilgevoord, “The uncertainty principle for energy and time”, *American Journal of Physics* 64.12 (1996) 1451, eprint: <https://doi.org/10.1119/1.18410> (cit. on p. 37).
- [83] J. Hilgevoord, “The uncertainty principle for energy and time. II”, *American Journal of Physics* 66.5 (1998) 396, eprint: <https://doi.org/10.1119/1.18880> (cit. on p. 37).
- [84] A. Vepsäläinen, S. Danilin and G. S. Paraoanu, “Superadiabatic population transfer in a three-level superconducting circuit”, *Science Advances* 5.2 (2019), eprint: <https://advances.sciencemag.org/content/5/2/eaau5999.full.pdf> (cit. on pp. 38, 73).
- [85] S. van Frank, M. Bonneau, J. Schmiedmayer, S. Hild, C. Gross, M. Cheneau, I. Bloch, T. Pichler, A. Negretti, T. Calarco and S. Montangero, “Optimal control of complex atomic quantum systems”, *Scientific Reports* 6.1 (2016) 34187, issn: 2045-2322 (cit. on pp. 38, 73).
- [86] G. Fubini, “Sulle metriche definite da una forme Hermitiana”, *Atti del Reale Istituto Veneto di Scienze, Lettere ed Arti* 63 (1904) 502 (cit. on pp. 38, 52).
- [87] E. Study, “Kürzeste Wege im komplexen Gebiet”, *Mathematische Annalen* 60.3 (1905) 321, issn: 1432-1807 (cit. on pp. 38, 52).
- [88] T. Rakovszky, J. K. Asbóth and A. Alberti, “Detecting topological invariants in chiral symmetric insulators via losses”, *Phys. Rev. B* 95 (20 2017) 201407 (cit. on p. 74).

-
- [89] H. Müller, S.-w. Chiow, S. Herrmann and S. Chu,
“Atom Interferometers with Scalable Enclosed Area”, *Phys. Rev. Lett.* 102 (24 2009) 240403
(cit. on p. 74).
- [90] S.-w. Chiow, T. Kovachy, H.-C. Chien and M. A. Kasevich,
“ $102\hbar k$ Large Area Atom Interferometers”, *Phys. Rev. Lett.* 107 (13 2011) 130403 (cit. on p. 74).
- [91] M. Werninghaus,
“Controlling atom transport in a two-dimensional state-dependent optical lattice”,
Master thesis, Universität Bonn, 2017 (cit. on p. 74).
- [92] “The Standard Coherent States: The Basics”, *Coherent States in Quantum Physics*,
John Wiley and Sons, Ltd, 2009, chap. 2 13, ISBN: 9783527628285,
eprint: <https://onlinelibrary.wiley.com/doi/pdf/10.1002/9783527628285.ch2>
(cit. on p. 85).
- [93] R. L. Stratonovich, “On a Method of Calculating Quantum Distribution Functions”, 1957
(cit. on p. 85).
- [94] J. Hubbard, “Calculation of Partition Functions”, *Phys. Rev. Lett.* 3 (2 1959) 77 (cit. on p. 85).

Change of energy reference of Hamiltonian moments

The Hamiltonian moments obtained with the method presented in Sec. 3.4 are given with respect to the energy of the reference wave function. The values plotted in Fig. 3.6 are all given with respect to the energy of the ground state. In this section, the expression to do the change of energy reference is derived.

Let E_i be the eigenenergies of the Hamiltonian, with i being the eigenstate number, and let the ground state's energy define the zero energy reference, i.e. $E_0 = 0$. The Hamiltonian moments computed with respect to the ground state's energy are

$$\langle \mathcal{H}^n \rangle = \sum_{i=0}^{\infty} E_i^n p_i, \quad (\text{A.1})$$

where p_i is the population probability of the i 'th eigenstate. The Hamiltonian moments computed with respect to another energy reference E' are

$$\begin{aligned} \langle \mathcal{H}^n \rangle' &= \sum_{i=0}^{\infty} (E_i - E')^n p_i \\ &= \sum_{i=0}^{\infty} \sum_{k=0}^n \binom{n}{k} E_i^{n-k} (-E')^k p_i, \end{aligned} \quad (\text{A.2})$$

where $\binom{n}{k} = n!/(k!(n-k)!)$ is the binomial coefficient. Exchanging the order of the sum this is

$$\begin{aligned} \langle \mathcal{H}^n \rangle' &= \sum_{k=0}^n \binom{n}{k} (-E')^k \sum_{i=0}^{\infty} E_i^{n-k} p_i, \\ &= \sum_{k=0}^n \binom{n}{k} (-E')^k \langle \mathcal{H}^{n-k} \rangle, \end{aligned} \quad (\text{A.3})$$

where Eq.(A.1) has been used for the second equality. This way, the Hamiltonian moments computed with respect to one energy reference can be obtained from the moments computed with respect to another energy reference.

Overlap between coherent states

In this section I will prove that the overlap between two coherent states evolving under the same harmonic potential is always non-zero. Consider a coherent state $|\phi_\alpha(t)\rangle$ associated to the parameter α , i.e. $a|\phi_\alpha(t)\rangle = \alpha|\phi_\alpha(t)\rangle$ where a is the creation operator. The wave function $|\phi_\alpha(t)\rangle$ in the coordinate representation is [92]

$$\phi_\alpha(t, x) = c(\alpha, t, \omega) e^{\sqrt{2}\alpha(t)x/x_0 - x^2/(2x_0^2)} \quad (\text{B.1})$$

where c is a non-zero complex number that depends on α , the evolution time t and the trapping frequency ω , and $\alpha(t) = \alpha \exp(-i\omega t)$. The overlap between two coherent states at different evolution times t_1 and t_2 is

$$\begin{aligned} \langle \phi_\alpha(t_1) | \phi_\alpha(t_2) \rangle &= \int_{-\infty}^{\infty} dx \bar{\phi}_\alpha(t_1, x) \phi_\alpha(t_2, x) \\ &= \bar{c}(\alpha, t_1, \omega) c(\alpha, t_2, \omega) \int_{-\infty}^{\infty} dx e^{\sqrt{2}\bar{\alpha}(t_1)x/x_0 - x^2/(2x_0^2)} e^{\sqrt{2}\alpha(t_2)x/x_0 - x^2/(2x_0^2)} \\ &= \bar{c}(\alpha, t_1, \omega) c(\alpha, t_2, \omega) \int_{-\infty}^{\infty} dx e^{\sqrt{2}(\bar{\alpha}(t_1) + \alpha(t_2))x/x_0 - x^2/x_0^2}. \end{aligned} \quad (\text{B.2})$$

From the Hubbard–Stratonovich transformation [93, 94], the last integral is non-zero. Therefore, $\langle \phi_\alpha(t_1) | \phi_\alpha(t_2) \rangle \neq 0$.

Bound of the phase of single-pixel images

If a complex number c is contained in a circle with center at $p_k \in \mathbb{R}$ and a radius $1 - p_k$ with $0.5 \leq p_k \leq 1$, then its phase $\varphi = \arg(c)$ is bounded by

$$|\varphi| \leq \arcsin\left(\frac{1 - p_k}{p_k}\right). \quad (\text{C.1})$$

As illustrated in Fig. C.1, the triangle defined by the points O, A and B is a right-angled triangle. Therefore, the angle at the origin is $\varphi_{max} = \arcsin[(1 - p_k)/p_k]$ which is an upper bound on the phase of any complex number inside the circle, thus proving Eq.(C.1). This sets an upper bound on the phase of the single-pixel image of a state with population p_k in a single eigenstate, as discussed in Sec. 3.5.

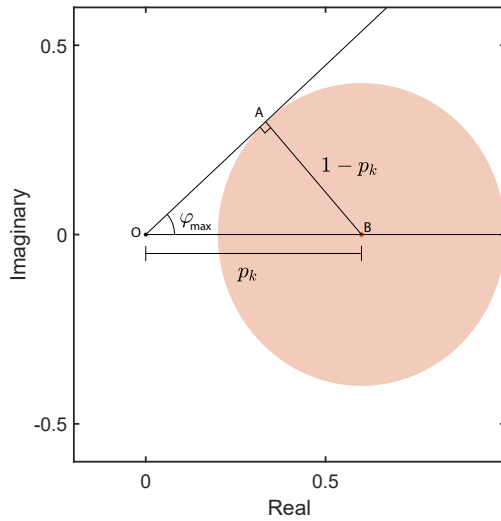


Figure C.1: **Phase bound of single-pixel images.** The phase of a complex number inside the orange circle is bounded by the expression given in Eq.(C.1).

Acknowledgements

First of all I would like to thank Prof. Meschede for giving me the opportunity to join the group. Before coming to Germany I had no experience in experimental physics. I had never used an oscilloscope, and didn't even know what a BNC cable is. On top of that, I was coming from a different field, so my background on atomic physics and quantum optics was very limited. But still, he gave me the chance to join the group as an intern student to acquire the required experimental knowledge before starting the PhD.

I would also like to thank my supervisor Dr. Andrea Alberti for his constant support and guidance, specially since I joined the quantum walks team. His constant quest for improvements helped me, and the other members of the team, achieve very satisfying results. To Dr. Wolfgang Alt who always provided helpful advice, and always had the answer to those questions that seemed unanswerable to all of us. Also Dr. Carsten Robens was of great help in my process of entering a field that was completely new to me. His altruistic help was always present even after he left the group. Moreover, me and the other members of the SDT team inherited an excellent setup from him.

To Dr. Natalie Peter and Thorsten Groh, my first two team mates in the SDT lab, who made of my first half of the PhD a very enjoyable journey. We learned many things together and had fun at the same time. To Andreas Blendl and Jan Uckert who did their master thesis in the SDT team, they were of great help. I finally never really used Andy's "magic box" but we definitely had fun chasing the mysterious magnetic signal all around the institute. Of course to Gal Ness who temporarily joined the SDT team, even though he joined for a short time, he helped a lot in getting the famous Mandelstam-Tamm project going. Also to his professor, Yoav Sagi, for his valuable support on the writing of two of the papers presented in this thesis.

To all the other students of the group (Gautam, Tobi, Richard, Stefan, Sajid...) including the Spanish speaking crew (Eduardo, Miguel, Jose) with whom at some point we almost outnumbered the German speaking members. I want to thank all of them for the stimulating discussions and for sharing the suffering of maintaining ungrateful labs that sometimes gave us satisfaction and sometimes nightmares. I will always remember the barbecues in Tobi's house, the multiple bike rides with Gautam (including the multiple hours waiting for him at the top or every hill) and all the hours wasted in the gym with Jose.

I thank the people that took the time to read parts of my thesis to give me constructive comments that helped me improve the thesis: Carsten, Natalie, Gautam, Eduardo and Nicolas.

I am grateful to Dietmar Haubrich, Fien Latumahina, Annelise von Rudloff-Miglo and Kerstin Steinseifer for all their help concerning the administrative matters, very important to keep the group working.

Por supuesto, voy a estar eternamente agradecido con mi familia, sobre todo mi papá y mi mamá que me han apoyado desde que tengo memoria (dentro de mi limitada memoria, que todo se me olvida). Siempre han confiado en mí, y me han ayudado a realizar mi carrera aunque eso significara estar lejos de casa. A mi esposa Fabiana que ha estado a mi lado desde el día que la conocí, y ahora no imagino mi vida sin ella. A sido fuente de motivación y apoyo constante, incluso los años que pasamos a un océano de distancia. Y a mi hija María Inés, que en sus primeros meses de vida ya nos ha enseñado tanto a

Fabiana y a mí.

Y nunca dejaré de estar agradecido con Dios y la Virgen María, mis eternos protectores y guías.